

NASA CR-189849

NASA-CR-189849
19920008782

COLLEGE
OF
ENGINEERING

Hi-Alpha Forebody Design: Part I
Methodology Base and Initial Parametrics

by

William H. Mason and R. Ravi

VPI-Aero-176 (rev.,)

LIBRARY

LIBRARY COPY
JUL 1 1992
LANGLEY RESEARCH CENTER
LIBRARY
HAMPTON



VIRGINIA
POLYTECHNIC
INSTITUTE
AND
STATE
UNIVERSITY

BLACKSBURG,
VIRGINIA

3 1176 01355 6528

**Hi-Alpha Forebody Design: Part I
Methodology Base and Initial Parametrics**

by

William H. Mason and R. Ravi

VPI-Aero-176 (rev.,)

October 1990
(rev., January 1992)

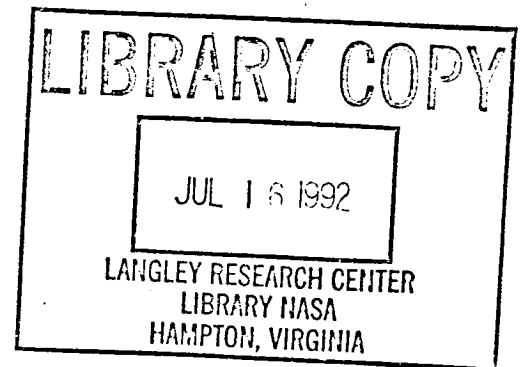
Prepared for:

National Aeronautics and Space Administration
Langley Research Center

Grant No: NAG-1-1037

Covering the period July 17, 1989 - July 15, 1990

Department of Aerospace And Ocean Engineering
Virginia Polytechnic Institute and State University
Blacksburg, VA 24061



N92-18024#

TABLE OF CONTENTS

SUMMARY	1
INTRODUCTION	2
LIST OF SYMBOLS	5
COMPUTATIONAL BASIS	7
LAMONT TANGENT OGIVE	8
Tangent Ogive Forebody Grid	9
Results and Discussion of Lamont Tangent Ogive Computations	9
F-5A FOREBODY	11
F-5A Forebody Geometry Math Model	11
F-5A Grid	12
Results and Discussion of Computations on the F-5A Forebody	13
ERICKSON CHINE FOREBODY	16
Erickson Chine Forebody Math Model	16
Longitudinal lines	17
Cross Sections	18
Erickson Chine Forebody Grid	19
Results and Discussion of the Computations on the Erickson Forebody	20
A MODEL FOR FOREBODY DESIGN:THE GENERIC FOREBODY	23
CONCLUSIONS	25
ACKNOWLEDGEMENTS	26
APPENDIX A MODIFICATIONS TO cfl3d (version 1.1)	27
APPENDIX B F-5A FOREBODY GEOMETRY MATH MODEL	43
APPENDIX C ERICKSON FOREBODY MATH MODEL	59
REFERENCES	71
TABLES	73
FIGURES	74

LIST OF TABLES

1. Tangent ogive Forebody : Comparison of Forces ($M_\infty = 0.20$)

LIST OF FIGURES

1. Typical $C_{n\beta}$ characteristics of an advanced fighter
2. Grafton's classic example (ref 5)
3. Schematic of a typical forebody flowfield characteristics
4. Goal of forebody design effort
5. Samples of shapes employed in fighter forebody design
6. Tangent ogive crude grid comparison with data on windward plane
- 7(a). Tangent ogive crude grid comparison with data ($x/d = 0.5$)
- 7(b). Tangent ogive crude grid comparison with data ($x/d = 2.0$)
- 7(c). Tangent ogive crude grid comparison with data ($x/d = 3.5$)
- 7(d). Tangent ogive crude grid comparison with data ($x/d = 6.0$)
- 8(a). Tangent ogive : Demonstration of α / β results at $x/d = 0.062$
- 8(b). Tangent ogive : Demonstration of α / β results at $x/d = 11.02$
- 8(c). Tangent ogive : Demonstration of α / β results at $x/d = 24.0$
- 9(a). F-5A geometry (from Tom Heglund of Northrop)
- 9(b). F-5A geometry: FS 49.70 in.(forward station)
- 9(c). F-5A geometry: FS 130.35 in.(just prior to straight line side beginning)
- 9(d). F-5A geometry: FS 131.13 in.(just aft of straight line side beginning)
- 9(e). F-5A geometry: FS 194.00 in.(end station)
- 10(a) F-5A wind tunnel model (from NASA Langley)
- 10(b) Set-up used to measure F-5A surface coordinates at VPI

- 11(a). Comparison of F-5A geometry: Station 3.375 in. from nose
- 11(b). Comparison of F-5A geometry: Station 6.25 in. from nose
- 11(c). Comparison of F-5A geometry: Station 9.1875 in. from nose
- 11(d). Comparison of F-5A geometry: Station 15.3125 in. from nose
- 11(e). Comparison of F-5A geometry: Station 18.0625 in. from nose
- 11(f). Comparison of F-5A geometry: Station 22.5 in. from nose
- 12. F-5A computational model (PLOT3D)
- 13. F-5A cross sectional grid and closeup near surface at $x = 9.061$ in.
- 14. F-5A cross sectional grid and closeup near surface at $x = 15.44$ in.
- 15. F-5A cross sectional grid and closeup near surface at $x = 29.6$ in.
- 16. F-5A longitudinal pattern of grid (PLOT3D)
- 17. F-5A convergence history (inviscid) $\alpha = 40^\circ$ and $\beta = 5^\circ$
- 18(a). F-5A convergence history (turbulent) $\alpha = 40^\circ$ and $\beta = 5^\circ$
- 18(b). F-5A convergence history (turbulent) $\alpha = 20^\circ$ and $\beta = 5^\circ$
- 19. F-5A directional stability: Comparison of calculation with experiment
- 20(a). F-5A inviscid surface pressure distribution at $x = 14.02$ in.
- 20(b). F-5A inviscid surface pressure distribution at $x = 29.61$ in.
- 21(a). F-5A turbulent surface pressure distribution at $x = 14.02$ in.
- 21(b). F-5A turbulent surface pressure distribution at $x = 29.61$ in.
- 22. F-5A inviscid vs turbulent surface pressure distribution.
- 23(a). F-5A inviscid surface oil flow pattern $\alpha = 40^\circ$ and $\beta = 5^\circ$
- 23(b). F-5A turbulent surface oil flow pattern $\alpha = 40^\circ$ and $\beta = 5^\circ$
- 24. F-5A inviscid pressure contours at $x = 14.025$ in. ($\alpha = 40^\circ$ and $\beta = 5^\circ$)
- 25. F-5A turbulent pressure contours at $x = 14.025$ in. ($\alpha = 40^\circ$ and $\beta = 5^\circ$)
- 26. F-5A inviscid stagnation pressure at $x = 14.025$ in. ($\alpha = 40^\circ$ and $\beta = 5^\circ$)
- 27. F-5A turbulent stagnation pressure at $x = 14.025$ in. ($\alpha = 40^\circ$ and $\beta = 5^\circ$)
- 28. Details of the Erickson forebody wind tunnel model.

29. Comparison of digitized ordinates and smooth math model for the Erickson forebody for the full range of stations.
30. Comparison of digitized ordinates and smooth math model for the Erickson forebody.
31. Erickson forebody computational model (PLOT3D)
32. Erickson forebody cross sectional grid at $x = 30.00$ in.
33. Erickson forebody convergence history (inviscid) $\alpha = 30^\circ$ and $\beta = 10^\circ$
34. Erickson forebody convergence history (turbulent) $\alpha = 30^\circ$ and $\beta = 10^\circ$
- 35(a). Erickson forebody inviscid surface pressure distribution at $x = 7.19$ in.
- 35(b). Erickson forebody inviscid surface pressure distribution at $x = 13.56$ in.
- 35(c). Erickson forebody inviscid surface pressure distribution at $x = 19.94$ in.
- 36(a). Erickson forebody inviscid surface pressure distribution at $x = 7.19$ in.
- 36(b). Erickson forebody inviscid surface pressure distribution at $x = 13.56$ in.
- 36(c). Erickson forebody inviscid surface pressure distribution at $x = 19.94$ in.
- 37(a). Erickson forebody inviscid vs turbulent surface pressures at $x = 7.19$ in.
- 37(b). Erickson forebody inviscid vs turbulent surface pressures at $x = 13.56$ in.
- 37(c). Erickson forebody inviscid vs turbulent surface pressures at $x = 19.94$ in.
- 38(a). Erickson forebody inviscid vs turbulent surface pressures at $x = 7.19$ in.
- 38(b). Erickson forebody inviscid vs turbulent surface pressures at $x = 13.56$ in.
- 38(c). Erickson forebody inviscid vs turbulent surface pressures at $x = 19.94$ in.
39. Erickson forebody with isolated wing VLM model
40. Wing induced flowfield at Erickson forebody pressure stations.
- 41(a). Erickson forebody inviscid surface pressures at $x = 7.19$ in. ($\alpha = 32.2^\circ$ and $\beta = 0^\circ$)
- 41(b). Erickson forebody inviscid surface pressures at $x = 13.56$ in. ($\alpha = 32.2^\circ$ and $\beta = 0^\circ$)
- 41(c). Erickson forebody inviscid surface pressures at $x = 19.94$ in. ($\alpha = 32.2^\circ$ and $\beta = 0^\circ$)
42. Erickson forebody inviscid surface oil flow pattern ($\alpha = 30^\circ$ and $\beta = 0^\circ$)

43. Erickson forebody turbulent surface oil flow pattern ($\alpha = 30^\circ$ and $\beta = 0^\circ$)
44. Erickson forebody inviscid pressure contours at $x = 13.56$ in. ($\alpha = 30^\circ$ and $\beta = 0^\circ$)
45. Erickson forebody turbulent pressure contours at $x = 13.56$ in. ($\alpha = 30^\circ$ and $\beta = 0^\circ$)
46. Erickson forebody inviscid stagnation pressure at $x = 13.56$ in. ($\alpha = 30^\circ$ and $\beta = 0^\circ$)
47. Erickson forebody turbulent stagnation pressure at $x = 13.56$ in. ($\alpha = 30^\circ$ and $\beta = 0^\circ$)
48. Erickson forebody inviscid surface oil flow pattern ($\alpha = 30^\circ$ and $\beta = 10^\circ$)
49. Erickson forebody turbulent surface oil flow pattern ($\alpha = 30^\circ$ and $\beta = 10^\circ$)
50. Erickson forebody inviscid pressure contours at $x = 13.56$ in. ($\alpha = 30^\circ$ and $\beta = 10^\circ$)
51. Erickson forebody turbulent pressure contours at $x = 13.56$ in. ($\alpha = 30^\circ$ and $\beta = 10^\circ$)
52. Erickson forebody inviscid stagnation pressure at $x = 13.56$ in. ($\alpha = 30^\circ$ and $\beta = 10^\circ$)
53. Erickson forebody turbulent stagnation pressure at $x = 13.56$ in. ($\alpha = 30^\circ$ and $\beta = 10^\circ$)
54. Parametric forebody shapes as driven by the value of n
55. Parametric forebody shapes when the straight sidewall is selected
56. Examples of the parametric forebody for the entire cross section
 - a) elliptic cross sections
 - b) straight wall sides at max half breadth
 - c) chine type cross sections

HI-ALPHA FOREBODY DESIGN: PART I METHODOLOGY BASE AND INITIAL PARAMETRICS

William H. Mason
R. Ravi

Virginia Polytechnic Institute and State University

SUMMARY

The use of Computational Fluid Dynamics (CFD) has been investigated for the analysis and design of aircraft forebodies at high angle of attack combined with sideslip. The results of the investigation show that CFD has reached a level of development where computational methods can be used for high angle of attack aerodynamic design. The classic wind tunnel experiment for the F-5A forebody directional stability has been reproduced computationally over an angle of attack range from 10° to 45° , and good agreement with experimental data was obtained. Computations have also been made at combined angle of attack and sideslip over a chine forebody, demonstrating the qualitative features of the flow, although not producing good agreement with measured experimental pressure distributions. The computations were performed using the code known as `cf13d` for both the Euler equations and the Reynolds equations using a form of the Baldwin-Lomax turbulence model. To study the relation between forebody shape and directional stability characteristics a generic parametric forebody model has been defined which provides a simple analytic math model with flexibility to capture the key shape characteristics of the entire range of forebodies of interest, including chines.

INTRODUCTION

High angle of attack aerodynamic characteristics are key to agility of advanced fighter aircraft. Considerable attention has been devoted to flow asymmetries, advanced control device concepts (forebody "flaps"), and modern control system design (ref. 1-4). However, the requirement for advanced control devices and control systems is in large part due to directional stability characteristics. If the basic directional stability characteristics are aerodynamically tailored by proper shaping of the design, demands on control systems and control devices can be dramatically decreased, and complicated forebody mechanisms (which are undesirable from an aircraft designer's point of view) may not be required.

The aerodynamic design problem can be described using typical aerodynamic characteristics of fighter aircraft. Figure 1 illustrates the problem in terms of typical $C_{n\beta}$ characteristics of an advanced fighter. At low angle of attack the vertical tail provides directional stability. As the angle of attack increases the tail loses effectiveness because it is located in the separated flow region behind the fuselage and wing. For some configurations the directional stability increases again as the angle of attack increases, as shown in the figure. Figure 2 is taken from the report by Grafton, et. al., (ref. 5). In this case the directional stability of the forebody alone is nearly identical to the directional stability of the entire aircraft above $30^\circ \alpha$, and shows the dominant role played by the forebody in causing the directional stability to start increasing for an F-5A type of configuration. Figure 3 (ref. 6) provides a schematic of a typical forebody and flowfield responsible for favorable characteristics, although in this case the concept is quantitatively in error. The leeward vortex is actually bigger but farther away from the surface than the windward vortex. The low pressure associated with the vortex located very close to the surface acts to "pull" the body back to a smaller sideslip, and thus provides a stabilizing moment. The possibility of controlling the flow is shown in the figure, where the cross section is not axisymmetric, and has a small radius of curvature or crease at the max half breadth line location. Figure 4 shows the desirable changes to the $C_{n\beta}$

characteristics shown in figure 1. Ideally the loss of stability should be delayed and the rapid variation should be minimized, with a resulting maximum $C_{n\beta}$ being less than the extremely high values sometimes observed. High values of $C_{n\beta}$ are frequently considered to be an indication of poor C_{nr} characteristics.

Previous development work in this area has been carried out experimentally. Figure 5 illustrates a range of forebody shapes that have been considered for use on fighter aircraft. However the capability now exists to use computations to investigate the design of aircraft components at high angle of attack. This has been demonstrated by recent computational results. One practical example is the analysis of the F/A-18 (ref. 11). Detailed examinations have also been made for tangent ogives, including the effects of surface perturbations on flow asymmetry (ref. 12-14). However, none of the previous work has examined the capability of the methods to compute sideforces arising from combined angle of attack and sideslip on non-axisymmetric forebodies.

Although the general problem of obtaining positive directional stability levels for fighter aircraft at high angle of attack is complicated and component interactions are important, the forebody is crucial, as shown in figure 2, and because of its location necessarily less affected by interactions than other components. Therefore, the broad objective of the current effort is directed toward developing an understanding of forebody static directional stability aerodynamics and methods to tailor the isolated forebody characteristics for desirable high angle of attack characteristics. Specifically: i) how can a favorable contribution to directional stability be induced at lower angles of attack and ii) how can extremely large values of $C_{n\beta}$ (which presumably are indicative of poor C_{nr} characteristics) be eliminated?

This report addresses the necessary first steps required to achieve the overall objective: the capability and credibility of using an advanced computational code to conduct initial aerodynamic design of forebodies. To investigate the current capabilities of CFD, a current, widely used code, cfl3d (ref. 15), was used to compute two cases for which experimental data is available: the F-5A

forebody tested by Grafton, et. al. (ref. 5), and the chine forebody tested by Erickson and Brandon (ref. 7). A discussion of the results is preceded by a description of the initial work done to use **cf13d** in a combined α / β flowfield. After the comparison with the experimental results, a parametric model for a generic forebody is presented which is completely defined by simple analytic formulas. This generic forebody model is capable of describing forebody geometries over an extremely large class of shapes, from sharp edge chines to rectangular cross sections.

LIST OF SYMBOLS

a	maximum half breadth of the generic forebody definition
b	maximum centerline distance of the generic forebody definition
b'	wingspan
c	mean aerodynamic chord
C_L	lift-force coefficient, lift/ $q_\infty S_{ref}$
C_m	pitching-moment coefficient, pitching moment/ $q_\infty S_{ref} c$
C_n	yawing-moment coefficient, yawing moment/ $q_\infty S_{ref} b'$
$C_{n\beta}$	directional stability derivative, $\partial C_n / \partial \beta$
C_p	pressure coefficient, $(p-p_\infty)/q_\infty$
C_x	axial-force coefficient, axial force/ $q_\infty S_{ref}$
C_y	side-force coefficient, side force/ $q_\infty S_{ref}$
C_z	normal-force coefficient, normal force/ $q_\infty S_{ref}$
c_y	local side-force, section side force/ $q_\infty S_{ref}$
D	diameter of circular cross section of tangent ogive
FS	fuselage station
m, n	adjustable parametric coefficients
M_∞	free stream Mach number
l	model length
Re_l	Reynolds number based on model length, l
S_{ref}	reference area
u^*	wall friction velocity, $\sqrt{\tau_w} / \rho$
x, y, z	body coordinate system : x positive aft along model axis, y positive to right and z positive up

x_{ref} moment reference center
 y^+ inner law variable, yu^*/v
 α angle of attack, deg
 β angle of sideslip, deg
 θ azimuthal angle, measured clockwise from windward plane at any cross section

COMPUTATIONAL BASIS

The baseline code for this work was the NASA Langley program **cf13d**. At the start of the effort version 1.1 of this code was selected as being appropriate for this investigation. In this code the three dimensional compressible viscous flow around the body is found by solving the conservative form of the dimensionless, thin layer Navier-Stokes equations.

For turbulent flow **cf13d** uses the Reynolds averaged counterparts of the Navier-Stokes equations. An algebraic turbulence model is used, where the turbulent viscosity μ_t is obtained by using the two layer algebraic eddy viscosity of Baldwin and Lomax (ref. 16) as modified by Degani and Schiff to account for the special characteristics of strongly separated flows in references 17 - 19. The Roe type inviscid flux difference splitting scheme option in the code was used to obtain the results presented in this report.

The farfield computational boundaries were chosen sufficiently far away from the body so as not to affect the forces on the body. They were chosen to be consistent with those used by other investigators *e.g.*, F/A-18 (ref. 11) and tangent ogive (ref. 12). The exact distances have been given under each specific case discussed later. Inflow-outflow boundary conditions were used at the farfield inflow, farfield outflow and the farfield outer boundary. For turbulent computations the grid ahead of the nose was treated as a separate block (as described later). When viscous effects are included the no-slip as well as non-penetration conditions are enforced on the body. At the plane of geometric symmetry periodic conditions are used to include sideslip as well as angle of attack in the freestream flow. The temperature boundary condition is treated by defining the body to be adiabatic.

The computations were made on the NASA Langley Cray-2 computer. Some initial startup activity was required before beginning the forebody study. The available version of the code was modified, as described in Appendix A, to handle the boundary conditions for combined α/β flows, and then validated for operation at combined angles of alpha and beta.

The primary, and minor, modification of the code was the incorporation of a new boundary condition. For the work conducted here a full grid was used wrapping all the way around the body, instead of a typical plane of symmetry grid. Therefore, instead of plane of symmetry boundary conditions, the grid interface in the cross flow plane was setup to allow flow across the grid boundary on the leeward side.

The computational grids were generated using stacked 2D grids at each axial location. The 2D grid in the cross plane was generated using a grid generator provided by W. McCrory (ref. 20) that was originally developed to construct the grid for the calculation of the SR-71 flowfield (ref. 21).

Analysis of flowfield calculations was carried out for the more complicated aspects of the grid and flow visualization using the NASA Ames code PLOT3D (ref. 22). This program was used on the Aerospace and Ocean Engineering Department Iris 4D graphics workstation.

LAMONT TANGENT OGIVE

To check the code and grid setup for this work a simple geometry extensively studied by other investigators was selected. The so-called "Lamont tangent ogive" (ref. 23) was used for the work. This is a 3.5 diameter tangent ogive nose with a cylindrical afterbody. The total length of the ogive and cylindrical forebody was 25 diameters. The objective of computing the flow over this relatively simple geometry was to test the minor modifications that were made to `cfl3d`, including the added boundary condition. The ability of the code to handle combined angle of attack and sideslip is a key part of the study and needed to be verified with a geometry which would provide the same results for α at zero β and β at zero α . Inviscid computations were made at $M_\infty = 0.2$ for two different cases, one for $\alpha = 20^\circ$ and no sideslip and the other with $\beta = 20^\circ$ with no angle of attack.

Tangent Ogive Forebody Grid

The three dimensional grid was constructed from two dimensional O-type cross flow grids which are longitudinally stacked, constituting an H-O topology. The boundaries upstream of the nose and radially away from the body were selected to be consistent with similar calculations done by Hartwich and Hall (ref. 12). The forward boundary extends upstream of the nose by $0.502l$ and radial outer boundary extends $1.06l$ from the model centerline. The reference length l is equal to the longitudinal extent of the forebody, which was 25 diameters.

The grid used for the initial inviscid calculations had 24 points in the radial direction and 57 points in the full circumferential direction. Longitudinally, the grid was clustered near the nose with 22 stations on the forebody and 9 stations ahead of the nose. The grid upstream of the nose was also longitudinally stretched to provide resolution near the nose. The entire inviscid grid consisted of 42,408 points. The results obtained using this grid resulted in irregularities in the surface pressures at the ogive-cylinder intersection and downstream to be discussed below. The problem was reduced by increasing the grid resolution. Thus, subsequent calculations were made by increasing the number of grid points in the circumferential direction to 69 points with total number of points in the entire grid increasing to 51,336 points.

Results and Discussion of the Lamont Tangent Ogive Computations

Initial inviscid calculations used the $24 \times 57 \times 31$ grid for the case of $\alpha = 20^\circ$ and $\beta = 0^\circ$. These results are shown in figures 6 and 7. The experimental data shown in these figures are due to Lamont (ref. 23). Here they are taken from the paper by Hall and Hartwich (ref. 12) and include an adjustment in the pressures. The data were obtained at a wind tunnel freestream Reynolds number of 0.2×10^6 based on the diameter of the tangent ogive. Figure 6 shows the surface pressures on the windward plane of symmetry. The difference in the surface pressure between the experimental and the computational data at sections close to the nose is attributed to the poor

resolution of the stacked O-grid type topology at the nose. Figures 7(a) to 7(d) show the surface pressure coefficient at the axial stations of $x/d = 0.5, 2.0, 3.5$ and 6.0 . The first two locations are on the ogive forebody, the third is at the junction between the forebody and the cylindrical afterbody and the fourth is on the cylindrical afterbody. The θ shown on the x axis is the angle measured clockwise from the windward plane at any cross section with $\theta = 0^\circ$ corresponding to the windward plane and $\theta = 180^\circ$ corresponding to the leeward plane. The inviscid computations agree fairly well with the data on the windward side. Agreement is poor near the nose (fig. 7(a)). Presumably this is due to a lack of grid resolution, as seen in figure 6. The agreement is surprisingly good at $x/d = 2.0$ considering the expectation that viscous effects would have significantly altered the pressure distribution at this angle of attack. However, agreement does deteriorate further downstream, where viscous effects do begin to make a significant effect on the surface pressure distribution as shown in figures 7(c) and 7(d). The irregularities in the computed surface pressures near $\theta = 90^\circ$ decreased significantly when the $24 \times 69 \times 31$ grid was used. All the following figures incorporate this finer grid.

Using the refined mesh, computations were also made for the case of $\alpha = 0^\circ$ and $\beta = 20^\circ$ to verify that the surface pressures and forces were equivalent to the $\alpha = 20^\circ$ and $\beta = 0^\circ$ case. The surface pressures at different cross sections are shown in figures 8(a) to 8(c) for both the cases. The ordinates for the case of $\alpha = 0^\circ$ and $\beta = 20^\circ$ have been shifted by 90° for comparison to the surface pressures from the $\alpha = 20^\circ$ and $\beta = 0^\circ$ case. The pressures are identical in both cases. Table [1] gives the forces for these cases. The forces and moments are nearly identical with the orientation of the body in each case. Only small differences occur between components. The replacement of the plane of symmetry boundary condition with the periodic boundary condition also weakened the convergence.

This computation establishes the validity of the new boundary condition and the ability to treat side slip with angle of attack. Having established confidence in the code for sideslip as well as angle of attack calculations, the calculation of aerodynamic interest were initiated.

F-5A FOREBODY

The flowfield around the F-5A forebody was computed to study the use of an advanced code like **cf13d** in predicting the directional stability characteristics of forebodies at high angles of attack. This forebody had been tested by Sue Grafton , et.al. at NASA Langley Research Center and the results are available in ref 5.

F-5A Forebody Geometry Math Model

The computational math model was constructed using classical conic lofting techniques (ref. 24) based on the lofting information provided by Tom Heglund of Northrop. Figures 9(a) to 9(e) show the F-5A forebody geometry with cross section shapes at different locations along the length of the body, together with the data required to construct the numerical model. The configuration was modeled from the nose longitudinally back to $x = 225$ in. The computational model did not include the canopy. At sections close to the nose, as shown by figures 9(b) and 9(c), the upper and lower maximum half breadth points coincide. However, at sections downstream the upper and lower maximum half breadth points are separated by a flat side wall. Because of this, grid points were clustered near the maximum half breadth points forward of the flat side wall to provide adequate definition on the flat wall portion of the forebody and create smoothly varying longitudinal grid lines. The computer code to generate the F-5A surface co-ordinates is given in Appendix B.

To verify that the wind tunnel model geometry agreed with the math model, Sue Grafton of NASA Langley provided the forebody from the wind tunnel model of the F-5A. The model was a 0.17-scale model of the full scale airplane. Figures 10(a) and 10(b) show the wind tunnel model forebody and the setup that was used to make templates of the cross sections. The measured shape of the forebody at different cross sections was then digitized from a tracing of the shape defined by

the template and compared with the computational model. The cross sectional shapes of the computational and the wind tunnel model agree very well considering the method used to obtain the model shape, as shown in figures 11(a) to 11(f). The shaded surface pattern of the F-5A computational model is given in figure 12.

F-5A Grid

The three dimensional grid was constructed from two dimensional O-type cross flow grids which are longitudinally stacked, constituting an H-O topology. The boundaries upstream of the nose and radially away from the body were initially selected to be consistent with the F/A-18 calculations in ref 11. These were later found to be sufficiently far away from the body so as not to affect the forces and moments on the body. The forward boundary extends upstream of the nose by $0.62l$ and radial outer boundary extends $0.98l$ from the model centerline. The downstream boundary, as explained earlier, extended from the nose back to $x = 225 \text{ in}$ (in full scale) which is as shown in figure 9(a) without the canopy. The reference length l is equal to the longitudinal extent of the forebody which was 31.025 in using the wind tunnel model scale.

For inviscid calculations the grid had 45 points in the radial direction and 93 points in the full circumferential direction. This number was increased based on the experience with the tangent ogive and the need to resolve the details of the cross section. Longitudinally, the grid was clustered near the nose with 25 stations on the forebody and 8 stations ahead of the nose. The grid upstream of the nose was also longitudinally stretched to provide resolution near the nose. The entire inviscid grid consisted of 138,105 points.

For viscous calculations the grid had 65 points in the radial direction with longitudinal and circumferential grid points remaining the same as used for the inviscid calculations. The total number of grid points for the viscous grid was 199,485 points. The grid upstream of the nose was treated as a separate block for turbulent flow calculations. Figures 13 to 15 show the grid used for

the viscous calculations at different cross sections downstream from the nose. The reason for the clustering of the grid points near the maximum half breadth point at stations close to the nose was described above. Figure 16 shows the longitudinal stretching of the grids. For the grid that was used, it can be seen that good resolution of the grid at the nose is required to resolve the flow details there. The actual grid used in the computations had more stations near the nose than that shown in figure 16.

The grid was established with sufficient normal clustering near the surface to adequately resolve the laminar sublayer for the turbulent boundary layer flow. This grid produced an average normal cell size of approximately $10^{-4}l$. At the wind tunnel freestream conditions ($M_\infty = 0.2$, $Re_l = 1.25 \times 10^6$, and $\alpha = 20^\circ$) the baseline grid typically resulted in a value of $y^+ \approx 2$ at the first mesh point away from the body.

Results and Discussion of Computations on the F-5A Forebody

Inviscid calculations were performed for $\alpha = 20^\circ, 30^\circ, 40^\circ$ and 50° with side slip angles of $\beta = 0^\circ, 5^\circ$ and 10° . Turbulent calculations were performed for $\alpha = 10^\circ, 20^\circ, 30^\circ, 40^\circ$ and 45° and $\beta = 5^\circ$. All computations were performed on the Cray-2. The inviscid computations took approximately 0.55 hours of CPU time for convergence, and the turbulent computations took approximately 4.5 hours to reduce oscillations in the lift coefficient C_L and the yawing moment coefficient C_n to a negligible level.

Convergence histories for a typical inviscid case is given in figure 17 in terms of residual and lift. The convergence histories for a typical viscous computation are shown in figure 18 which includes the residual, the lift force, side force and the yawing moment coefficients. The inviscid calculations which were started with a CFL number of 2 and ramped over 100 steps to a CFL number of 6 demonstrated strong convergence. Unlike the inviscid case, the turbulent computations show low frequency decaying oscillations in values of C_L and C_n and require about 5000 iterations for a fully converged solution. The turbulent computations were started with

a CFL number of 0.1 and ramped over 100 steps to a CFL number of 0.3. The detailed behavior of the residual and forces change abruptly after 3000 iterations as shown in figures 18(a) and 18(b). This is the result of reducing the CFL number once the solution ceased to converge, thus, making the oscillations decay further to a steady solution.

The F-5A forebody directional stability experimental data from ref 5 are shown along with the computed inviscid and viscous results in figure 19. The computed values of $C_{n\beta}$ were obtained as the finite difference of the yawing moment coefficients C_n . These values being small, it was required that the solution be fully converged to avoid errors in the computed values of $C_{n\beta}$. It can be seen that both inviscid as well as viscous results show the stabilizing effect of the forebody at high angles of attack. At low angle of attack (10° and 20°) the inviscid and viscous calculations agree with each other and the data. At 30° the viscous computations continue to agree with the data, and at the higher angles of attack (40° and 45°) differences begin to appear. This is reasonable considering both the thin layer assumption and the accuracy of the turbulence model for massively separated flows. Nonetheless, the ability of the computations to reproduce the experimentally observed contribution of the F-5A forebody to directional stability is an exciting result. The viscous calculation results establish the effectiveness of an advanced code like `cf3d` in computing the directional stability characteristics for forebodies at high angles of attack. However the inviscid results are in error. The Euler solution results are shown below to contain the spurious non-physical flow separation arising due to lack of grid resolution. The grid resolution effects were not studied in this report but the issue should be considered as a part of future study.

Figures 20 and 21 show the inviscid and turbulent surface pressure distributions at various cross section stations, respectively. The corresponding cross sectional shapes are shown at the bottom of the figure. The results presented here were carried out on the respective standard grids for the case of $\alpha = 40^\circ$ and $\beta = 5^\circ$. The negative peak pressures are due to the vortices on the upper surface of the cross section and are shown more clearly in the surface flow visualization pictures presented in the following paragraph. The asymmetry in the pressure distribution due to the side-slip can also be seen. Figure 22 provides a comparison of the inviscid and turbulent

results. At station 14 the viscous results clearly show the effect of the vortices, with two low pressure regions underneath the windward and leeward primary vortices. Curiously, at the aft station (29.61), the inviscid results contain the low pressure peaks. At this station the true vortices in the turbulent calculations are well away from the surface, and the flow is massively separated, with the associated low pressure gradients along the surface. The three low pressure peaks in the turbulent solution are due to the windward primary vortex, the leeward primary vortex and the leeward secondary vortex. The inviscid results contain low pressure regions that are related to the cross section curvature.

The flowfield results shown in figures 23 to 27 have been generated using computational flow visualization techniques (PLOT3D). Figure 22a shows the inviscid surface flow pattern for $\alpha = 40^\circ$ and $\beta = 5^\circ$. The dye is injected at two axial stations to observe the formation of separation lines, if any. The inviscid separation lines seem to indicate some kind of spurious separation occurring on the surface. The turbulent flow surface oil flow pattern, is shown in figure 23b for the same α and β . Here, primary separation lines starting from near the nose as well as the secondary separation lines starting from further downstream are shown.

Figures 24 and 25 show the cross sectional pressure contours at the axial station $x = 14.025$ in. from the nose for the inviscid and viscous flows respectively, where these results are again for $\alpha = 40^\circ$ and $\beta = 5^\circ$. The magnitudes associated with the contour quantities are displayed with a color bar on the left. The viscous leeward vortex is bigger and farther away from the surface than the windward vortex in figure 25. The lower surface pressure associated with the vortex closer to the surface acts to pull the body back to smaller sideslip, and thus provides a stabilizing moment. The vortex pattern and asymmetry are more clearly seen in the figures 26 and 27 which are shaded based on the stagnation pressure. The leeward vortex in the case of turbulent flow is farther away from the surface than that of the inviscid flow. This difference in the relative positions of the vortices in turbulent and inviscid cases is the reason for the different directional stability shown in figure 19. The turbulent flow also shows the secondary vortices being shed from under the primary vortices further downstream from the nose.

ERICKSON CHINE FOREBODY

The surface pressure distributions from the chine forebody tested by Erickson and Brandon (ref. 7) were used to investigate the capability of CFD to compute the flow over a chined forebody. The experimental configuration is shown in figure 28 (ref. 7). The geometry information used to construct the grid was supplied by Robert Hall of NASA Langley, and the pressure data was supplied by Gary Erickson, also of NASA Langley.

The wing tunnel model had rows of pressure orifices at FS7.19, FS13.56, and FS19.94. All of the data was taken with the wing present. It was assumed that the presence of the wing would not affect the results at the first station, and have minor effects at the second station. The third row of pressures was considered too close to the wing to provide valid comparisons with the forebody calculations, but are presented to provide additional information.

Erickson Chine Forebody Math Model

The Erickson forebody definition was not available in a convenient form for development of the surface definition. A CAD drawing was made available, together with digitized ordinates of the cross-sections contained on the drawing. We were also supplied with digitized coordinates of the drawing generated by Nielsen Engineering and Research, Inc.* As a basis for the shape, Robert Hall supplied a copy of his notes defining the class of theoretical shapes intended to be used to design the forebody. The forebody was required to blend smoothly to an existing NASA Langley model, and this requirement led to deviations from the theoretical concept.

The surface is constructed using standard lofting techniques. First, the key longitudinal lines are defined as a function of the axial station. In this case the lines are the top center line, the bottom

* The CAD drawing of the model forebody was identified as "Roll Stability Model Forebody", 11 July 1984, C.J. Rozo, Change A

center line, and the max half breadth line. A cross section model is then developed which connects these lines smoothly and produces a section which varies smoothly with axial location. For this model the upper and lower cross sections are developed independently of each other. The listing of the FORTRAN code of the math model is given in Appendix C.

Longitudinal Lines

Upper surface centerline: from the nose to FS7.5 the top centerline is defined by a portion of a 19.5° tangent ogive. Aft of this station the shape is defined by combination of three cubic spline segments and two straight line segments. This model was based on careful analysis of the CAD drawing.

Lower surface centerline: from the nose to FS6.0 the bottom centerline was defined by a portion of a 15° tangent ogive. Aft of this station the shape was defined by a combination of two cubic line segments and two straight line sections. Again, the model was developed based on an analysis of the CAD drawing.

Max half breadth line: from the nose to FS8.0 the max half breadth line was defined by a portion of a 27.5° tangent ogive. A cubic spline was used from FS8.0 to FS19.0, followed by a zero slope straight line segment.

In all cases the line segments and spline end point conditions were chosen to provide smoothly varying changes in the slope of the lines, and to minimize jumps in the curvature distribution. Analysis of the CAD drawing suggests that the modifications to the theoretical shape originally outlined by Hall resulted in some abrupt changes in curvature distribution in the actual model lines (recall that a point and slope type match between surfaces will normally result in a discontinuity in curvature at that point). The exact details of the models are easily found in the listing in Appendix C.

Cross Sections

Upper surface cross section: Forward of FS 7.19 the Hall equation was found to fit the supplied digitized ordinates from the drawing well. Aft of the FS7.17 the section was modified to match the existing circular fuselage at FS23. Thus another station was defined at FS23, which was initially circular, and then departed to make the chine using cubic splines. Between these two sections a combination of the two function was used based on the blending function method described by Barger and Adams (ref.25)

Lower surface cross section: When normalized by the max half breadth line and the lower centerline the digitized representation of the cross sections was found to be the same at all cross sections. Thus only one cross sectional shape was required. This cross section was constructed using Hall's equation as the basis, and adding a spline curve defining the difference between Hall's equation and the actual shape. The difference was found by subtracting the analytic shape given by Hall from the measured ordinates. Because the measured coordinates were slightly noisy, a smooth curve was developed by selecting a small number of points from the data, and using a spline interpolation between the points to evaluate intermediate values.

The results of the math model are compared with the ordinates measured from the drawing in figure 29 for the full range of stations. Figure 30 presents details at the three stations where pressure data was obtained. This is the best smooth model of the forebody we were able to construct. The surface shaded PLOT3D view of the model is shown in figure 31, and demonstrates the resulting smooth contour of the math model. Construction of an accurate math model for the Erickson forebody was one of the most time consuming parts of the work described in this report.

Erickson Chine Forebody Grid

Using a procedure similar to the approach used for the F-5A grid, the three dimensional grid around the Erickson forebody was constructed from two dimensional O-type cross flow grids which were longitudinally stacked, constituting an H-O topology. The boundaries upstream of the nose and radially away from the body were again selected to be consistent with the F/A-18 calculations in ref. 11. The downstream boundary was extended from 19.94 *in* to 30.00 *in* with the same cross section. The forward boundary extends upstream of the nose by 0.61*l* and radial outer boundary extends .99*l* from the model centerline. The reference length *l* is equal to the longitudinal extent of the forebody (30.00 *in*).

The inviscid calculation grid had 45 points in the radial direction and 101 points in the full circumferential direction. Longitudinally, the grid was clustered near the nose with 25 stations on the forebody and 8 stations ahead of the nose. The grid upstream of the nose was also longitudinally stretched to provide resolution near the nose. Care was taken to have axial stations at sections where the experimental surface pressures were available. These were at a distance of 7.19, 13.56 and 19.94 inches from the nose along the length of the body. The entire inviscid grid consisted of 149,985 points.

As compared to the inviscid grid, the viscous calculation grid had 65 points in the radial direction with longitudinal and circumferential grid points remaining the same. The total number of grid points for the viscous grid was 216,645 points. As described for the F-5A calculations, the grid upstream of the nose was treated as a separate block for turbulent flow calculations. Figure 32 shows the viscous grid structure at a typical cross section.

The baseline grid was established with sufficient normal clustering near the surface to adequately resolve the laminar sublayer for the turbulent boundary layer flow. This grid produced an average normal cell size of approximately $10^{-4}l$. At the wind tunnel freestream conditions ($M_\infty = 0.2$, $Re_l = 1.02 \times 10^6$, and $\alpha = 20^\circ$) the baseline grid typically resulted in a value of $y^+ \approx 2$ at the first mesh point away from the surface.

Results and Discussion of the Computations on the Erickson Chine Forebody

Inviscid and turbulent calculations were initially performed for $\alpha = 30^\circ$ with side slip angles $\beta = 0^\circ$ and 10° . Inviscid computations took approximately 0.75 hours of CPU time for convergence to five orders of magnitude. The turbulent computations took approximately 4.0 CPU hours to reduce oscillations in lift force coefficient C_L and yawing moment coefficient C_n to a negligible level, by which time the residual went down two orders in magnitude.

The convergence summary for a typical inviscid and viscous case are given in figures 33 and 34 respectively. Convergence histories of the residual and the normal force coefficients are shown. As in the case of F-5A the inviscid calculations were started with a CFL number of 2 and ramped over 100 steps to a CFL number of 6. Unlike the inviscid case, the turbulent computations show low frequency decaying oscillations in values of C_L and require about 4000 iterations for a fully converged solution. The turbulent computations were started with a CFL number of 0.1 and ramped over 100 steps to a CFL number of 0.3. Once the solution ceased to converge after 2000 iterations the CFL number was increased and the oscillations decayed further to a steady solution. This change in CFL number is the reason for the sudden change in the behavior of the plot in figure 34.

Figures 35 and 36 present the computed inviscid surface pressure distributions on the upper surface at the three pressure instrumented cross sections, with the cross sectional shapes shown below each of the plots. The experimental data were obtained from Gary Erickson. The details of the experimental investigation are available in ref 7. The axial stations where the pressures have been plotted were at a distance of 7.19, 13.56 and 19.94 inches from the nose along the length of the body. Figure 35 shows the pressures for the $\alpha = 30^\circ$ and $\beta = 0^\circ$ case. At the section closest to the nose (7.19 in.) the computations predict the pressure level very well near the center section of the body, and underpredict the surface pressure suction levels outboard, where the suction peak

occurs. Moving downstream, the trends are the same, except that the agreement at the center section also becomes less accurate. Figure 36 shows the surface pressure comparisons for the case of $\alpha = 30^\circ$ and $\beta = 10^\circ$. In this case the windward pressure suction levels, as well as the center section pressures are predicted very well by the inviscid computations. The agreement deteriorates at the FS19.94 station, where wing effects not included in the calculation would become important. The leeward pressure levels are poorly predicted at all the stations.

The effect of viscosity on the surface pressure comparisons presented above are given in figures 37 and 38. Including viscosity effects does not improve the agreement. Figure 37 provides the results at zero sideslip. Viscous effects did not change the pressure levels at the mid section of the forebody, but did have a large effect on the peak suction pressure level, reducing the peak pressures and resulting in even worse agreement with the experimental data. The same trend is observed for the results at 10° sideslip, as shown in figure 38.

Due to the disappointing agreement between the experiment and computations, an estimation of the possible effects of the wing on the forebody flowfield was made. To investigate the effect of the wing on the flow over the forebody Lamar's Vortex Lattice code (VLM4997, ref 26) was run for an isolated wing model of the wind tunnel model for the case of $\alpha = 30^\circ$ and $\beta = 0^\circ$. The velocity field due to the wing lift was then computed at the pressure measurement locations. Although approximate, this calculation provides an estimate of the additional induced angle of attack that would exist on the forebody due to the presence of the wing. Two models of the isolated wing were considered, as shown in figure 39. The first model had the leading edge sweep extended to the centerline and the second model had the wing nose clipped at the wing-chine forebody intersection. Using the experimental value of the lift at $\alpha = 30^\circ$, $C_L = 1.0$, the code computed an angle of attack of 26° . Under these conditions the induced angles of attack as computed by the VLM code are given in figure 40. The effect is approximately 1° at FS7.19, 2° at FS13.56, and becomes large at FS19.94, which is very close to the wing.

Based on the induced angle of attack analysis, an inviscid solution was computed using an

additional 2.2° alpha. The resulting 32.2° α would correspond to the corrected α at FS13.56 including wing induced angle of attack effects. The results are shown in figure 41 compared with the results presented above for $\alpha = 30^\circ$ and $\beta = 0^\circ$. Although the results at the first station (where the estimated effect was only 1°) start to show good agreement, the change in the solution at FS13.56 is not enough to attribute the differences to the neglected wing flowfield. Also note that if viscous effects had been included an even greater angle of attack change would be required to obtain agreement with experiment. Thus the wing flowfield effects do not entirely explain the poor agreement between experiment and computation at the suction peak locations.

The flowfield results shown in figures 42 to 53 have been generated as in the case of F-5A using computational flow visualization techniques (PLOT3D). Figure 42 shows the inviscid surface oil flow pattern for $\alpha = 30^\circ$ and $\beta = 0^\circ$. The dye is injected at two different axial stations to observe the formation of separation lines, if any. The inviscid separation can be clearly seen to be occurring at the sharp edges as expected. The turbulent surface flow pattern is completely different, as shown in figure 43 for the same case. The primary separation lines start from the edge as in the case of inviscid flow, and an attachment line occurs at the centerline. However a secondary separation line is shown in the figure.

Figures 44 and 45 show the cross sectional pressure contours at the axial station $x = 13.56$ in. from nose for the inviscid and viscous flows respectively at $\alpha = 30^\circ$ and $\beta = 0^\circ$. The pressures are seen to be symmetrical about the plane of symmetry for both the inviscid and turbulent cases. The vortex pattern and symmetry are more clearly seen in the figures 46 and 47 which are shaded based on the stagnation pressure. The turbulent flow also shows the secondary vortices being shed from under the primary vortices further downstream from the nose.

Figures 48 to 53 show the similar flow visualization pictures for the case of $\alpha = 30^\circ$ and $\beta = 10^\circ$. Figure 48 shows the inviscid surface oil flow pattern. The asymmetry pattern is readily apparent. The lines that end abruptly arise when the streamline reaches the edge of the computational grid. After this photo session we learned how to operate PLOT3D to avoid this

premature termination of the oil flow line. However, the figure demonstrates that the attachment line has shifted due to sideslip. Figure 49 presents the results when viscous effects are included. Qualitatively the results are the same as in the zero sideslip case, but show the asymmetry introduced by the sideslip. Figures 50 and 51 show the pressure contours with the magnitudes of the pressures shown on the left. In both the turbulent and inviscid cases the leeward vortex is farther away from the surface than the windward vortex. Figures 52 and 53 show the stagnation pressure contours, and define the vortex location more precisely.

A MODEL FOR FOREBODY DESIGN: THE GENERIC FOREBODY

Passive tailoring of the aerodynamic properties of forebodies can only be achieved through the geometry of the forebody. As a means of beginning the study of geometry effects on forebody characteristics, a class of shapes possessing the ability to produce shapes of interest has been defined. In particular, the body can be considered to be composed of essentially independent cross-section and planform lines. This forebody makes use of the equation of a super-ellipse to obtain both cross section and planform lines. The super-ellipse can:

- Recover a circular cross-section
- Produce elliptical cross-sections
- Capture the key characteristics of chine forebodies, such as the one tested by Erickson and being used on the YF-23.
- Produce a straight sidewall at the max half breadth line with various slopes
- Be generated by a simple analytical equation

The equation for the forebody cross section is:

$$\left(\frac{z}{b}\right)^{2+n} + \left(\frac{y}{a}\right)^{2+m} = 1$$

where n and m adjustable coefficients. The constants a and b correspond to the max halfbreadth and centerlines respectively. Depending on the value of n and m , the equation can be made to meet all the requirements specified above. The case $n = m = 0$ corresponds to the standard ellipse, where the body is circular when $a = b$. When $n = -1$ the sidewall is linear at the max half breadth line, forming a distinct crease line. When $n < -1$ the body cross-section takes on the cusped or chine-like shape. The derivative of z / b with respect to y / a is:

$$\frac{d\bar{z}}{d\bar{y}} = -\frac{\left(\frac{2+m}{2+n}\right)}{\left[1-\bar{y}^{(2+m)}\right]^{\left(\frac{1+n}{2+n}\right)}}$$

where $\bar{z} = z / b$ and $\bar{y} = y / a$. As $\bar{y} \rightarrow 1$, the slope becomes:

$$\frac{d\bar{z}}{d\bar{y}} = \begin{cases} \infty & n > -1 \\ 0 & n < -1 \\ -(2+m)\bar{y}^{1+m} & n = -1 \end{cases}$$

Extreme flexibility is provided by allowing n, m, a, b to be functions of the axial distance x , and providing for different cross-sections to be used above and below the max half-breadth line. Notice that when $n = -1$ the value of m can be used to control the slope of the sidewall at the crease line.

An example of the range of shapes available within this simple parametric geometry is illustrated in the figures. Figure 54 provides an upper quadrant section to illustrate the manner in

which the cross-section can change from a chine, through the straight line sidewall at the max halfbreadth to the elliptic and even "fuller" elliptic shape originally envisioned for super ellipses simply by changing the value of the exponent coefficient n . As n becomes very large the shape will approach a rectangular cross section. Figure 55 shows the special case where the wall slope is finite and non-zero at the max half-breadth ($n = -1$). In this case the value of the slope is controlled by the value of m . The figure demonstrates the range of control that is available, and the effect of sidewall slope selection on the entire cross-section.

The entire cross section is shown for a series of axial station in figure 56. Figure 56a shows a standard elliptical cross section, with different upper and lower surface centerlines, while figure 56b provides similar results for the case with the straight line side at the max half breadth, and figure 56c provides the equivalent view for the chine shaped case. The range of cross sectional shapes, together with the possibility of allowing them to vary character with axial distance provides an extremely broad design space to investigate aerodynamic tailoring of forebody characteristics through geometric design.

CONCLUSIONS

In this study the use of a Navier-Stokes code to obtain credible results has been demonstrated for high angle of attack forebody aerodynamics at combined angle of attack and sideslip. The F-5A forebody experimental results have been simulated computationally. The computed results nearly duplicated the experimental results. By comparing inviscid and viscous computational solutions the role of viscosity in creating the stabilizing effect of the forebody has been explicitly identified.

When considering extreme forebody shapes such as the Erickson forebody, the code has also been shown to be capable of obtaining solutions in qualitative agreement with measured pressure distributions, although differences between computed and measured pressure distributions remain. Further analysis must be carried out to determine if grid resolution or turbulence model deficiencies

are responsible for the lack of quantitative agreement.

In obtaining the solutions used to determine the directional stability derivatives it was found that the solution had to be "fully converged". Because the derivative was obtained as the difference between two small numbers, the value of $C_{n\beta}$ only started to converge after around 4000 iterations.

An analytic generic forebody model that is extremely versatile yet very simple has been proposed to study the relation between forebody geometry and aerodynamic characteristics.

ACKNOWLEDGEMENTS

The results presented in this report were obtained with the help of many other people. At NASA Langley: Sue Grafton provided us with the forebody from the wind tunnel model of the F-5A. Robert Hall gave us geometry data on the Erickson forebody and notes defining the original geometric concept. Gary Erickson provided us with tabulated pressure coefficients for his famous chine forebody. Ed Waggoner, James Luckring, Robert Hall and Farhad Ghaffari each helped us get up and keep going on the NASA computing system. At Northrop, Tom Heglund provided us with detailed F-5A lofting information. At VPI & SU, Robert Walters consulted with us regularly on the use of `cf13d`, and William McGrory provided us with his grid generator. Each of these contributions is gratefully acknowledged.

APPENDIX A
 MODIFICATIONS TO **cf13d** (version 1.1)

The following modifications and additions were made to **cf13d** (version 1.1)

Where : bc.f ; *subroutine* bc

Purpose : Periodic boundary condition at the grid interface of a wraparound grid used for flows with sideslip

New :

```
if (mtypej(1).eq.2001 .or. mtypej(2).eq.2001)
. call bc2001(jdim,kdim,ldim,w(lq),w(lqj0),w(lqk0),w(lqi0),
. w(lsj),w(lsk),w(lsi))
```

Where : bc.f ; *completely new subroutine*

Purpose : Periodic boundary condition at the grid interface of a wraparound grid used for flows with sideslip

New :

```
subroutine bc2001(jdim,kdim,ldim,q,qj0,qk0,qi0,sj,sk,si)
```

```
common / reyue / ivisc(3),reue,tinf,isnd,c2spe
```

c

```
common /info/ title(20),xmach,alpha,beta,nit,ntt,dt,fmax,idiag(3),
. nitfo,iflagts,rkap(3),istrag,impl,iru,nju,ijac,iaf,nres,iafa,
. levelb(5),mgflag,iconsf,mseq,ncycl(5),levelt(5),nitfol(5),mmx,
. imesh,ngam,nsm(5),iflim(3)
```

```
common/fluid/gamma,gml,gpl,gmlg,gplg,ggml
```

```
common/ivals/p0,rho0,c0,u0,v0,w0,et0,h0,pt0,qiv(5)
```

```
common /te/ jtel,jte2,ktel,kte2,itel,ite2
```

c

```
common/bv/ibci(2),ibcj(2),ibck(2),ibcmi(5,2),ibcmj(5,2),ibcmk(5,2)
```

```

common /type/ mtypej(2),mtypek(2),mtypei(2)
c
common/unst/iunst,time,rfreq,alf,alphau,cloc,rfreq0
common /sklton/ isklton
c
dimension q(jdim,kdim,ldim,5),qi0(jdim,kdim,5,4),
.          qj0(kdim,ldim-1,5,4),qk0(jdim,ldim-1,5,4)
dimension sk(jdim,kdim,ldim-1,5),
.si(jdim,kdim,ldim,5),sj(jdim,kdim,ldim-1,5)
dimension tsym(5)
data tsym / 1.e0,1.e0,-1.e0,1.e0,1.e0 /
c
jdim1=jdim-1
kdim1=kdim-1
ldim1=ldim-1
c
c
c
c          * * * * *
c          * yawed flow boundary condition mtype=2001 *
c          * * * * *
c
c*****
c      j=1 boundary          flow across x-z plane          mtype 2001
c*****
c
c      reflection - symmetry plane  j=0/j=jdim
c
      if (mtypej(1).eq.2001) then
      if (isklton.eq.1) write(11,*)
      .' j=1 boundary flow across x-z plane from j = jdim  mtype 2001'
      do 38 i=1,ldim1
      do 38 l=1,5
      do 38 k=1,kdim1
      qj0(k,i,l,1) = q(jdim-1,k,i,l)
      qj0(k,i,l,2) = q(jdim-2,k,i,l)
38 continue
      end if
c

```

```

c*****
c      j=jdim boundary      flow across  x-z plane      mtype 2001
c*****
c
c      reflection - symmetry plane  j=0/j=jdim
c
      if (mtypej(2).eq.2001) then
      if (isklton.eq.1) write(11,*)
      .' j=jdim boundary  flow across x-z plane from j = 1  mtype 2001'
      do 39 i=1, idim1
      do 39 l=1, 5
      do 39 k=1, kdim1
      qj0(k,i,l,3) = q(1,k,i,l)
      qj0(k,i,l,4) = q(2,k,i,l)
39 continue
      end if
      return
      end

```

Where : cbsem.f ; *subroutine* plot3d

Purpose : Calculate and print coefficient of pressure C_p instead of p/p_∞

Old :

```

      write(17,29) i, j, k, x(j,k,i), y(j,k,i), z(j,k,i),
      .
      q2, q3, q4, q5, t1, xml, pitot, edvis

```

New :

```

      cp          = 2.0/gamma/xmach**2*(q5 - 1.0)
      write(17,29) i, j, k, x(j,k,i), y(j,k,i), z(j,k,i),
      .
      q2, q3, q4, cp, t1, xml, pitot, edvis

```

Where : cbsem.f ; *subroutine* plot3d

Purpose : At a corner point, for wraparound grids, this is more appropriate

Old :

```

      if (k.eq.kdim) kd = kdim1

```

```

      if (j.eq.1 .or. j.eq.jdim) then
        if (j.eq.jdim) jd = jdim1
c       corner points
        xw(jw,kw,iw,1) = 0.5*(q(jd,kd,id,1)+q(jd,kd,id1,1))

```

New :

```

      m=2
      if (k .eq. kdim ) m=4
      if (j .eq. 1)
c       xw(jw,kw,iw,1)=.25*(qk0(jd,id,1,m) +qk0(jdim1,id,1,m)
c       + qk0(jd,id1,1,m) + qk0(jdim1,id1,1,m))
      if (j .eq. jdim)
c       xw(jw,kw,iw,1)=.25*(qk0(jd,id,1,m) +qk0(1,id,1,m)
c       + qk0(jd,id1,1,m) + qk0(1,id1,1,m))

```

Where : lbcx.f ; *subroutine* force

Purpose : Calculate yawing moment

Old :

```

      subroutine force(jdim,kdim,idim,x,y,z,sk,q,
c       .cl,cd,cz,cm,chd,swet,i00,ub,vb,wb,vmu,vol)
c
c*****
c       Purpose: Integrate the forces on the body.
c*****
c
c       implicit half precision(a-h,o-z)
c       common /fsum/ sref,cref,bref,xmc,ymc,zmc
c       common/ivals/p0,rho0,c0,u0,v0,w0,et0,h0,pt0,qiv(5)
c       dimension ub(jdim*kdim,1),vb(jdim*kdim,1),
c       +wb(jdim*kdim,1),vmu(jdim-1,1),vol(jdim*kdim,1)
c       common /te/ jtel,jte2,ktel,kte2,itel,ite2
c       common /info/ title(20),xmach,alpha,beta,nit,ntt,dt,fmax,idiag(3),
c       . nitfo,iflagts,rkap(3),istrag,impl,iru,nju,ijac,iaf,nres,iafa,
c       . levelb(5),mgflag,iconsf,mseq,ncycl(5),levelt(5),nitfol(5),mmx,

```

```

. imesh,ngam,nsm(5),iflim(3)
dimension x(jdim,kdim,ldim),y(jdim,kdim,ldim),z(jdim,kdim,ldim)
dimension sk(jdim*kdim,ldim-1,5),q(jdim,kdim,ldim,5)
common/fluid/gamma,gml,gpl,gmlg,gplg,ggml
common / reue / ivisc(3),reue,tinf,lsnd,c2spe
c
common/unst/iunst,time,rfreq,alf,alphau,cloc,rfreq0
c
al=alpha+alf
c
cpc=2.e0/(gamma*xmach*xmach)
c
cosa=cos(al)
sina=sin(al)
c
cl=0.e0
cd=0.e0
cz=0.e0
cm=0.e0
chd= 0.e0
swet=0.e0
ist=itel
ifn=ite2-1
jte21=jte2-1
const=4./(reue*xmach)
do 9000 i=ist,ifn
cxl=0.e0
cyl=0.e0
czl=0.e0
cml=0.e0
chdl=0.e0
xas=0.e0
yas=0.e0
zas=0.e0
swetl=0.e0
jte21=jte2-1
do 50 j=jtel,jte21
c
xa=.25e0*( x(j,1,i) + x(j+1,1,i) + x(j,1,i+1) + x(j+1,1,i+1) )

```

```

ya=.25e0*( y(j,1,i) + y(j+1,1,i) + y(j,1,i+1) + y(j+1,1,i+1) )
za=.25e0*( z(j,1,i) + z(j+1,1,i) + z(j,1,i+1) + z(j+1,1,i+1) )
xas=xas+xa
yas=yas+ya
zas=zas+za

c
dcp=-(q(j,1,i,5)/p0-1.e0)*cpc*sk(j,i,4)
dcx=dcp*sk(j,i,1)
dcy=dcp*sk(j,i,2)
dcz=dcp*sk(j,i,3)

c
if (ivisc(3).gt.0) then
tau=vmu(j,i)*const/vol(j,i)*sk(j,i,4)**2
vnorm=ub(j,i)*sk(j,i,1)+vb(j,i)*sk(j,i,2)+wb(j,i)*sk(j,i,3)
dcx=dcx+tau*(ub(j,i)-vnorm*sk(j,i,1))
dcz=dcz+tau*(wb(j,i)-vnorm*sk(j,i,3))
dcy=dcy+tau*(vb(j,i)-vnorm*sk(j,i,2))
end if

c
chdl=chdl+abs(sk(j,i,3))*sk(j,i,4)
swetl=swetl+sk(j,i,4)
cxl=cxl+dcx
cyl=cyl+dcy
czl=czl+dcz
50 cml=cml-dcz*(xa-xmc)+dcx*(za-zmc)
xas=xas/float(jte2-jte1)
yas=yas/float(jte2-jte1)
zas=zas/float(jte2-jte1)
cds= cxl*cosa+czl*sina
cls=-cxl*sina+czl*cosa
cms=cml
chds=chdl
swets=swetl
cl=cl+cls
cd=cd+cds
cz=cz+czl
cm=cm+cms
chd=chd+chds
swet=swet+swets
if(ntt.le.1 .or. i00.eq.1) then

```

```

c
    if(chds.le.0.) chds=1.
    cls=2.0*cls/chds
    cds=2.0*cds/chds
    czl=2.0*czl/chds
    cyl=2.0*cyl/chds
c
    if(i.eq.ist) write(11,8613)
8613 format(/30x,41hSUMMARY OF I=CONSTANT K=1 SECTIONAL LOADS,/,
    . 23x,54hSref-s is 1/2 projected area in X-Y plane, if positive)
    if(i.eq.ist) write(11,8713)
8713 format(/1x,2x,1hI,5x,6hXavg-s,6x,6hYavg-s,6x,6hZavg-s,6x,
    .6hSref-s,6x,6hSwet-s,7x,4hCl-s,8x,4hCd-s,8x,4hCz-s,
    .8x,4hCy-s,7x,7hRe-Xavg)
c
    xrep      = reue*xas
    write(11,1318) i,xas,yas,zas,
    .chds,swets,cls,cds,czl,cyl,xrep
1318 format(1x,i3,10e12.3)
c
    end if
9000 continue
    return
end

```

New :

```

    subroutine force(jdim,kdim,ldim,x,y,z,sk,q,
    .cl,cd,cz,cm,cx,cy,cn, chd, swet, i00, ub, vb, wb, vmu, vol)
c
c*****
c Purpose: Integrate the forces on the body.
c*****
c
c implicit half precision(a-h,o-z)
common /fsum/ sref,cref,bref,xmc,ymc,zmc
common/ivals/p0,rho0,c0,u0,v0,w0,et0,h0,pt0,qiv(5)

```

```

dimension ub(jdim*kdim,1),vb(jdim*kdim,1),
+wb(jdim*kdim,1),vmu(jdim-1,1),vol(jdim*kdim,1)
common /te/ jte1,jte2,kte1,kte2,ite1,ite2
common /info/ title(20),xmach,alpha,beta,nit,ntt,dt,fmax,idiag(3),
. nitfo,iflagts,rkap(3),istrag,impl,iru,nju,ijac,iaf,nres,iafa,
. levelb(5),mgflag,iconsf,mseq,ncycl(5),levelt(5),nitfol(5),mmx,
. imesh,ngam,nsm(5),iflim(3)
dimension x(jdim,kdim,ldim),y(jdim,kdim,ldim),z(jdim,kdim,ldim)
dimension sk(jdim*kdim,ldim-1,5),q(jdim,kdim,ldim,5)
common/fluid/gamma,gml,gpl,gmlg,gplg,ggml
common / reue / ivisc(3),reue,tinf,isnd,c2spe
c
common/unst/iunst,time,rfreq,alf,alphau,cloc,rfreq0
c
al=alpha+alf
c
cpc=2.e0/(gamma*xmach*xmach)
c
cosa=cos(al)
sina=sin(al)
c
c1=0.e0
cd=0.e0
cx=0.e0
cy=0.e0
cz=0.e0
cm=0.e0
cn=0.e0
chd= 0.e0
swet=0.e0
ist=ite1
ifn=ite2-1
jte21=jte2-1
const=4./(reue*xmach)
do 9000 i=ist,ifn
cxl=0.e0
cyl=0.e0
czl=0.e0
cml=0.e0
cnl=0.e0

```

```

chdl=0.e0
xas=0.e0
yas=0.e0
zas=0.e0
swetl=0.e0
jte21=jte2-1
do 50 j=jtel,jte21
c
xa=.25e0*( x(j,1,i) + x(j+1,1,i) + x(j,1,i+1) + x(j+1,1,i+1) )
ya=.25e0*( y(j,1,i) + y(j+1,1,i) + y(j,1,i+1) + y(j+1,1,i+1) )
za=.25e0*( z(j,1,i) + z(j+1,1,i) + z(j,1,i+1) + z(j+1,1,i+1) )
xas=xas+xa
yas=yas+ya
zas=zas+za
c
dcp=-(q(j,1,i,5)/p0-1.e0)*cpc*sk(j,i,4)
dcx=dcp*sk(j,i,1)
dcy=dcp*sk(j,i,2)
dcz=dcp*sk(j,i,3)
c
if (ivisc(3).gt.0) then
tau=vmu(j,i)*const/vol(j,i)*sk(j,i,4)**2
vnorm=ub(j,i)*sk(j,i,1)+vb(j,i)*sk(j,i,2)+wb(j,i)*sk(j,i,3)
dcx=dcx+tau*(ub(j,i)-vnorm*sk(j,i,1))
dcz=dcz+tau*(wb(j,i)-vnorm*sk(j,i,3))
dcy=dcy+tau*(vb(j,i)-vnorm*sk(j,i,2))
end if
c
chdl=chdl+abs(sk(j,i,3))*sk(j,i,4)
swetl=swetl+sk(j,i,4)
cxl=cxl+dcx
cyl=cyl+dcy
czl=czl+dcz
cnl=cnl-dcy*(xa-xmc)+dcx*(ya-ymc)
50 cml=cml-dcz*(xa-xmc)+dcx*(za-zmc)
xas=xas/float(jte2-jtel)
yas=yas/float(jte2-jtel)
zas=zas/float(jte2-jtel)
cds= cxl*cosa+czl*sina

```

```

cls=-cxl*sina+czl*cosa
cms=cml
chds=chdl
swets=swetl
cl=cl+cls
cd=cd+cds
cx=cx+cxl
cy=cy+cyl
cz=cz+czl
cm=cm+cms
cn=cn+cnl
chd=chd+chds
swet=swet+swets
if(ntt.le.1 .or. i00.eq.1) then
c
  if(chds.le.0.) chds=1.
  cls=2.0*cls/chds
  cds=2.0*cds/chds
  czl=2.0*czl/chds
  cyl=2.0*cyl/chds
c
  if(i.eq.ist) write(11,8613)
8613 format(/30x,41hSUMMARY OF I=CONSTANT K=1 SECTIONAL LOADS,/,
. 23x,54hSref-s is 1/2 projected area in X-Y plane, if positive)
  if(i.eq.ist) write(11,8713)
8713 format(/1x,2x,1hI,4x,6hXavg-s,5x,6hYavg-s,5x,6hZavg-s,5x,
.6hSref-s,5x,6hSwet-s,6x,4hCl-s,7x,4hCn-s,7x,4hCx-s,7x,4hCz-s,
.7x,4hCy-s,6x,7hRe-Xavg)
c
  xrep      = reue*xas
  write(11,1318) i,xas,yas,zas,
. chds,swets,cls,cnl,cxl,czl,cyl,xrep
1318 format(1x,i3,11e11.3)
c
  end if
9000 continue
  return
end

```

Where : rhs.f ; subroutine resp

Purpose : Calculate and print block summary of axial, normal and side forces and also of yawing moment

Old :

```
      call force(jdim,kdim,ldim,x,y,z,sk,q,
. cl,cd,czz,cm, chd, swet, icall, q(1,2), q(1,3), q(1,4), vmu, vol)
c
      clt      = cl/sref
      cmt      = cm/(sref*cref)
      cdt      = cd/sref
c
c      print block summary
c
      if (icyc.le.1 .or. icyc.eq.ncyc) then
      write(11,677) nbl
677 format (/10x,37hSUMMARY OF FORCES AND MOMENTS - BLOCK,i5)
      write(11,603)
603 format (/1x,11hwetted area,2x,14hX-Y proj. area,
.          5x,4hCL-b,10x,4hCD-b,10x,4hCM-b)
      write(11,653) swet, chd, clt, cdt, cmt
653 format (1x,e12.5,4(2x,e12.5))
      end if
c
c      sum contributions of blocks on global level in clw,cdw
c
      if (level.eq.lglobal) then
      chdgp     = chdgp     + chd
      swetgp    = swetgp    + swet
      clw(nres) = clw(nres) + clt
      cmgp      = cmgp      + cmt
      cdw(nres) = cdw(nres) + cdt
      end if
c
c      print summary of global blocks
c
      if (icyc.le.1 .or. icyc.eq.ncyc) then
      if(nbl .eq. lblock) then
      write(11,777)
```

```

777 format (/10x,49hSUMMARY OF FORCES AND MOMENTS - ALL GLOBAL BLOCKS)
      write(11,703)
703 format (/1x,11hwetted area,2x,14hX-Y proj. area,
.         6x,2hCL,12x,2hCD,12x,2hCM)
      write(11,653) swetgp, chdgp, clw(nres), cdw(nres), cmgp
      end if
      end if
670 continue
c
      irite=1
      if(irite .eq. 1 .and. iunst .gt. 0) then
      call prntcp(jdim,kdim, idim,wk,q)
      end if
c
c      print residual and lift
c
      if (icyc.eq.1 .or. (icyc.eq.2 .and. nbl.eq.lblock)
. .or. icyc.eq.ncyc) then
      if(iunst .lt. 2) then
      write(11,5002)
5002 format (/1x,5hlevel,1x,5hblock,1x,9hiteration,3x,
.         8hresidual,4x,10htotal res.,3x,7hrkap(i),3x,7hrkap(j),
.         3x,7hrkap(k),3x,10hlift coef.,3x,10hdrag coef.)
c
      else
      write(11,4682)
4682 format (/1x,5hlevel,1x,5hblock,1x,9hiteration,3x,
.         8hresidual,4x,10htotal res.,3x,7hrkap(i),3x,7hrkap(j),
.         3x,7hrkap(k),3x,10hlift coef.,3x,10hdrag coef.,
.         4x,4htime,6x,5halpha)
      end if
      end if
      if (icyc.eq.1 .or. (icyc.ge.2 .and. nbl.eq.lblock)
. .or. icyc.eq.ncyc) then
      if(iunst .lt. 2) then
      write(11,5001) level,nbl,nres,rmst,rms(nres),rkap,
.         clw(nres),cdw(nres)
5001 format (1x,i5,1x,i5,3x,i5,2x,e12.5,1x,e12.5,2x,f6.2,
.         4x,f6.2,4x,f6.2,3x,e12.5,1x,e12.5)

```

```

else
alot=(alpha+alf)*57.2958
write(11,4683) level,nbl,nres,rmst,rms(nres),rkap,
.           clw(nres),cdw(nres),time,alot
4683 format(1x,i5,1x,i5,3x,i5,2x,e12.5,1x,e12.5,2x,f6.2,
.           4x,f6.2,4x,f6.2,3x,e12.5,1x,e12.5,1x,f9.4,1x,e11.4)
end if
end if

```

c

```

if(nbl.eq.lblock) then
chdgp      = 0.
swetgp     = 0.
cmgp       = 0.
end if
67 continue

```

New :

```

call force(jdim,kdim,idim,x,y,z,sk,q,cl,cd,cz,cm,
. cx,cy,cn,chd,swet,icall,q(1,2),q(1,3),q(1,4),vmu,vol)

```

c

```

clt        = cl/sref
cmt        = cm/(sref*cref)
cdt        = cd/sref
cxt        = cx/sref
czt        = cz/sref
cyt        = cy/sref
cnt        = cn/(sref*bref)

```

c

c print block summary

c

```

if(icyc.le.1 .or. icyc.eq.ncyc) then
write(11,677) nbl
677 format(/10x,37hSUMMARY OF FORCES AND MOMENTS - BLOCK,i5)
write(11,603)

603 format(/1x,11hwetted area,2x,14hX-Y proj. area,4x,4hCL-b,
. 9x,4hCD-b,9x,4hCM-b,9x,4hCX-b,9x,4hCY-b,9x,4hCZ-b,9x,4hCN-b)
write(11,653) swet,chd,clt,cdt,cmt,cxt,cyt,czt,cnt

```

```

653 format (1x,e12.5,8(2x,e11.4))
    end if
c
c   sum contributions of blocks on global level in clw,cdw
c
    if (level.eq.lglobal) then
    chdgp      = chdgp      + chd
    swetgp     = swetgp     + swet
    clw(nres)  = clw(nres)  + clt
    cmgp       = cmgp       + cmt
    cdw(nres)  = cdw(nres)  + cdt
    cxgp       = cxgp       + cxt
    czgp       = czgp       + czt
    cygp       = cygp       + cyt
    cngp       = cngp       + cnt
    end if
c
c   print summary of global blocks
c
    if (icyc.le.1 .or. icyc.eq.ncyc) then
    if(nbl .eq. lblock) then
    write(11,777)
777 format (/10x,49hSUMMARY OF FORCES AND MOMENTS - ALL GLOBAL BLOCKS)
    write(11,703)
703 format (/1x,11hwetted area,2x,14hX-Y proj. area,
.          5x,2hCL,11x,2hCD,11x,2hCM,11x,2hCX,11x,2hCY,
.          11x,2hCZ,11x,2hCn)
    write(11,653) swetgp, chdgp, clw(nres), cdw(nres), cmgp, cxgp, cygp,
.          czgp, cngp
    end if
    end if
670 continue
c
    irite=1
    if(irite .eq. 1 .and. iunst .gt. 0) then
    call prntcp(jdim,kdim, idim,wk,q)
    end if
c
c   print residual and lift
c

```

```

        if (icyc.eq.1 .or. (icyc.eq.2 .and. nbl.eq.lblock)
        . .or. icyc.eq.ncyc) then
            if(iunst .lt. 2) then
                write(11,5002)
5002 format (/1x,5hlevel,1x,5hblock,1x,9hiteration,3x,
        .      8hresidual,4x,10htotal res.,3x,7hrkap(i),3x,7hrkap(j),
        .      3x,7hrkap(k),3x,10hlift coef.,3x,10hdrag coef.,
        .      3x,7h cy ,3x,7hcn )
c
            else
                write(11,4682)
4682 format (/1x,5hlevel,1x,5hblock,1x,9hiteration,3x,
        .      8hresidual,4x,10htotal res.,3x,7hrkap(i),3x,7hrkap(j),
        .      3x,7hrkap(k),3x,10hlift coef.,3x,10hdrag coef.,
        .      4x,4htime,6x,5halpha)
            end if
            end if
            if (icyc.eq.1 .or. (icyc.ge.2 .and. nbl.eq.lblock)
            . .or. icyc.eq.ncyc) then
                if(iunst .lt. 2) then
                    write(11,5001) level,nbl,nres,rmst,rms(nres),rkap,
        .                      clw(nres),cdw(nres),cygp,cngp
5001 format (1x,i5,1x,i5,3x,i5,2x,e12.5,1x,e12.5,2x,f6.2,
        .      4x,f6.2,4x,f6.2,3x,e12.5,1x,e12.5,1x,e12.5,1x,e12.5)
                else
                    alot=(alpha+alf)*57.2958
                    write(11,4683) level,nbl,nres,rmst,rms(nres),rkap,
        .                      clw(nres),cdw(nres),time,alot
4683 format (1x,i5,1x,i5,3x,i5,2x,e12.5,1x,e12.5,2x,f6.2,
        .      4x,f6.2,4x,f6.2,3x,e12.5,1x,e12.5,1x,f9.4,1x,e11.4)
                end if
            end if
c
            if(nbl.eq.lblock) then
                chdgp      = 0.
                swetgp     = 0.
                cmgp       = 0.
                cxgp       = 0.
                cygp       = 0.

```

```
        czgp      = 0.  
        cngp      = 0.  
    end if  
67 continue
```

Where : rhs.f ; *subroutine* turb

Purpose : Correction to the value of parameter *cwk* used in Baldwin Lomax model (AIAA
78-257) which was incorrect

Old :

```
data aplus/26.e0/,ccp/1.6e0/,ckleb/.3e0/,cwk/.25e0/,vk/.4e0/,  
.      clauser/.0180e0/
```

New :

```
data aplus/26.e0/,ccp/1.6e0/,ckleb/.3e0/,cwk/1.0e0/,vk/.4e0/,  
.      clauser/.0180e0/
```

Where : rhs.f ; *subroutine* turb

Purpose : Change initialized value of *fblmax* to avoid division by zero. More of a
precautionary measure as suggested by Dr. R.W.Walters

Old :

```
fblmax = 0.
```

New :

```
fblmax = 1.e-10
```

APPENDIX B

F-5A FOREBODY GEOMETRY MATH MODEL

The F-5A forebody math model was constructed using conic lofting techniques (ref 7) based on lofting information provided by Tom Heglund of Northrop, and verified by comparison with an actual nose provided by Sue Grafton. The computational model was extended to 225 in. (without the canopy) which was beyond the length of the wind tunnel model (175 in.).

```

      program f5agrid ( F-5A forebody math model )
c      F-5A forebody surface geometry and grid definition.

c      R.Ravi, August 1989
c      program generates the control and maximum half breadth points at
c      various cross sections as suggested by Tom Heglund of Northrop
c      and then generates the cross sectional shape using conic lofting
c      techniques (ref. 24 )
c
c      It also generates the F-5A surface grid and uses this
c      information to generate the input to the grid generator
c      which in our case was GRIDTOOL
c
c      The length of the computational model was 225 in.(canopy
c      not included)
c
c      It scales down the surface co-ordinates to compare with
c      Sue Graftons F-5A wind tunnel model
c
c      It finally writes down the surface co-ordinates in PLOT3D format
c
c
      dimension x(100,10),y(100),z(100,10),x1(100,100),x2(100,100),
1      z1(100,100),z2(100,100),xxx(100,100,1),yyy(100,100,1)
2      ,zzz(100,100,1),xx2(100,100),zz2(100,100),yext(15)
```

```

3  ,slope1(100,100),curv(100,100),s(100)
c  open(7,file='f5asurface.out')
   open(10,file='f5asurface.plot3d')
   open(11,file='f5asurface.compare')
   open(13,file='test')
   open(14,file='slopes')
   open(15,file='curv')
   open(12,file='fbody.gridgen')
   open(16,file='report')
   pi=acos(-1.)

C
C  IEXT  = NUMBER OF AXIAL STATIONS AHEAD OF THE NOSE
C        INCLUDING THE NOSE STATION
C
C  JDIM  = NUMBER OF POINTS FROM THE TOP CENTER LINE
C        TO THE POINT WHERE THE FLAT SURFACE STARTS
C
C  YAHEAD = DISTANCE AHEAD OF THE NOSE FROM WHERE
C        SUBSONIC GRID STARTS
C

   jdim=25
   jdiminit=jdim
   iext=10
   j2=jdim*2-1
   j2init=j2
   yahead=100.0
   y(1)=42.50
   y(2)=42.55
   y(3)=42.60
   y(4)=42.65
   y(5)=42.70
   y(6)=42.75
   y(7)=42.80
   y(8)=42.85
   y(9)=42.90
   y(10)=42.95
   y(11)=43.00
   y(12)=43.50
   y(13)=44.00
   y(14)=44.50
   y(15)=45.00
   y(16)=45.50

```

y(17)=46.00
y(18)=47.00
y(19)=48.00
y(20)=49.00
y(21)=50.00
y(22)=52.00
z(1,1)=-8.589
z(1,6)=-8.589
z(2,1)=-8.464
z(2,6)=-8.745
z(3,1)=-8.408
z(3,6)=-8.811
z(4,1)=-8.364
z(4,6)=-8.861
z(5,1)=-8.326
z(5,6)=-8.904
z(6,1)=-8.291
z(6,6)=-8.942
z(7,1)=-8.259
z(7,6)=-8.977
z(8,1)=-8.230
z(8,6)=-9.008
z(9,1)=-8.201
z(9,6)=-9.038
z(10,1)=-8.175
z(10,6)=-9.066
z(11,1)=-8.149
z(11,6)=-9.092
z(12,1)=-7.929
z(12,6)=-9.308
z(13,1)=-7.745
z(13,6)=-9.477
z(14,1)=-7.581
z(14,6)=-9.621
z(15,1)=-7.428
z(15,6)=-9.749
z(16,1)=-7.283
z(16,6)=-9.867
z(17,1)=-7.145

```

z(17,6)=-9.976
z(18,1)=-6.884
z(18,6)=-10.175
z(19,1)=-6.636
z(19,6)=-10.356
z(20,1)=-6.4
z(20,6)=-10.523
z(21,1)=-6.171
z(21,6)=-10.68
z(22,1)=-5.721
z(22,6)=-10.98
x(1,3)=0.0
x(2,3)=-0.175
x(3,3)=-.251
x(4,3)=-.311
x(5,3)=-.363
x(6,3)=-.409
x(7,3)=-.452
x(8,3)=-.491
x(9,3)=-.528
x(10,3)=-.564
x(11,3)=-.598
x(12,3)=-0.884
x(13,3)=-1.118
x(14,3)=-1.326
x(15,3)=-1.517
x(16,3)=-1.696
x(17,3)=-1.866
x(18,3)=-2.185
x(19,3)=-2.484
x(20,3)=-2.768
x(21,3)=-3.041
x(22,3)=-3.577
z(1,3)=-8.589
z(22,3)=-8.147
do 3 i=2,21
slope=(z(22,3)-z(1,3))/(y(22)-y(1))
z(i,3)=z(1,3)+(slope*(y(i)-y(1)))
continue
do 5 i=1,22

```

3

5

```

x(i,1)=0.0
x(i,6)=0.0
continue
idim=11
iidim=22+idim-1
y(22)=52.0
y(iidim)=125.00
dely=(y(iidim)-y(22))/(idim-1)
do 10 i=22,iidim
x(i,1)=0.0
x(i,6)=0.0
y1=.01*(y(i)-38.5)
a1=-.08815+.235*y1-.04904*(y1**2.)
a2=.0457594*(y1**3.)-0.0294590*(y1**4.)+.0077218*(y1**5.)
a3=-0.000571*(y1**6.)
z(i,1)=(a1+a2+a3)/.01
b1=-.08815-.17125*y1+.068785*(y1**2.)+.1089634*(y1**3.)
b2=-.1823104*(y1**4.)+.110555*(y1**5.)-.0242660*(y1**6.)
z(i,6)=(b1+b2)/.01
y3=(y(i)-42.5)*0.01
a4=.0065+.213*y3-.269652*(y3**3)+.3669951*(y3**4)-.25149*(y3**5)
a5=.0874987*(y3**6.)-.0120677*(y3**7.)
x(i,2)=-1.0*(a4+a5)/.01
if ((y(i) .ge. 52.0) .and. (y(i) .le. 70.0)) then
    z(i,2)=-15.551+.1746575*y(i)
    x(i,5)=-1.0*(-7.37+.191*y(i))
    x(i,3)=-1.0*(-10.35644+.2679492*y(i))
    x(i,4)=x(i,3)
else
    y4=.01*(y(i)-70.0)
    z(i,2)=-.03325+.1746575*y4+.0215199*(y4**3.)/.01
    b4=.06+.191*y4-1.1941603*(y4**3.)+3.5325676*(y4**4.)
    b5=-4.7103427*(y4**5)+2.9985414*(y4**6)-.7374221*(y4**7)
    x(i,5)=-1.*(b4+b5)/.01
    e1=.084+.2679492*y4-2.0762353*(y4**3)+8.9749473*(y4**4)
    e2=-19.2071906*(y4**5.)+20.6116655*(y4**6.)
    e3=-8.8061808*(y4**7.)
    x(i,3)=-1.*(e1+e2+e3)/.01
    x(i,4)=x(i,3)

```

```

endif
y5=.01*(y(i)-42.5)
b6=-.09175-.096*y5+.3283568*(y5**3.)-.8070199*(y5**4.)
b7=.8932135*(y5**5.)-.4656938*(y5**6.)+.0929695*(y5**7.)
z(i,5)=(b6+b7)/.01
z(i,3)=-11.0949+.0589595*y(i)
z(i,4)=z(i,3)
y(i+1)=y(i)+dely
10 continue
idim1=7
iidim1=iidim+idim1-1
y(iidim)=125.00
y(iidim1)=175.00
dely=(y(iidim1)-y(iidim))/(idim1-1)
do 20 i=iidim,iidim1
x(i,1)=0.0
x(i,6)=0.0
y1=.01*(y(i)-125.)
c1=.095056+.1965665*y1-.017364*(y1**2.)-.1030717*(y1**3.)
c2=.8564063*(y1**4.)-2.0571887*(y1**5.)+1.5294378*(y1**6.)
z(i,1)=(c1+c2)/.01
y2=.01*(y(i)-38.5)
d1=-.08815-.17125*y2+.068785*(y2**2.)+.1089634*(y2**3.)
d2=-.1823104*(y2**4.)+.110555*(y2**5.)-.024266*(y2**6.)
z(i,6)=(d1+d2)/.01
y3=(y(i)-42.5)*0.01
b4=.0065+.213*y3-.269652*(y3**3)+.3669951*(y3**4)-.25149*(y3**5)
b5=.0874987*(y3**6.)-.0120677*(y3**7.)
x(i,2)=-1.*(b4+b5)/0.01
y4=.01*(y(i)-125.0)
d3=.066392+.1941868*y4+.0645597*(y4**2.)-.3888642*(y4**3.)
d4=2.6147284*(y4**4.)-6.9406616*(y4**5.)+5.5973024*(y4**6.)
z(i,2)=(d3+d4)/.01
y5=.01*(y(i)-70.0)
b6=.06+.191*y5-1.1941603*(y5**3.)+3.5325676*(y5**4.)
b7=-4.7103427*(y5**5.)+2.9985414*(y5**6.)-.7374221*(y5**7.)
x(i,5)=-1.*(b6+b7)/.01
y6=.01*(y(i)-42.5)
b8=-.09175-.096*y6+.3283568*(y6**3.)-.8070199*(y6**4.)

```

```

b9=.8932135*(y6**5.)-.4656938*(y6**6.)+.0929695*(y6**7.)
z(i,5)=(b8+b9)/.01
y7=.01*(y(i)-72.3)
e1=.09025+.2679492*y7-.252125*(y7**2.)+.1235176*(y7**3.)
e2=-.0352414*(y7**4.)+.005155*(y7**5.)
x(i,3)=-1.*(e1+e2)/.01
x(i,4)=x(i,3)
y1=.01*(y(i)-125.)
e3=-.03725+.0589595*y1+13.7487102*(y1**3.)-98.7915275*(y1**4.)
e4=300.6858408*(y1**5.)-430.699982*(y1**6.)+236.8200513*(y1**7.)
z(i,3)=(e3+e4)/.01
if (y(i) .le. 150.) then
    y1=.01*(y(i)-125.)
    e5=-.03725+.0589595*y1-.05*(y1**2.)-8.9138868*(y1**3.)
    e6=65.1205618*(y1**4.)-191.1452871*(y1**5.)
    e7=207.4735881*(y1**6.)
    z(i,4)=(e5+e6+e7)/.01
else
    y8=.01*(y(i)-150.)
    e8=-.04655-.085*y8-.025*(y8**2.)+1.1163*(y8**3.)
    e9=-16.0196*(y8**4.)+79.9248*(y8**5.)-121.056*(y8**6.)
    z(i,4)=(e8+e9)/.01
endif
y(i+1)=y(i)+dely
20 continue
idim2=6
iidim2=iidim1+idim2
y(iidim1)=175.00
y(iidim2)=225.0
dely=(y(iidim2)-y(iidim1))/(iidim2-iidim1)
do 700 i=iidim1,iidim2
x(i,1)=0.0
y10=.01*(y(i)-175.0)
g1=.18925+.174*y10-.025*(y10**2.)-.0891784*(y10**3.)
g2=-.404712*(y10**4.)+1.3978099*(y10**5.)-1.4735205*(y10**6.)
g3=.5163509*(y10**7.)
z(i,1)=(g1+g2+g3)/.01
x(i,6)=0.0
y11=(y(i)-175.)*.01
g4=-.1826+.025*(y11**2.)+.000825*(y11**3.)

```

```

g5=-.00451*(y11**4.)-.00006*(y11**5.)
z(i,6)=(g4+g5)/.01
if ( y(i) .ge. 175. .and. y(i) .le. 220.) then
    y12=.01*(y(i)-42.5)
    g6=.0065+.213*y12-.2696520*(y12**3.)+.3669951*(y12**4.)
    g7=-.25149*(y12**5)+.0874987*(y12**6)-.0120677*(y12**7)
    x(i,2)=-1.*(g6+g7)/.01
    y13=.01*(y(i)-72.3)
    g10=.09025+.267949*y13-.25212*(y13**2)+.1235176*(y13**3)
    g11=-.0352414*(y13**4.)+.005155*(y13**5.)
    x(i,3)=-1.*(g10+g11)/.01
    x(i,4)=x(i,3)
else
    x(i,2)=-15.50
    x(i,3)=-20.25
    x(i,4)=x(i,3)
endif
g8=.165+.155*y11-.025*(y11**2)-.311936*(y11**3)+.826826*(y11**4)
g9=-.9010034*(y11**5.)+.3592734*(y11**6.)-.01816*(y11**7.)
z(i,2)=(g8+g9)/.01
g12=.05325+.085*y11-.075*(y11**2)+.1473*(y11**3)-.33543*(y11**4)
g13=.5778333*(y11**5.)-.5472592*(y11**6.)+.1940741*(y11**7.)
z(i,3)=(g12+g13)/.01
if (y(i) .ge.175. .and. y(i) .le. 200.) then
    g14=-.066-.0377*y11+6.3274794*(y11**3)-54.34748*(y11**4)
    g15=183.0187488*(y11**5.)-221.217856*(y11**6.)
    z(i,4)=(g14+g15)/.01
    g16=.141+.016*y11-.04*(y11**2)
1      -.6661333*(y11**3)+5.7792*(y11**6)
    g17=-17.80224*(y11**5.)+19.6949333*(y11**6.)
    x(i,5)=-1.*(g16+g17)/.01
else
    z(i,4)=-12.4874+.0303714*y(i)
    x(i,5)=-14.209
endif
z(i,5)=z(i,6)+3.45
y(i+1)=y(i)+dely
700 continue
do 100 i=1,22

```

```

am=x(i,3)
an=z(i,3)
au=x(i,1)
av=z(i,1)
ag=x(i,6)
ah=z(i,6)
aa=au-am
ab=av-an
ac=ag-am
ad=ah-an
c   using a parabola for sections before y(i)<50.0
pup=-1.0*(ab/aa)
sup=(4.0*(ab**2.))/aa
pdown=-1.0*(ad/ac)
sdown=(4.0*(ad**2.))/ac
do 105 j=1,jdiminit
c   x1(i,j)=aa*cos(((j-1)*pi)/(2.0*(jdiminit-1)))
x1(i,j)=aa-aa*sin(((j-1)*pi)/(2.0*(jdiminit-1)))
if (i .eq. 1) then
    z1(i,j)=0.0
    go to 105
endif
z1(i,j)=pup*x1(i,j)+((abs(sup*x1(i,j)))**0.5)
105 continue
do 110 j=jdiminit,j2init
jjj=2*jdiminit-j
x1(i,j)=x1(i,jjj)
if (i .eq. 1) then
    z1(i,j)=0.0
    go to 110
endif
z1(i,j)=pdown*x1(i,j)-((abs(sdown*x1(i,j)))**0.5)
110 continue
do 115 j=1,j2
x2(i,j)=x1(i,j)+am
z2(i,j)=z1(i,j)+an
115 continue
do 102 j=1,j2init
write(13,103) i,j,x1(i,j),z1(i,j),-x2(i,j),z2(i,j)

```

```

103  format (1x,2(i3,2x),1x,4(f14.4,1x))
102  continue
100  continue
    do 200 i=23,44
    if (i .ge. 33)then
        jdim=21
        j2=(2*jdim)-1
        jdimfinal=jdim
        j2final=j2
    endif
    if ((i .ge.23) .and. (i .le. 32)) then
        jdim=22
        j2=(2*jdim)-1
        jdiminter=jdim
        j2inter=j2
    endif
    aml=x(i,3)
    anl=z(i,3)
    am2=x(i,4)
    an2=z(i,4)
    au1=x(i,1)
    av1=z(i,1)
    au2=x(i,2)
    av2=z(i,2)
    ag1=x(i,6)
    ah1=z(i,6)
    ag2=x(i,5)
    ah2=z(i,5)
    au3=au1-aml
    av3=av1-anl
    au4=au2-aml
    av4=av2-anl
    ak=((av4-(av3*au4/au3))**2.)/(au4*(av3-av4))
    as=ak*av3
    ar=ak*(.25*ak-(av3/au3))
    ap=-0.25*ak-(.25*ak-(av3/au3))
    do 205 j=1,jdim-1
    x1(i,j)=au3-au3*sin(((j-1)*pi)/(2.0*(jdim-2)))
    z1(i,j)=ap*x1(i,j)+((abs(ar*(x1(i,j)**2.))+as*x1(i,j)))**0.5)
205  continue

```

```

do 210 j=1,jdim-1
x2(i,j)=x1(i,j)+am1
z2(i,j)=z1(i,j)+an1
210 continue
ag3=ag1-am2
ah3=ah1-an2
ag4=ag2-am2
ah4=ah2-an2
ak=((ah4-(ah3*ag4/ag3))**2.)/(ag4*(ah3-ah4))
as=ah3*ak
ar=ak*(0.25*ak-(ah3/ag3))
ap=-.25*ak-(.25*ak-(ah3/ag3))
do 220 j=jdim+1,j2
jjj=2*jdim-j
x1(i,j)=x1(i,jjj)
z1(i,j)=ap*x1(i,j)-((abs(ar*(x1(i,j)**2.)+as*x1(i,j)))**0.5)
220 continue
do 230 j=jdim+1,j2
x2(i,j)=x1(i,j)+am2
z2(i,j)=z1(i,j)+an2
230 continue
x2(i,jdim)=x2(i,jdim+1)
z2(i,jdim)=(z2(i,jdim+1)+z2(i,jdim-1))/2.
do 202 j=1,j2
201 format(1x,2(i3,2x),1x,4(f14.4,1x))
202 continue
s(1)=0.0
do 990 j=1,j2
if (i .eq. 24) then
    if (j .lt. j2) then
        dels=((x2(i,j+1)-x2(i,j))**2+(z2(i,j+1)-z2(i,j))**2)**.5
        s(j+1)=s(j)+dels
    endif
    if (j .eq. j2) then

```

c
c
c

```

generates slopes and curvatures at any particular cross section

h1=x2(i,j-1)-x2(i,j)
h3=x2(i,j-2)-x2(i,j)

```

```

        down2=h1*h3*(h1-h3)
        up2=(h3**2)*z2(i,j-1)-(h1**2)*z2(i,j-2)-((h3**2)-
1          h1**2)*z2(i,j)
        slopel(i,j)=up2/down2
        denom2=h1*h3*(h1-h3)/2
        anumer2=h3*z2(i,j-1)-h1*z2(i,j-2)-(h3-h1)*z2(i,j)
        curv(i,j)=(anumer2/denom2)/((1+slopel(i,j)**2)**1.5)
        endif
        if (j .eq. 1) then
        h1=x2(i,j)-x2(i,j+1)
        h3=x2(i,j)-x2(i,j+2)
        down1=h1*h3*(h3-h1)
        up1=(h3**2)*z2(i,j+1)-(h1**2)*z2(i,j+2)-((h3**2)-
1          h1**2)*z2(i,j)
        slopel(i,j)=up1/down1
        denom1=h1*h3*(h1-h3)/2
        anumer1=h3*z2(i,j+1)-h1*z2(i,j+2)-(h3-h1)*z2(i,j)
        curv(i,j)=(anumer1/denom1)/((1+slopel(i,j)**2)**1.5)
        endif
        if ((j .ge. 2) .and. (j .lt. j2)) then
        h2=x2(i,j)-x2(i,j+1)
        h1=x2(1,j-1)-x2(i,j)
        slopel(i,j)=(z2(i,j+1)-z2(i,j-1))/(x2(i,j-1)-x2(i,j+1))
        denom=(h1*(h2**2)+(h2*(h1**2)))/2
        anumer=(h1*z2(i,j+1)+(h2*z2(i,j-1))-((h1+h2)*z2(i,j)))
        curv(i,j)=(anumer/denom)/((1+slopel(i,j)**2)**1.5)
        write(13,*)h1,h2,-x2(i,j),z2(i,j),slopel(i,j),curv(i,j)
        endif
    endif
107   format(2(f14.9,1x))
990   continue
    if (i .eq. 24) then
        do 444 j=1,j2
            ratio=s(j)/s(j2)
            write(14,107)ratio,slopel(i,j)
            write(15,107)ratio,curv(i,j)
444   continue
    endif
200   continue
    do 250 j=1,j2init

```

```

z2(1,j)=-8.589
250 continue
do 260 i=1,32
if (i .le. 22) then
    jdim=jdiminit
    j2=j2init
else
    jdim=jdiminter
    j2=j2inter
endif
do 255 j=1,j2
if (j .lt. (jdim-1)) then
    jj=j
    xx2(i,jj)=x2(i,j)
    zz2(i,jj)=z2(i,j)
endif
if (j .eq. (jdim-1)) go to 255
if (j .eq. jdim) then
    jj=jdim-1
    xx2(i,jj)=x2(i,j)
    zz2(i,jj)=z2(i,j)
endif
if (j .eq. (jdim+1)) go to 255
if (j .gt. (jdim+1)) then
    jj=j-2
    xx2(i,jj)=x2(i,j)
    zz2(i,jj)=z2(i,j)
endif
255 continue
260 continue
do 263 i=23,32
do 264 j=1,j2init
x2(i,j)=xx2(i,j)
z2(i,j)=zz2(i,j)
264 continue
263 continue
do 721 i=23,44
jextra=3
topdels=(z2(i,jdimfinal)-z2(i,jdimfinal-1))/(jextra+1)

```

```

topdelr=(x2(i,jdimfinal)-x2(i,jdimfinal-1))/(jextra+1)
botdelr=(x2(i,jdimfinal+1)-x2(i,jdimfinal))/(jextra+1)
botdels=(z2(i,jdimfinal+1)-z2(i,jdimfinal))/(jextra+1)
do 723 j=1,j2final
if (j .le. (jdimfinal-1)) then
    jj=j
    xx2(i,jj)=x2(i,j)
    zz2(i,jj)=z2(i,j)
endif
if (j .eq. jdimfinal) then
    jj=jdimfinal+jextra
    xx2(i,jj)=x2(i,j)
    zz2(i,jj)=z2(i,j)
endif
if (j .ge. (jdimfinal+1)) then
    jj=j+(2*jextra)
    xx2(i,jj)=x2(i,j)
    zz2(i,jj)=z2(i,j)
endif
723 continue
do 726 jibba=1,jextra
jj=jdimfinal-1+jibba
xx2(i,jj)=x2(i,jdimfinal-1)+(jibba*topdelr)
zz2(i,jj)=z2(i,jdimfinal-1)+(jibba*topdels)
726 continue
do 728 jibba1=1,jextra
jj=jdimfinal+jextra+jibba1
xx2(i,jj)=x2(i,jdimfinal)+(jibba1*botdelr)
zz2(i,jj)=z2(i,jdimfinal)+(jibba1*botdels)
728 continue
721 continue
do 300 i=1,44
ylangley=(y(i)-42.5)*.17
do 300 j=1,j2init-2
yyy(i,j,1)=(y(i)-42.5)*.17
300 continue
do 500 i=1,44
do 400 j=1,j2init-2
xxx(i,j,1)=-xx2(i,j)*.17

```

```

      zzz(i,j,1)=zz2(i,j)*.17
400  continue
500  continue
      do 7000 ii=1,iext
      yext(ii)=yahead*sin(((ii-1)*pi)/(2*(iext-1)))
      if (ii .eq. iext .or. ii .eq. (iext-1)) go to 7000
      do 7100 j=1,j2init-2
      ass1=0.0
      ass2=0.0
      ass3=yext(ii)*.17
      write(12,530)ass1,ass2,ass3
      if ((j .eq. 1).or. (j .eq.(j2init-2))) then
      write(16,530)ass1,ass2,ass3
      endif
7100 continue
7000 continue
c
c   writes input to grid generator ( GRIDTOOL )
c
      do 510 i=1,22
      if ((i .eq. 1) .or. (i .eq. 22) .or. (i .eq. 18)) then
      if (i .eq. 18) then
      dely=y(i)-y(1)
      endif
      if (i .eq. 22)then
      dely=y(i)-y(18)
      endif
      do 520 j=1,j2init-2
      ass1=-xx2(i,j)*.17
      ass2=(zz2(i,j)-zz2(1,j))* .17
      ass3=(y(i)-42.5+100)*.17
      write(12,530)ass1,ass2,ass3
      if ((j .eq. 1) .or. (j .eq.(j2init-2)))
1 write(16,530)ass1,ass2,ass3
c   if (i .eq. 18) then
c   write(8,*)ass1,ass2
c   endif
530  format(3f15.8)
520  continue
      endif

```

```

510   continue
      do 550 i=23,44
      dely=y(i)-y(i-1)
c     write(6,*)dely
      do 560 j=1,j2init-2
      ass1=-xx2(i,j)*.17
      ass2=(zz2(i,j)-zz2(1,j))* .17
      ass3=(y(i)-42.5+100)*.17
      write(12,570)ass1,ass2,ass3
      if ((j .eq. 1) .or.(j .eq.(j2init-2)))
      write(16,570)ass1,ass2,ass3
      endif
570   format(3f15.8)
560   continue
550   continue
      go to 1000
      idim1=44
      jdim1=j2init-2
      kdim1=1
c
c     write output in PLOT3D format
c
      write(10,*)idim1,jdim1,kdim1
      write(10,*)((xxx(i,j,k),i=1,idim1),j=1,jdim1),k=1,kdim1)
      write(10,*)((yyy(i,j,k),i=1,idim1),j=1,jdim1),k=1,kdim1)
      write(10,*)((zzz(i,j,k),i=1,idim1),j=1,jdim1),k=1,kdim1)
1000  continue
      stop
      end

```

APPENDIX C
ERICKSON FOREBODY MATH MODEL

The Erickson forebody math model was developed using the descriptions of the model contained in the Langley reports, a CAD drawing of the forebody and digitized data of the drawing generated by Nielsen Engineering Company.

```
c Program efbmm.f (Erickson forebody math model)
c Erickson/Hall chine forebody surface geometry definition
c
c W.H. Mason, December 1989
c
c the main program is an example driver for the five subroutines
c
c longitudinal lines routines:
c
c xstn is input: ymhb, zupcl, and zlowcl are output
c
c subroutine ymhbc(xstn,ymhb) - find the y max half breadth line
c subroutine topcl(xstn,zupcl) - find the top center line
c subroutine botcl(xstn,zlowcl) - find the bottom center line
c
c cross section lines routines:
c
c xstn, zupcl, zlowcl, ymhb and xs are input: zu and zl are output
c
c subroutine top(xstn,zupcl,ymhb,xs,zu)
c subroutine bot(zlowcl,ymhb,xs,zl)
c
c input/output is dimensional except xs, which is the % spanwise location
c xs must be positive, use symmetry to get lines for -xs
c the routines use spline subroutines from Conte and Deboor (included)
c
dimension xpt(10,221),zpt(10,221),xstref(20)
c
imax = 9
xstref(1) = 0.0
xstref(2) = 1.44
xstref(3) = 4.312
xstref(4) = 7.19
xstref(5) = 10.12
xstref(6) = 13.56
xstref(7) = 17.25
xstref(8) = 19.94
```

```

xstref(9)    = 30.00

do 10  istn = 1,imax
xstn        = xstref(istn)
call ymhbc(xstn,ymhb)
call topcl(xstn,zupcl)
call botcl(xstn,zlowcl)

write(6,80) istn,xstn,ymhb,zupcl,zlowcl

do 10  i    = 1,101
ii     = 201 - (i-1)
xs     = 0.01*float(i-1)
call top(xstn,zupcl,ymhb,xs,zu)
call bot(zlowcl,ymhb,xs,zl)
xpt(istn,i) = xs*ymhb
zpt(istn,i) = zu
xpt(istn,ii) = xs*ymhb
zpt(istn,ii) = zl
10 continue

do 20 i = 1,201
write(6,100) (xpt(j,i),zpt(j,i), j = 1,imax)
20 continue

80 format(2x,i4,f10.5,3f15.5)
100 format(18f14.6)
stop
end

```

```

subroutine top(xstn,topcl,ymhb,xs,zu)

```

```

c
c
c
c
c
c

```

```

W.H. Mason, December, 1989

```

```

upper surface chine cross-section based on Bob Hall's routine

```

```

xs is % semi-span, and zu is dimensional

```

```

c topcl - top centerline of body
c ymhb  - max-half breadth of configuration
c
c xs    - spanwise location where z value is desired
c zu    - output value of body elevation at input xs

```

```

dimension xi(11),c(4,11)

```

```

c define cross section for xstn up to 7.19

```

```

pi      = 3.1415926

```

```

zu      = 0.0

```

```

if(xstn .le. 0.0) return

theta      = 12.0*pi/180.0

cc         = topcl/ymhb
tanht     = tan(theta)
a4         = 2.*tanht - 3.*cc
a3         = 5.*tanht - 8.*cc
a2         = 3.*tanht - 6.*cc

c
zu1        = (a4*xs**4 - a3*xs**3 + a2*xs**2 + cc) * ymhb
c
c
define cross section for xstn = 19.94 and beyond
c
if(xs .le. 0.40) then

                zu2 = sqrt(1.0-2.6*xs**2)*topcl
                go to 10

                end if

nin          = 4

xi(1)       = .4
xi(2)       = 0.62594
xi(3)       = 0.90121
xi(4)       = 1.0

c(1,1)      = 0.764199
c(1,2)      = 0.34556
c(1,3)      = 0.022085
c(1,4)      = 0.0

c(2,1)      = -1.3609
c(2,nin)    = -0.175

n           = nin - 1
call spline(n,xi,c)
call calccf(n,xi,c)

zu2         = pcubic(xs,n,xi,c)*topcl

10 continue

if(xstn .le. 7.19) zu = zu1
if(xstn .ge. 19.94) zu = zu2

if(xstn .gt. 7.19 .and. xstn .lt. 19.94) then

        xn = (xstn - 7.19)/(19.94 - 7.19)
        cn = f(xn)
        zu = (1. - cn)*zu1 + cn*zu2

```

```

        end if

    return
end

function f(xn)
c   blending function
    y   = 5.0*xn**2 - 6.0*xn**3
    if(xn .gt. 0.5) y = 1.-(5.0*(1.-xn)**2-6.*(1.-xn)**3)
    f = y
    return
end

subroutine bot(botcl,ymhb,xs,zl)
c
c   W. H. Mason, December, 1989
c
c   lower surface chine cross-section based on Bob Hall's routine
c
c   xs is % semi-span, and zl is dimensional
c
c   botcl - bottom centerline of body
c   ymhb  - max-half breadth of configuration at this station
c
c   xs    - spanwise location where y value is desired
c   zl    - output value of body elevation at input xs

    dimension xi(60),c(4,60)

    pi      = 3.1415926

    zl      = 0.0
    if(ymhb .eq. 0.0) return

    thetal  = -2.0*pi/180.0

    b       = botcl/ymhb
    tantht  = tan(thetal)
    a4      = 3.0*b - 2.*tantht
    a3      = 8.0*b - 5.*tantht
    a2      = 6.0*b - 3.*tantht
c
    zlbase  = (a4*xs**4 - a3*xs**3 + a2*xs**2 - b) * ymhb

    zmod    = 0.0

    nin     = 13
    xi(1)   = 0.000

```

```
xi(2) = 0.020
xi(3) = 0.120
xi(4) = 0.230
xi(5) = 0.340
xi(6) = 0.450
xi(7) = 0.540
xi(8) = 0.590
xi(9) = 0.630
xi(10) = 0.740
xi(11) = 0.850
xi(12) = 0.940
xi(13) = 1.000
```

```
c(1,1) = 0.000000
c(1,2) = 0.002180
c(1,3) = 0.050257
c(1,4) = 0.152545
c(1,5) = 0.249569
c(1,6) = 0.300617
c(1,7) = 0.270427
c(1,8) = 0.202228
c(1,9) = 0.135704
c(1,10) = 0.050513
c(1,11) = 0.017489
c(1,12) = 0.003740
c(1,13) = 0.000000
```

```
c(2,1) = 0.0
c(2,nin) = 0.0
```

```
n = nin-1
call spline(n,xi,c)
call calccf(n,xi,c)
```

```
bot719 = -1.6359
```

```
c the 1.76794 factor is the ymhb at x = 7.19
```

```
zmod = pcubic(xs,n,xi,c)*(botc1/bot719)*1.76794
```

```
zl = -(zlbase + zmod)
```

```
return
end
```

```
subroutine ymhb(xstn,ymhb)
```

```
c
c y max half breadth definition for the Erickson chine forebody
c
c xstn is input, ymhb is the output
```

c W.H. Mason, final version May 16, 1990

```
dimension xi(20),c(4,20)
```

```
if(xstn .le. 0.0) ymhb = 0.0
```

c tangent ogive portion

```
if(xstn .gt. 0.0 .and. xstn .le. 8.0) then
```

```
    r0      = 4.35
    xlref   = 27.35
    r0xl    = r0/xlref
    deltana = 27.5

    deltan  = deltana*3.1415926/180.0
    xnr0    = sin(deltan)/(1.0 - cos(deltan))
    xnxl    = xnr0*r0xl

    a       = r0xl*cos(deltan)/(1.0 - cos(deltan))
    b       = 2.*r0xl*sin(deltan)/(1.0 - cos(deltan))

    xn      = xnxl*xlref

    x       = xstn
    xl      = x/xlref
    rxl     = sqrt(a**2 + b*xl - xl**2) - a

    ymhb    = rxl * xlref

end if
```

c first spline p[ortion

```
if(xstn .gt. 8.0 .and. xstn .lt. 19.0) then
```

```
    nin     = 3
    xi(1)   = 8.0
    xi(2)   = 11.00
    xi(3)   = 19.00

    c(1,1)  = 3.08787
    c(1,2)  = 3.717
    c(1,3)  = 4.35

    c(2,1)  = 0.26256
    c(2,nin) = 0.0

    n       = nin - 1
    call spline(n,xi,c)
    call calccf(n,xi,c)
```

```

        ymhb      = pcubic(xstn,n,xi,c)
    end if

c    straight line portion
    if(xstn .gt. 19.0) ymhb = 4.35

    return
end

subroutine topcl(xstn,zupcl)
c
c    top centerline definition for the Erickson chine forebody
c
c    xstn is input, zupcl is output
c
c    W.H. Mason, final version May 165, 1990

    dimension xi(20),c(4,20)

    if(xstn .le. 0.0)    zupcl = 0.0

c    tangent ogive portion

    if(xstn .gt. 0.0 .and. xstn .le. 7.5) then

        r0      = 2.616
        xlref   = 23.000
        r0xl    = r0/xlref
        deltana = 19.500

        deltan  = deltana*3.1415926/180.0
        xnr0    = sin(deltan)/(1.0 - cos(deltan))
        xnxl    = xnr0*r0xl

        a      = r0xl*cos(deltan)/(1.0 - cos(deltan))
        b      = 2.*r0xl*sin(deltan)/(1.0 - cos(deltan))

        xn     = xnxl*xlref

        x      = xstn
        xl     = x/xlref
        rxl    = sqrt(a**2 + b*xl - xl**2) - a

        zupcl  = rxl * xlref

    end if

c    first spline p[ortion

```

```
if(xstn .gt. 7.5 .and. xstn .lt. 14.94) then
```

```
    nin      = 3
```

```
    xi(1)    = 7.5
```

```
    xi(2)    = 10.12
```

```
    xi(3)    = 14.94
```

```
    c(1,1)   = 1.9571
```

```
    c(1,2)   = 2.35
```

```
    c(1,3)   = 2.58
```

```
    c(2,1)   = .17184
```

```
    c(2,nin) = 0.0064935
```

```
    n        = nin - 1
```

```
    call spline(n,xi,c)
```

```
    call calccf(n,xi,c)
```

```
    zupcl    = pcubic(xstn,n,xi,c)
```

```
end if
```

```
c    first straight line portion
```

```
if(xstn .ge. 14.94 .and. xstn .le. 17.25) then
```

```
    xref     = 14.94
```

```
    zref     = 2.58
```

```
    dzref    = 0.0064935
```

```
    zupcl    = zref + (xstn - xref)*dzref
```

```
end if
```

```
c    second spline section
```

```
if(xstn .gt. 17.25 .and. xstn .lt. 19.94) then
```

```
    nin      = 2
```

```
    xi(1)    = 17.25
```

```
    xi(2)    = 19.94
```

```
    c(1,1)   = 2.595
```

```
    c(1,2)   = 2.630
```

```
    c(2,1)   = 0.0064935
```

```
    c(2,nin) = 0.0294118
```

```
    n        = nin - 1
```

```

        call spline(n,xi,c)
        call calccf(n,xi,c)

        zupcl    = pcubic(xstn,n,xi,c)

    end if

c    second straight section

    if(xstn .ge. 19.94 .and. xstn .le. 23.0) then

        xref    = 19.94
        zref    = 2.63
        dzref   = 0.0294118

        zupcl   = zref + (xstn - xref)*dzref

    end if

c    third and final spline section

    if(xstn .gt. 23.0 .and. xstn .le. 30.0) then

        nin     =      2

        xi(1)   = 23.0
        xi(2)   = 30.0

        c(1,1)  = 2.72
        c(1,2)  = 2.75

        c(2,1)  = 0.0294118
        c(2,nin) = 0.0

        n       = nin - 1
        call spline(n,xi,c)
        call calccf(n,xi,c)

        zupcl   = pcubic(xstn,n,xi,c)

    end if

    if(xstn .gt. 30.0) zupcl = 2.75

    return
end

subroutine botcl(xstn,zlowcl)
c
c    bottom centerline definition for the Erickson chine forebody
c

```

```

c   xstn is input, zlowcl is output
c
c   W.H. Mason, final version May 16, 1990

dimension xi(20),c(4,20)

if(xstn .le. 0.0)   zlowcl = 0.0

c   tangent ogive portion

if(xstn .gt. 0.0 .and. xstn .le. 6.0) then

    r0          = 3.50
    xlref       = 27.35
    r0xl        = r0/xlref
    deltana     = 15.0

    deltan      = deltana*3.1415926/180.0
    xnr0        = sin(deltan)/(1.0 - cos(deltan))
    xnxl        = xnr0*r0xl

    a           = r0xl*cos(deltan)/(1.0 - cos(deltan))
    b           = 2.*r0xl*sin(deltan)/(1.0 - cos(deltan))

    xn          = xnxl*xlref

    x           = xstn
    xl          = x/xlref
    rxl         = sqrt(a**2 + b*xl - xl**2) - a

    zlowcl     = -rxl * xlref

end if

c   first spline p[ortion

if(xstn .gt. 6.0 .and. xstn .lt. 19.94) then

    nin        = 3
    xi(1)      = 6.0
    xi(2)      = 10.12
    xi(3)      = 19.94

    c(1,1)     = -1.41617
    c(1,2)     = -2.025
    c(1,3)     = -2.59

    c(2,1)     = -0.20456
    c(2,nin)   = -0.052288

    n          = nin - 1
    call spline(n,xi,c)

```

```

        call calccf(n,xi,c)

        zlowcl  = pcubic(xstn,n,xi,c)

        end if

c      first straight line portion

if(xstn .ge. 19.94 .and. xstn .le. 23.0) then

        xref    = 19.94
        zref    = -2.59
        dzref   = -0.052288

        zlowcl  = zref + (xstn - xref)*dzref

        end if

c      second spline section

if(xstn .gt. 23.0 .and. xstn .lt. 30.0) then

        nin     = 2

        xi(1)   = 23.0
        xi(2)   = 30.0

        c(1,1)  = -2.75
        c(1,2)  = -2.85

        c(2,1)  = -0.052288
        c(2,nin) = 0.0

        n       = nin - 1
        call spline(n,xi,c)
        call calccf(n,xi,c)

        zlowcl  = pcubic(xstn,n,xi,c)

        end if

c      second straight section

if(xstn .ge. 30.0) then

        zlowcl  = -2.85

        end if

return
end

```

```

SUBROUTINE SPLINE(N,XI,C)
C
C FROM CONTE AND DEBOOR
C
DIMENSION XI(201),C(4,201),D(201),DIAG(3201)
DATA DIAG(1),D(1)/1.0D0,0.0D0/
NP1=N+1
DO 10 M=2,NP1
D(M)=XI(M)-XI(M-1)
10 DIAG(M)=(C(1,M)-C(1,M-1))/D(M)
DO 20 M=2,N
C(2,M)=3.0D0*(D(M)*DIAG(M+1)+D(M+1)*DIAG(M))
20 DIAG(M)=2.0D0*(D(M)+D(M+1))
DO 30 M=2,N
G=-D(M+1)/DIAG(M-1)
DIAG(M)=DIAG(M)+G*D(M-1)
30 C(2,M)=C(2,M)+G*C(2,M-1)
NJ=NP1
DO 40 M=2,N
NJ=NJ-1
40 C(2,NJ)=(C(2,NJ)-D(NJ)*C(2,NJ+1))/DIAG(NJ)
RETURN
END

```

```

SUBROUTINE CALCCF(N,XI,C)
DIMENSION XI(201),C(4,201)
DO 10 I=1,N
DX=XI(I+1)-XI(I)
DIVDF1=(C(1,I+1)-C(1,I))/DX
DIVDF3=C(2,I)+C(2,I+1)-2.0D0*DIVDF1
C(3,I)=(DIVDF1-C(2,I)-DIVDF3)/DX
10 C(4,I)=DIVDF3/DX/DX
RETURN
END

```

```

FUNCTION PCUBIC(XBAR,N,XI,C)
DIMENSION XI(201),C(4,201)
I = 1
DX=XBAR-XI(I)
IF (DX) 10,30,20
10 IF (I.EQ.1) GO TO 30
I=I-1
DX=XBAR-XI(I)
IF (DX) 10,30,30
19 I=I+1
DX=DDX
20 IF (I.EQ.N) GO TO 30
DDX=XBAR-XI(I+1)
IF (DDX) 30,19,19
30 PCUBIC=C(1,I)+DX*(C(2,I)+DX*(C(3,I)+DX*C(4,I)))
RETURN
END

```

REFERENCES

1. Chambers, J.R., "High-Angle-of-Attack Aerodynamics: Lessons Learned," AIAA paper No. 86-1774, June 1986.
2. Chambers, J.R. and Grafton, S.B., "Aerodynamic Characteristics of Airplanes at High Angle of Attack," NASA TM 74097, Dec. 1977.
3. Nguyen, L.T., "Control System Techniques for Improved Departure/Spin Resistance for Fighter Aircraft," SAE Paper 791083, Dec. 1979.
4. Rao, D.M., and Murri, D.G., "Exploratory Investigation of Deflectable Forebody Strakes for High Angle-of-Attack Yaw Control," AIAA Paper No. 86-0333, Jan. 1986.
5. Grafton, S.B., Chambers, J.R., and Coe, P.L., Jr., "Wind-Tunnel Free-Flight Investigation of a Model of a Spin Resistant Fighter Configuration," NASA TN D-7716, June 1974.
6. Lapins, M., Martorella, R.P., Klein, R.W., Meyer, R.C., and Sturm, M.J., "Control Definition Study for Advanced Vehicles," NASA CR 3738, Nov. 1983.
7. Erickson, G.E., and Brandon, J.M., "Low-Speed Experimental Study of the Vortex Flow Effects of a Fighter Forebody Having Unconventional Cross-Section," AIAA Paper No. 85-1798.
8. NASA/Grumman Co-operative Program.
9. Novak, C.J., Huie, C.R., Cornelius, K.C., "Laser Velocimetry in Highly Three Dimensional and Vortical Flows," NASA CP 2416, Vol 1, pp. 163-185.
10. Edwards, O.R., "Northrop F-5F Shark Nose Development," NASA CR 158936, Oct. 1979.
11. Ghaffari, F., Luckring, J.M. Thomas, J.L., and Bates, B.L., "Navier-Stokes Solutions about F/A-18 Forebody - LEX Configuration," AIAA paper No. 89-0338, Jan. 1989.
12. Hartwich, P., and Hall, R. "Navier-Stokes Solutions for Vortical Flows Over a Tangent-Ogive Cylinder," AIAA Paper No. 89-0337, Jan. 1989.
13. Hartwich, P.M., Hall, R.M., and Hensch, M.J., "Navier-Stokes Computations of Vortex Asymmetries Controlled by Small Surface Imperfections," AIAA Paper No. 90-0385, Jan. 1990.
14. Schiff, L.B., Degani, D., and Cummings, R.M., "Numerical Simulation of Separated and Vortical Flows on bodies at Large Angles of Attack," Fourth Symposium on Numerical and Physical Aspects of Aerodynamic Flows, 1989.
15. Thomas, J.L., van Leer, B., and Walters, R.W., "Implicit Flux-Split Schemes for the Euler Equations," AIAA Paper 85-1680, July 1985.
16. Baldwin, B.S., and Lomax, H., "Thin Layer Approximation and Algebraic Model for Separated Turbulent Flows," AIAA Paper 78-257, 1978.

17. Degani, D., and Schiff, L.B., "Computation of Supersonic Viscous Flows Around Pointed Bodies at Large Incidence," AIAA Paper No. 83-0034.
18. Degani, D., and Schiff, L.B., "Computation of Turbulent Supersonic Flows Around Pointed Bodies Having Cross Flow Separation," *Journal of Computational Physics*, 66, pp. 173-196, 1986.
19. Degani, D., and Schiff, L.B., and Yural Levy., "Physical Considerations Governing Computation of Turbulent Flows Over Bodies at Large Incidence," AIAA Paper No. 90-0096.
20. McCrory, W. personal communication, 1989.
21. Walters, R.W., Reu, T., Thomas, J.L., and McCrory, W.D., "Zonal Techniques for Flowfield Simulation about Aircraft," *Computers & Structures*, Vol. 30, No. 1/2, pp. 47-54, 1988.
22. Walatka, P.P., Buning, P.G., Pierce, L., and Elson, A. "PLOT3D User's Manual," NASA TM 101067, Mar 1990.
23. Lamont, P.J., "The Complex Asymmetric Flow Over a 3.5D Ogive Nose and Cylindrical Afterbody at High Angles of Attack," AIAA Paper No. 82-0053, Jan. 1982.
24. Liming, R.A., *Mathematics for Computer Graphics*, 1979.
25. Barger, R.L., and Adams, M.S., "Semianalytic Modeling of Aerodynamic Shapes," NASA TP 2413, April, 1985.
26. Lamar, J.E., and Herbert, H.E., "Production Version of the Extended NASA-Langley Vortex Lattice FORTRAN Computer Program - Volume I - User's Guide," NASA TM 83303, April 1982.

Virginia Polytechnic Institute and State University

Blacksburg, Virginia 24061

October 10, 1990

(rev., January 31, 1992)

TANGENT OGIVE 31 x 69 x 24 grid

	$\alpha = 20^\circ, \beta = 0^\circ$	$\alpha = 0^\circ, \beta = 20^\circ$
	-----	-----
C_x	-0.02004	-0.02004
C_y	0.2737E-3	0.1842
C_z	0.1845	-0.3878E-4
C_m	-1.595	0.2988E-3
C_n	-0.4143E-2	1.593
Iterations	1950	2260

Table 1. Comparison of Forces and Moments showing equivalence between angle-of-attack with no sideslip and sideslip with no angle-of-attack for an axisymmetric body

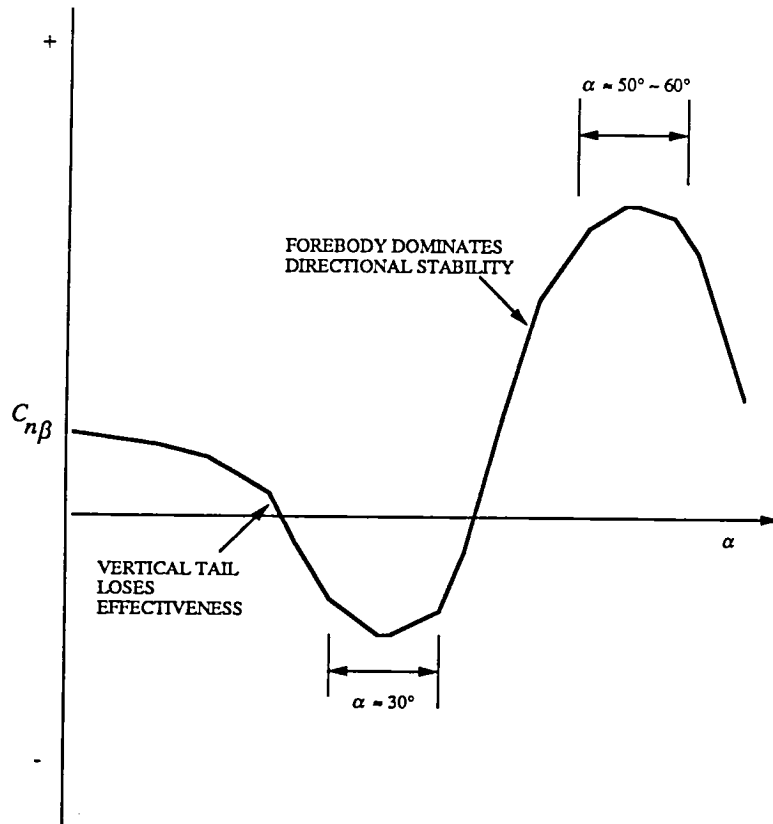


Figure 1. Typical $C_{n\beta}$ characteristics of an advanced fighter

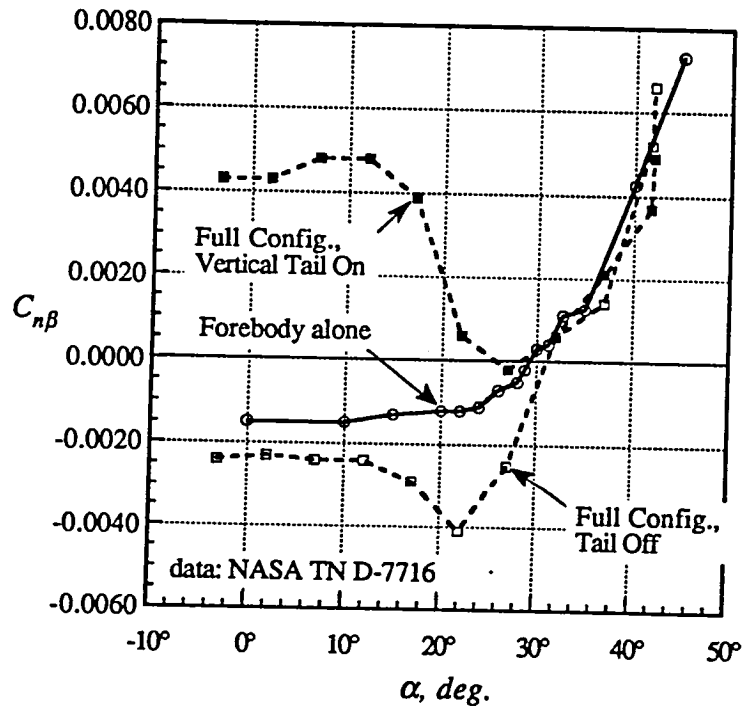


Figure 2. Grafton's classic example (ref. 5)

FOREBODY CROSS-SECTIONS

TYPICAL HI - α FOREBODY FLOW

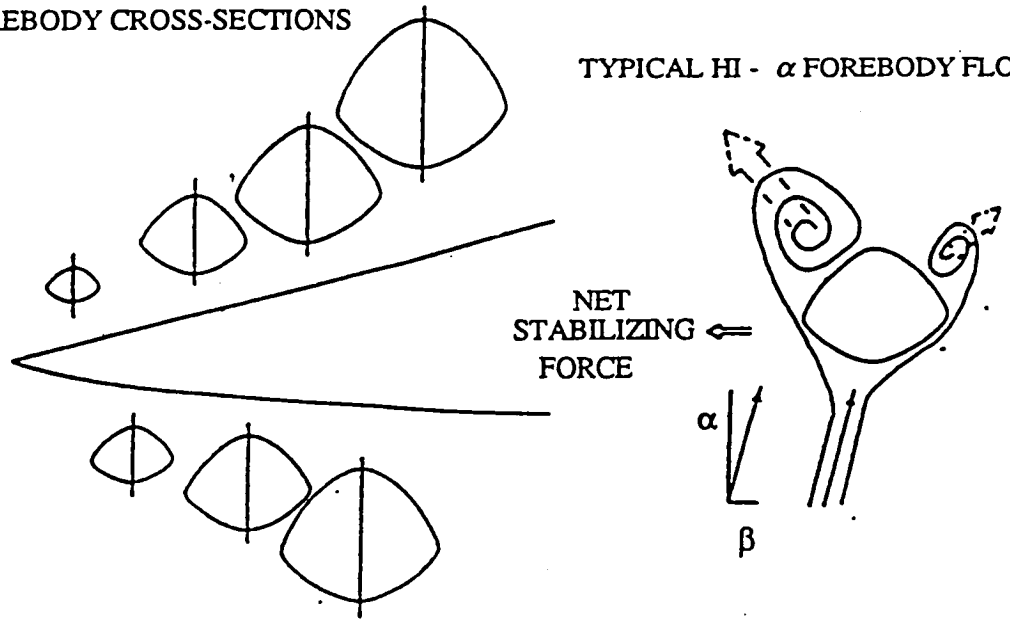


Figure 3. Schematic of a typical forebody flowfield characteristics

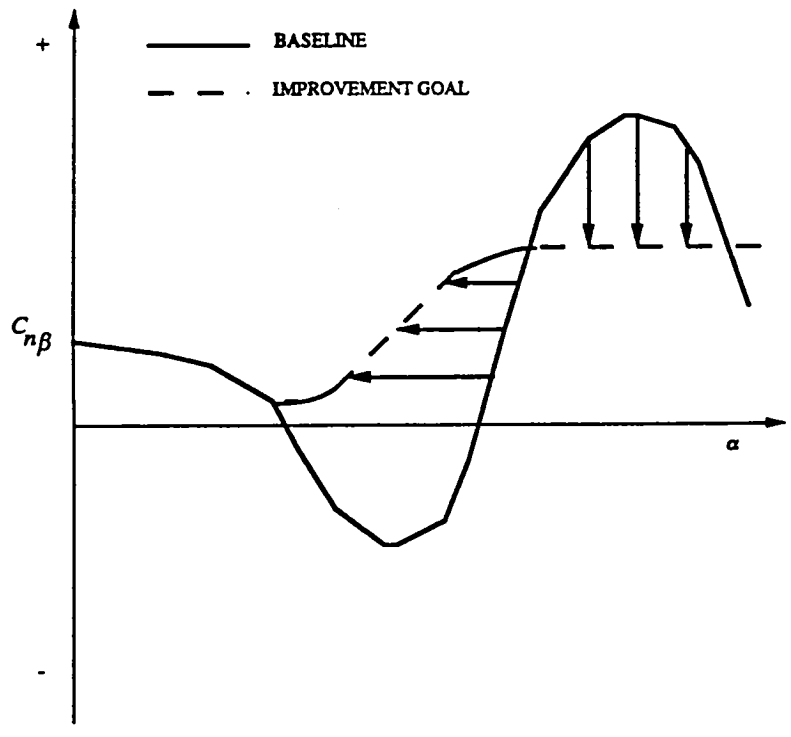
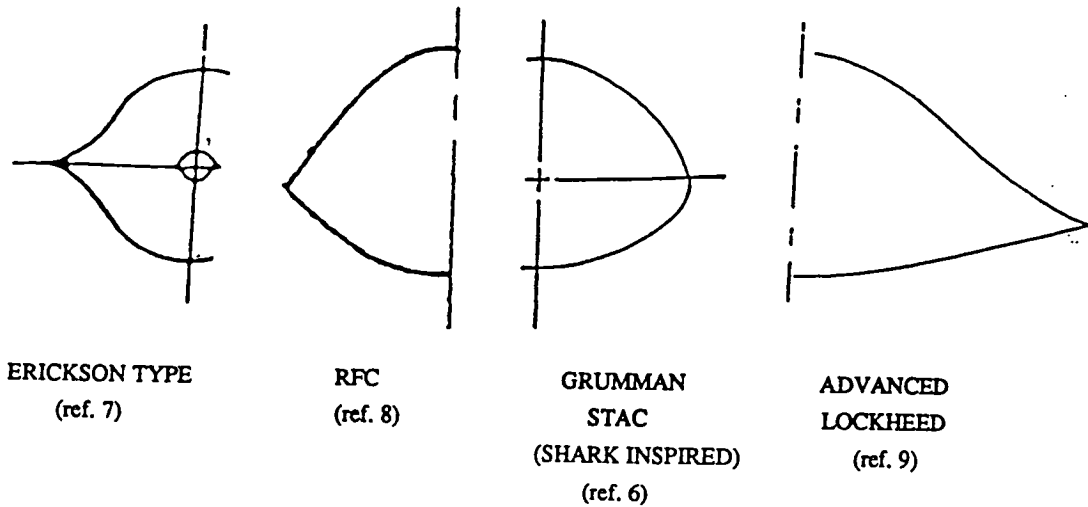
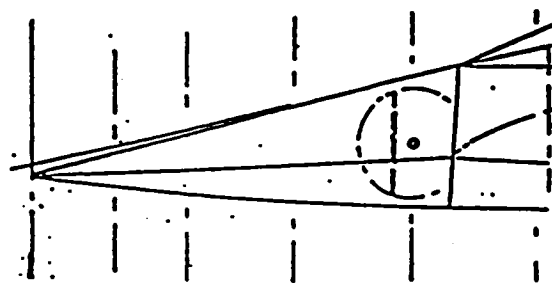
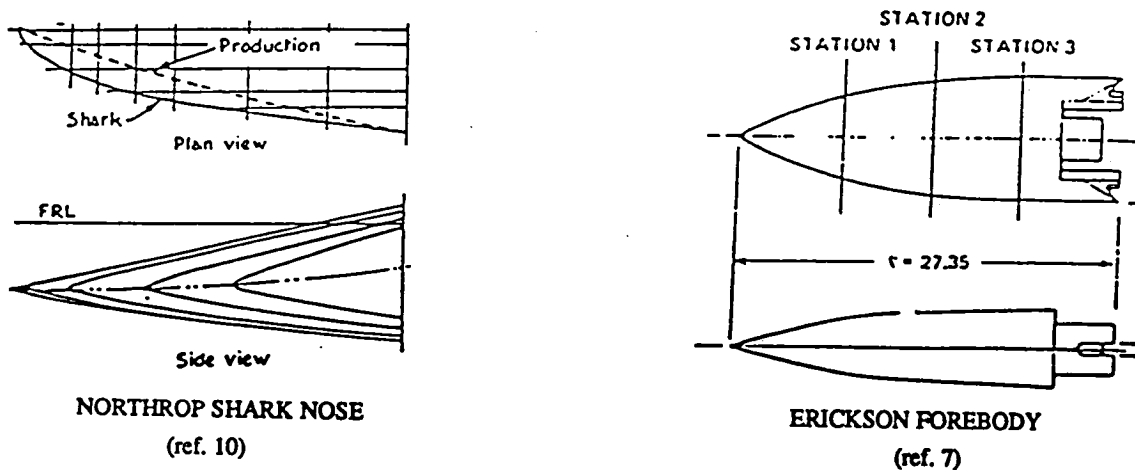


Figure 4. Goal of forebody design effort



(a) CROSS SECTIONS



RFC (ref. 8)

(b) PLAN AND PROFILE VIEWS

Figure 5. Samples of shapes employed in fighter forebody design

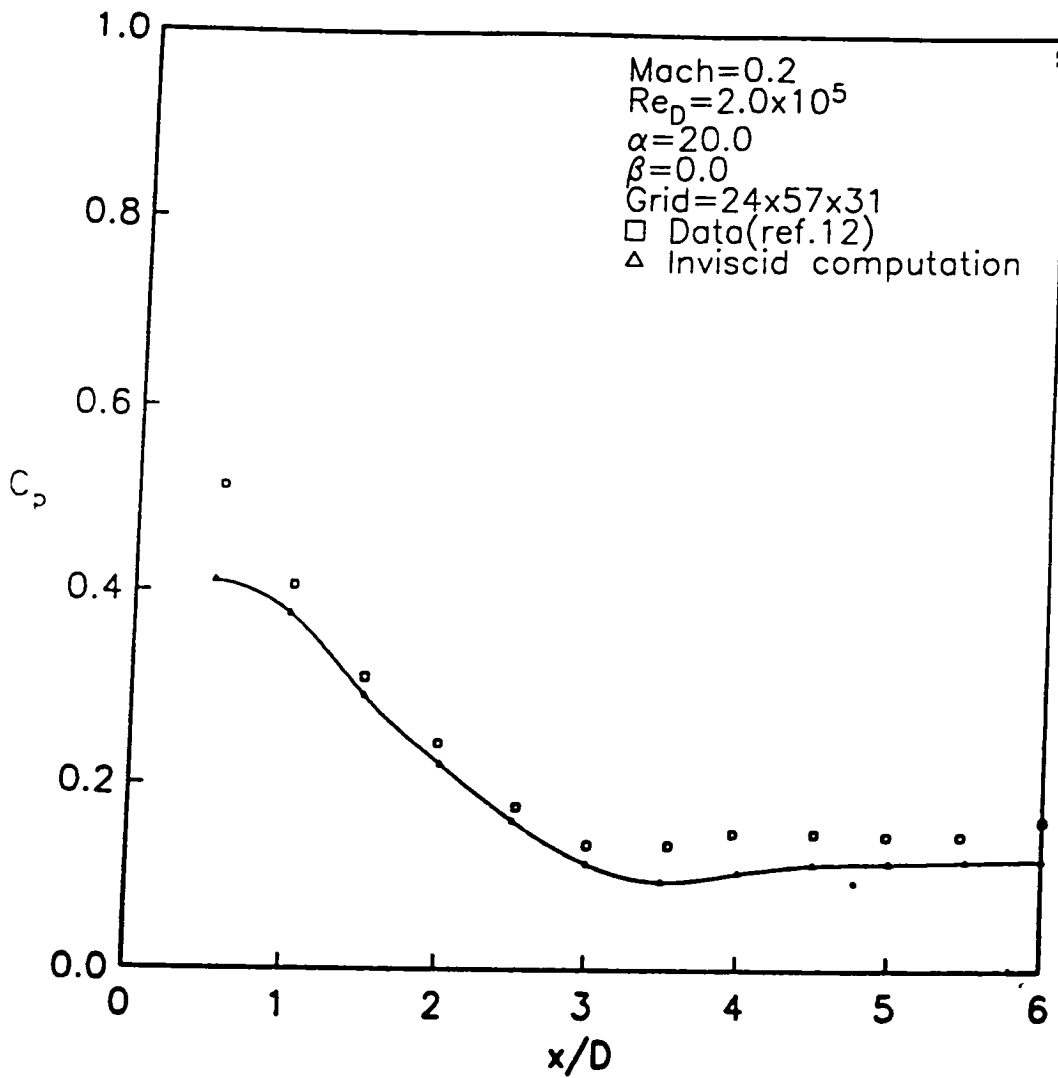


Figure 6. Tangent ogive crude grid Euler solution comparison with experimental data on windward plane.

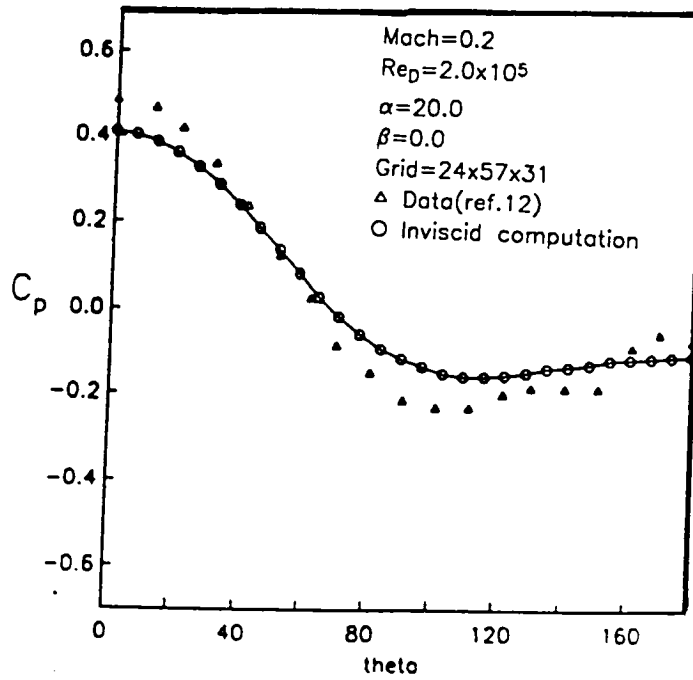


Figure 7(a). Tangent ogive crude grid Euler solution comparison with experimental data($x/d = 0.5$)

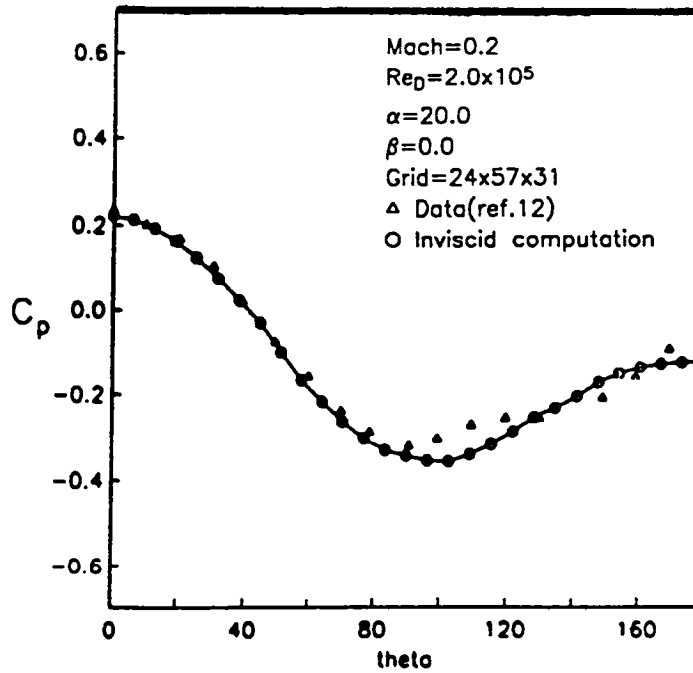


Figure 7(b). Tangent ogive crude grid Euler solution comparison with experimental data ($x/d = 2.0$)

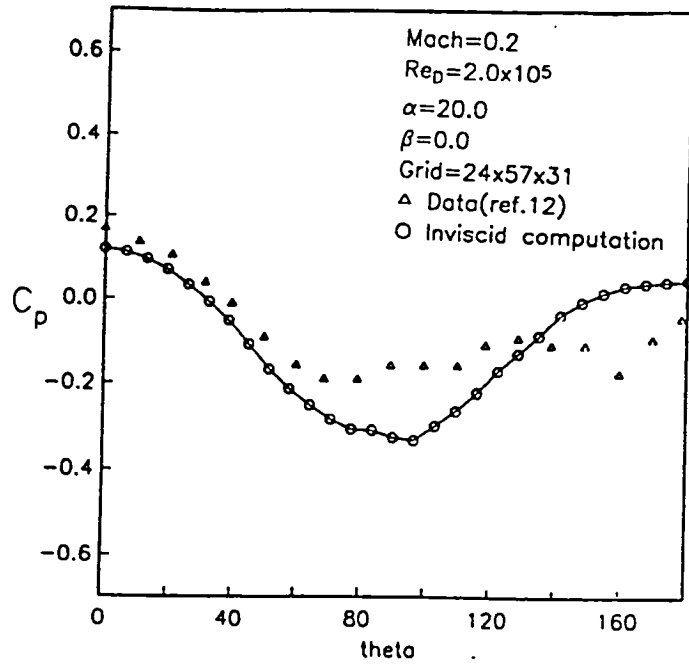


Figure 7(c). Tangent ogive crude grid Euler solution comparison with experimental data ($x/d = 3.5$)

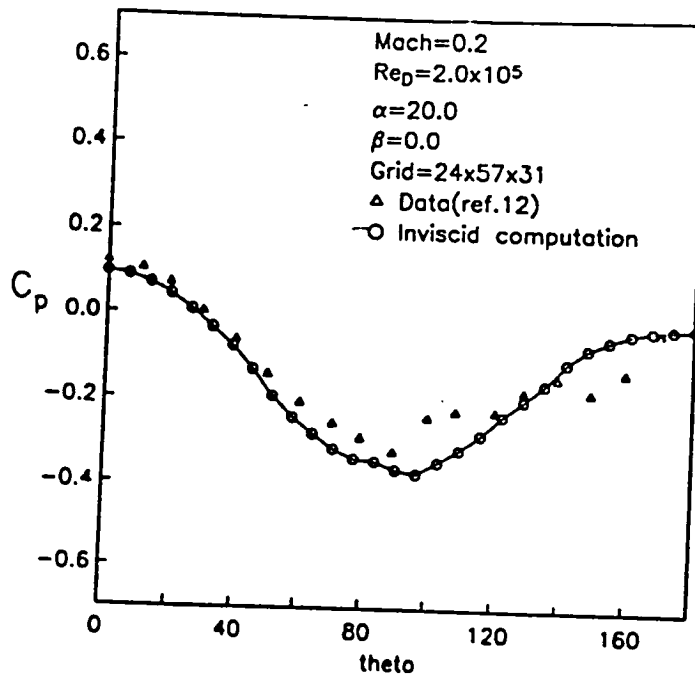


Figure 7(d). Tangent ogive crude grid Euler solution comparison with experimental data ($x/d = 6.0$)

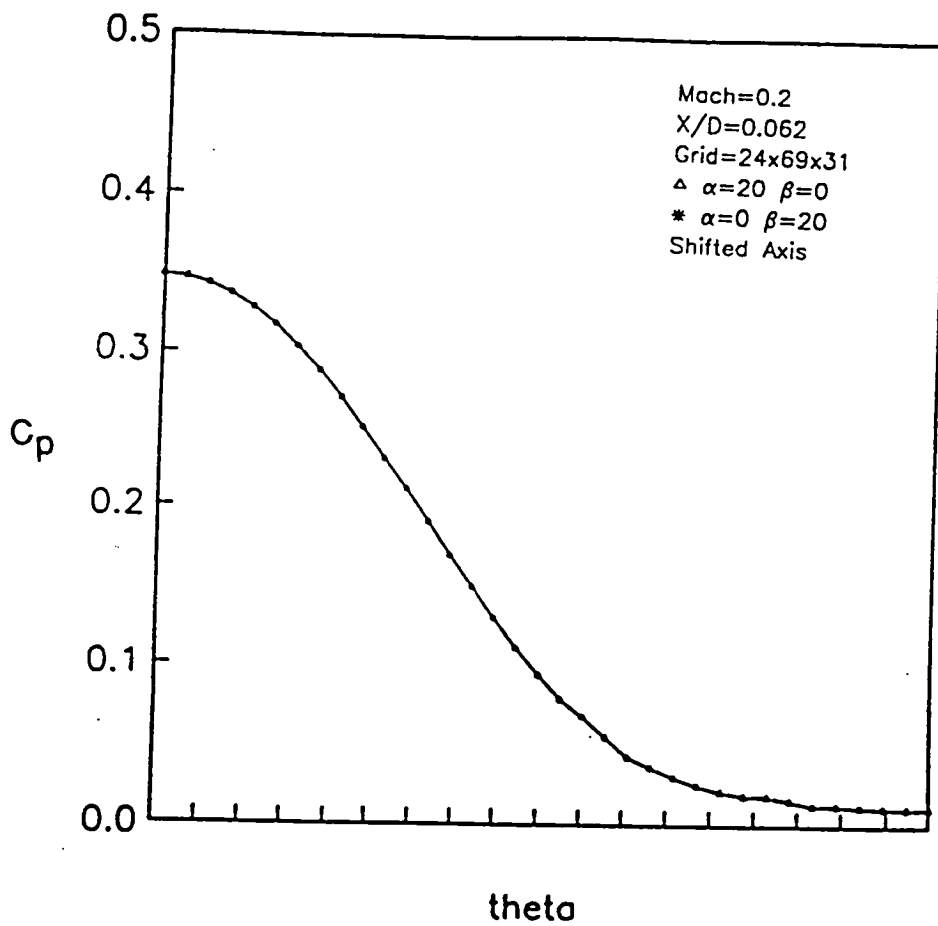


Figure 8(a). Tangent ogive : Demonstration of α / β results at $x/d = 0.062$ ($Re=2 \cdot 10^5$)

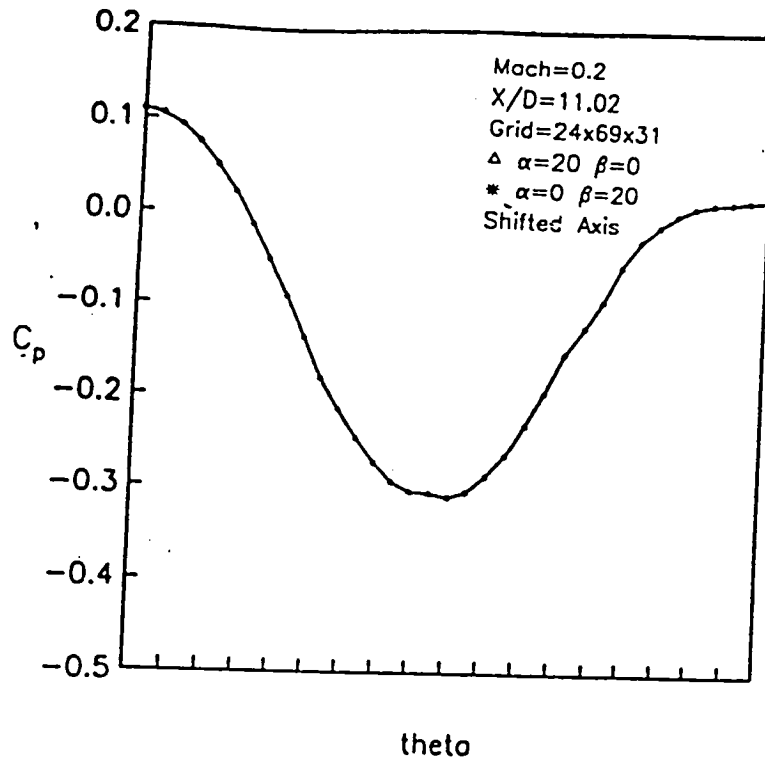


Figure 8(b). Tangent ogive : Demonstration of α / β results at $x/d = 11.02$ ($Re=2 \cdot 10^5$)

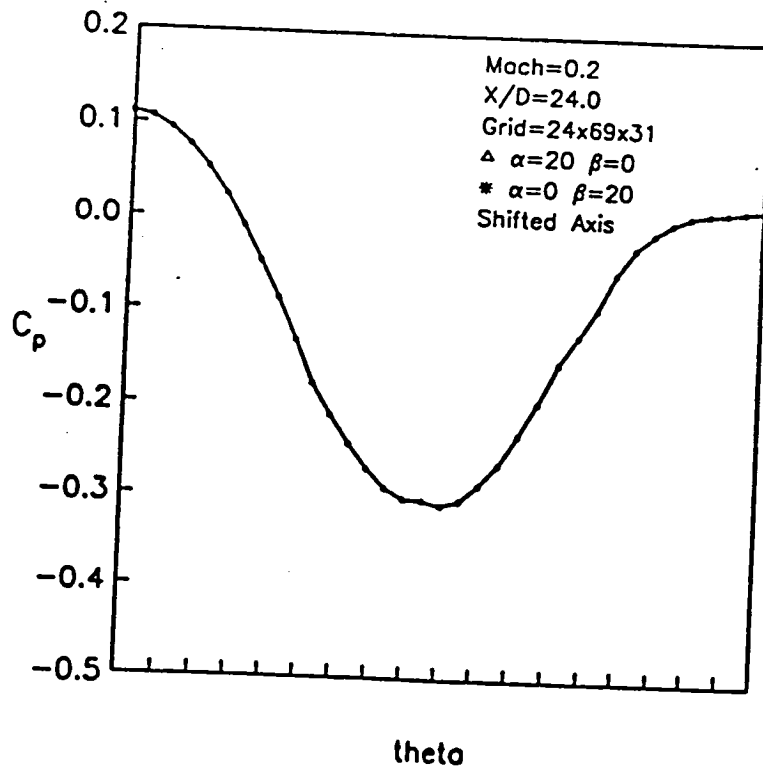


Figure 8(c). Tangent ogive : Demonstration of α / β results at $x/d = 24.0$ ($Re=2 \cdot 10^5$)

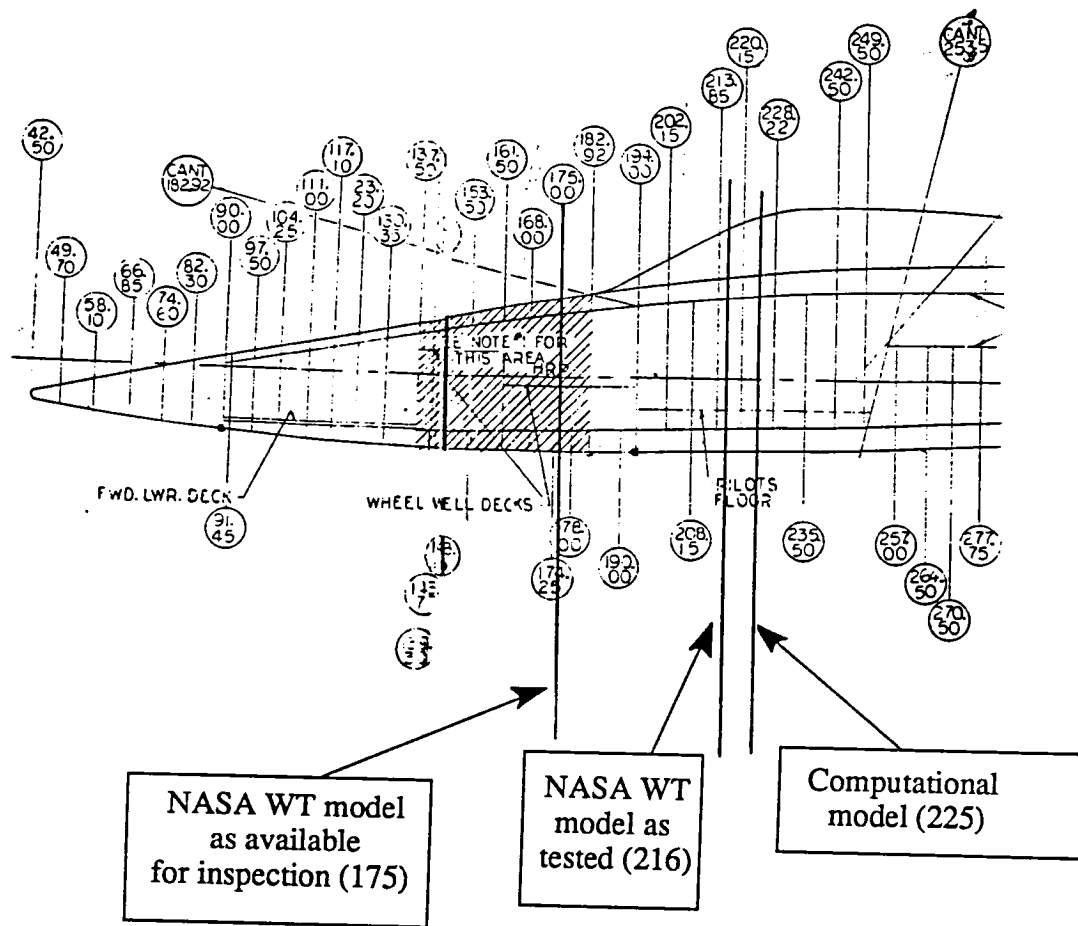


Figure 9(a). F-5A geometry (from Tom Heglund of Northrop)

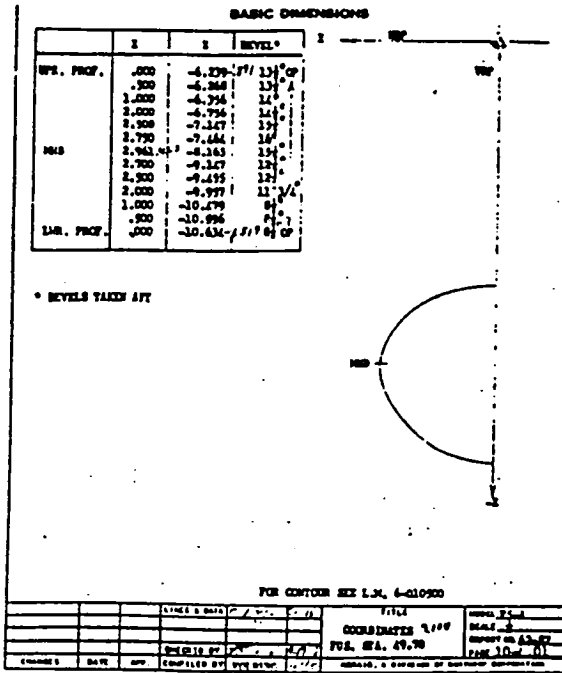


Figure 9(b). F5-A geometry: FS 49.70 in.(forward station)
(from Tom Heglund of Northrop)

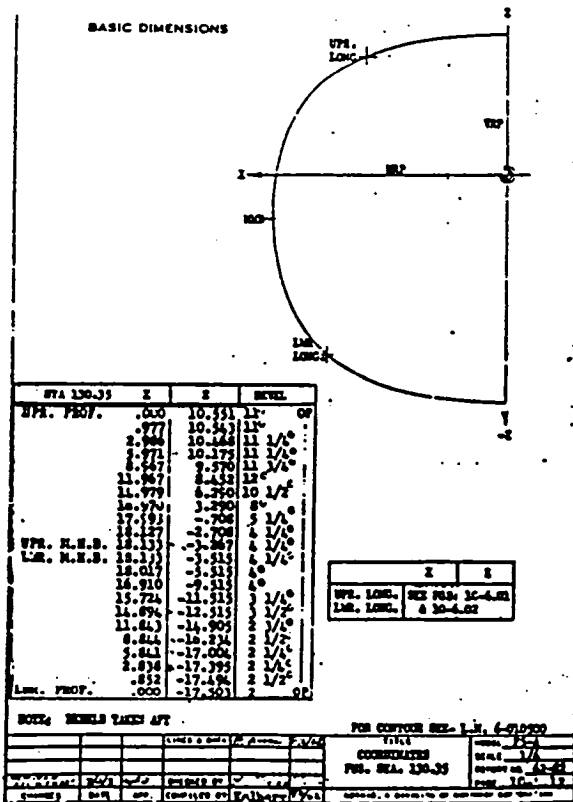


Figure 9(c). F5-A geometry: FS 130.35 in.(just prior to straight line side beginning)
(from Tom Heglund of Northrop)

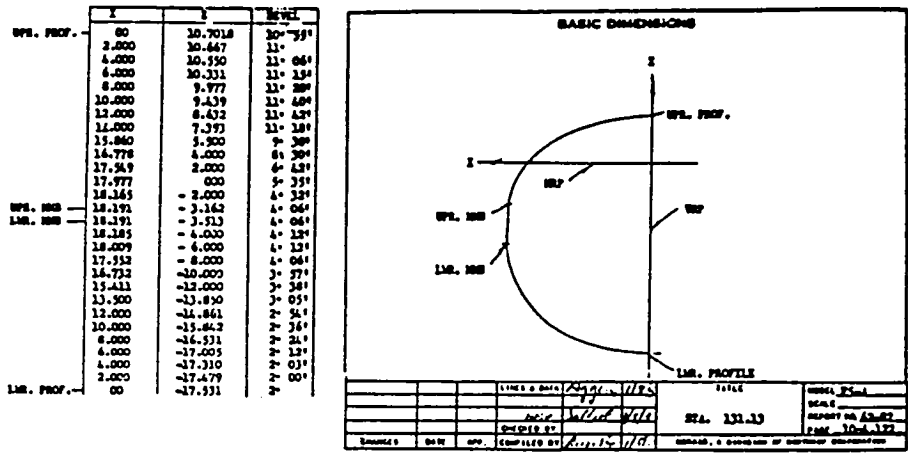


Figure 9(d). F5-A geometry: FS 131.13 in. (just aft of straight line side beginning)
(from Tom Heglund of Northrop)

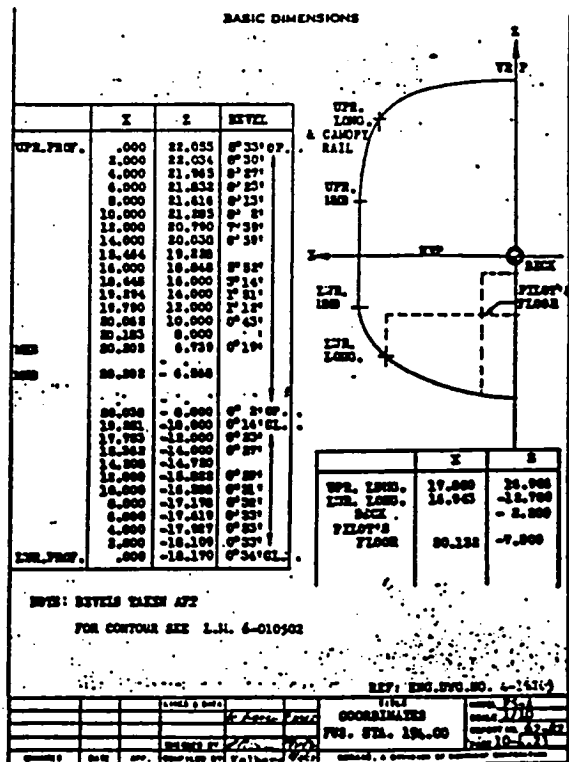


Figure 9(e). F5-A geometry: FS 194.00 in. (end station)
(from Tom Heglund of Northrop)

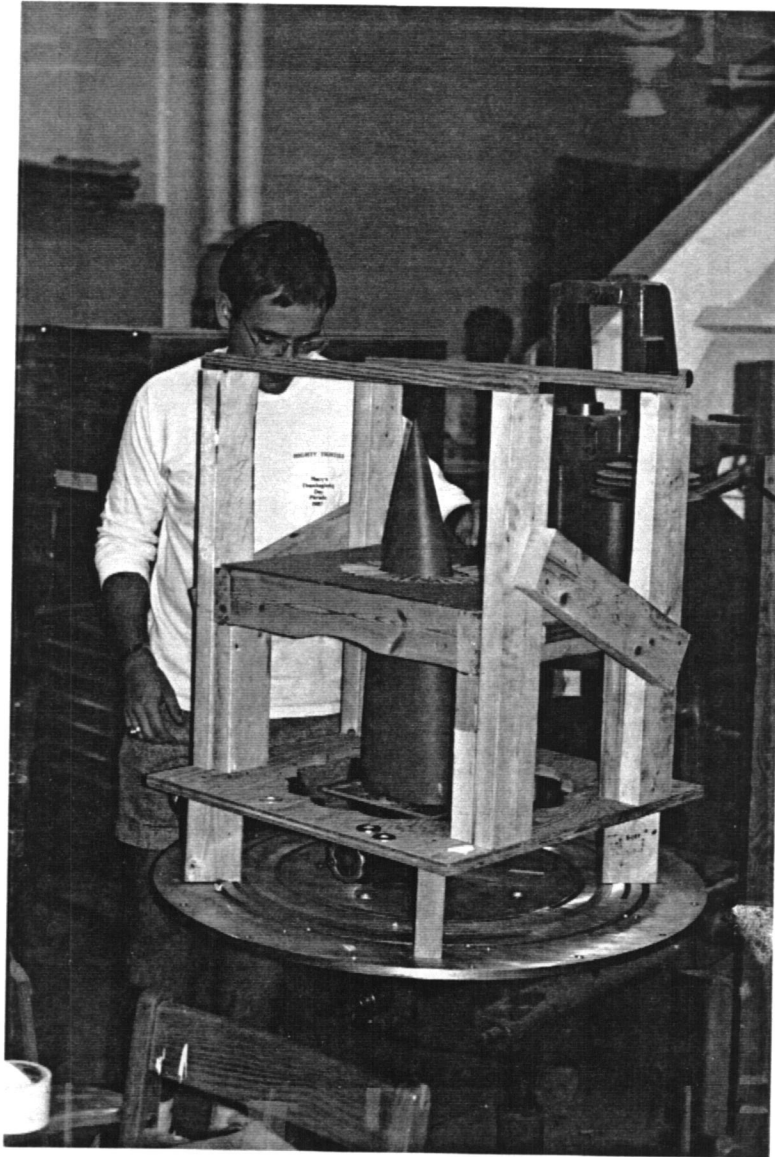


Figure 10(a). F5-A wind tunnel model being measured to determine the shape.

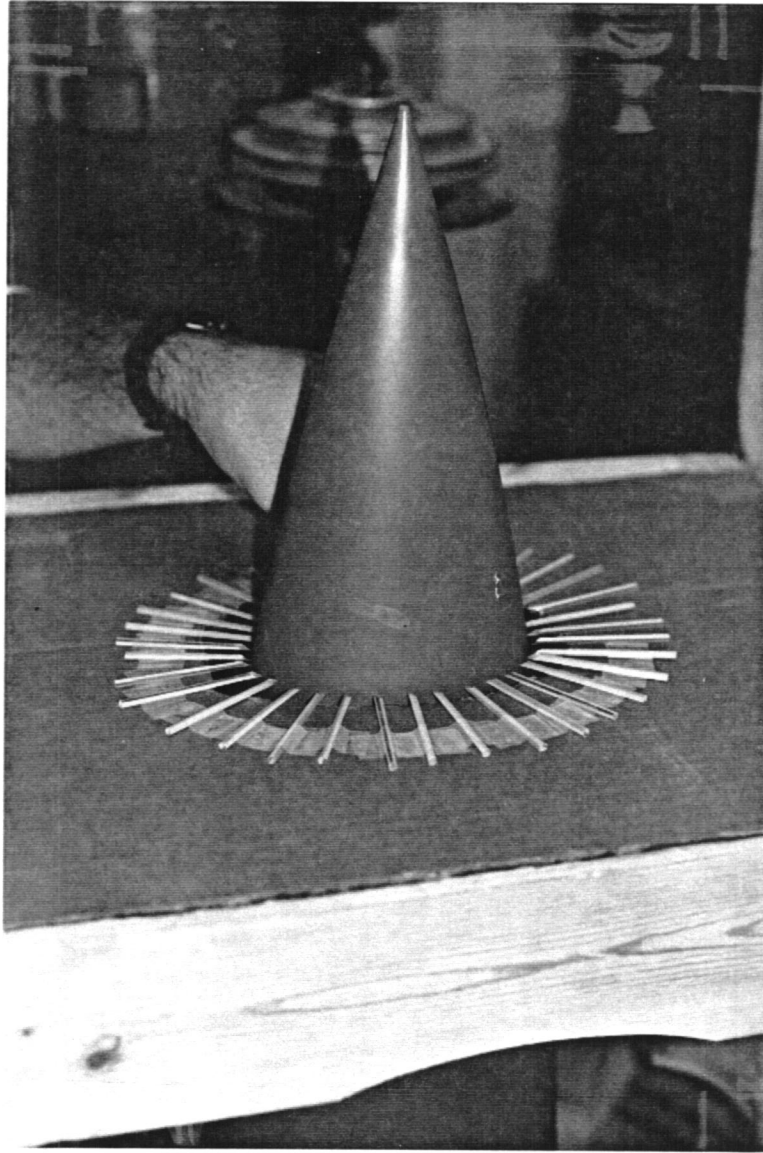


Figure 10(b). F5-A wind tunnel model being measured to determine the shape (close-up).

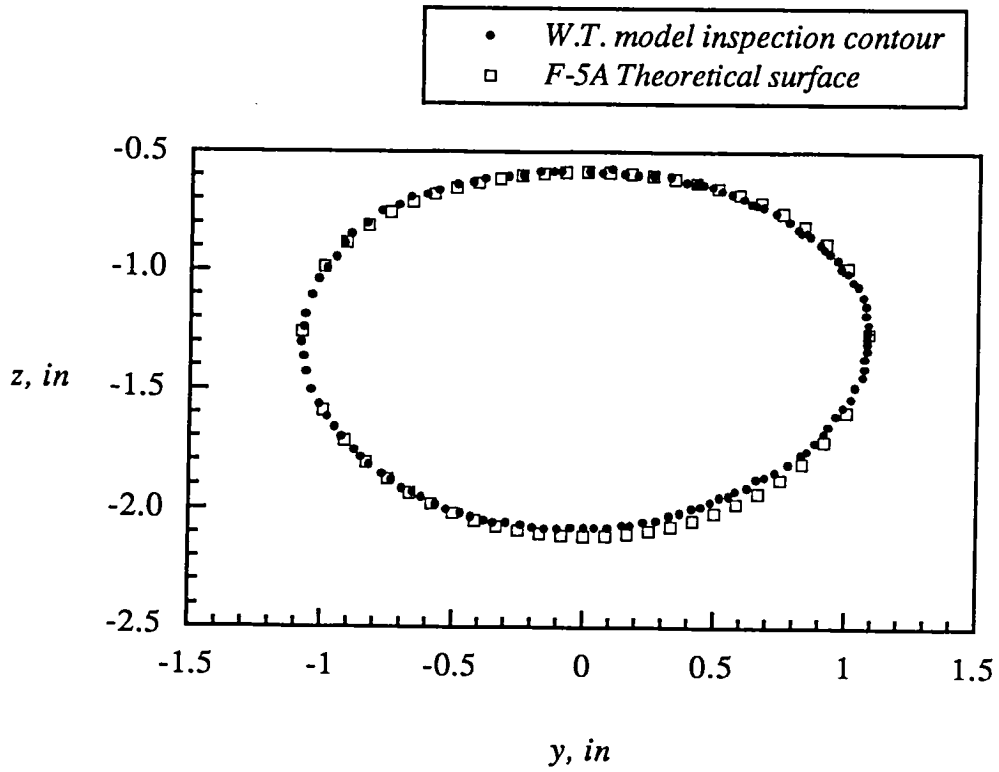


Figure 11(a). Comparison of F-5A geometry: Station 3.375 in from nose

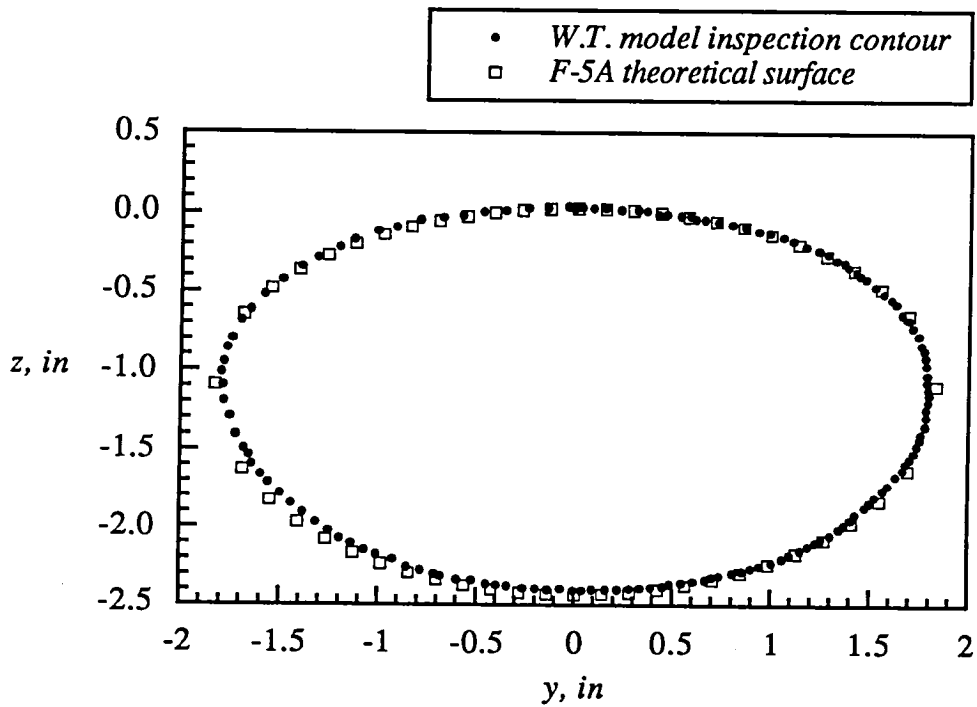


Figure 11(b). Comparison of F-5A geometry: Station 6.25 in from nose

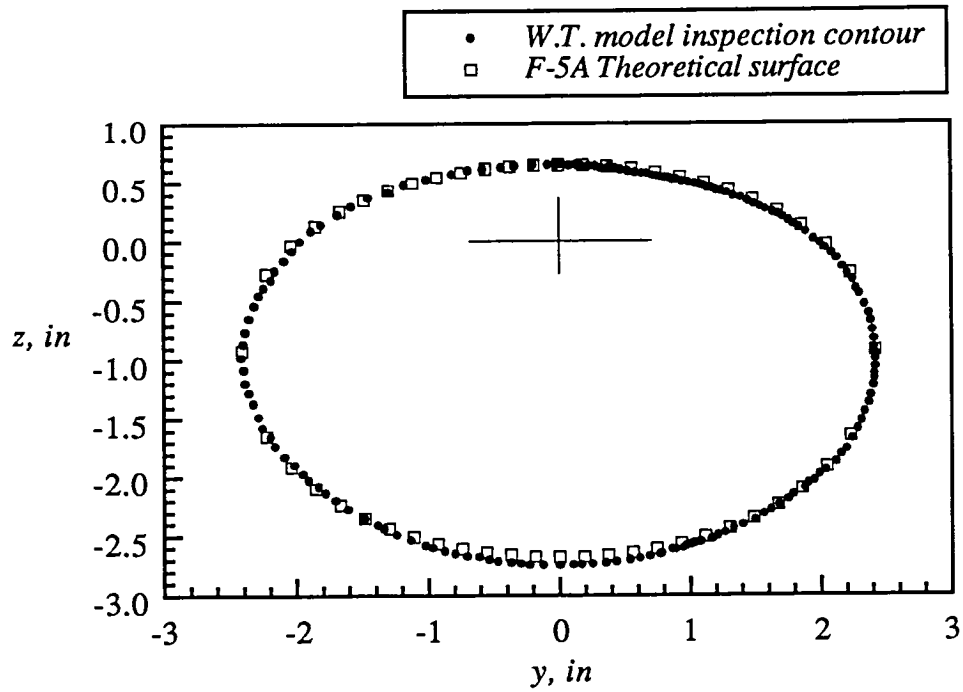


Figure 11(c). Comparison of F-5A geometry: Station 9.1875 *in* from nose

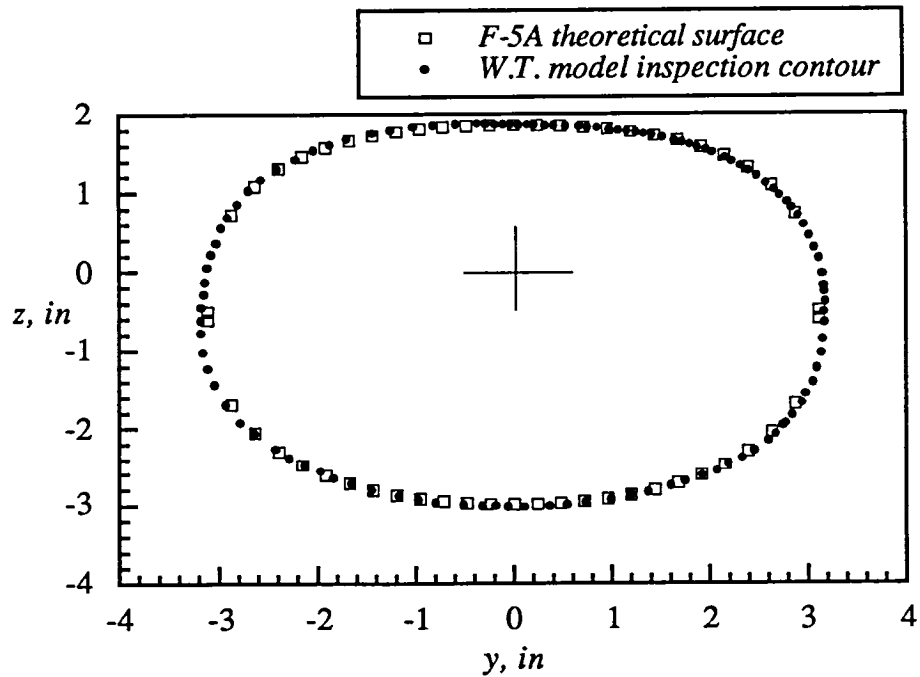


Figure 11(d). Comparison of F-5A geometry: Station 15.3125 *in* from nose

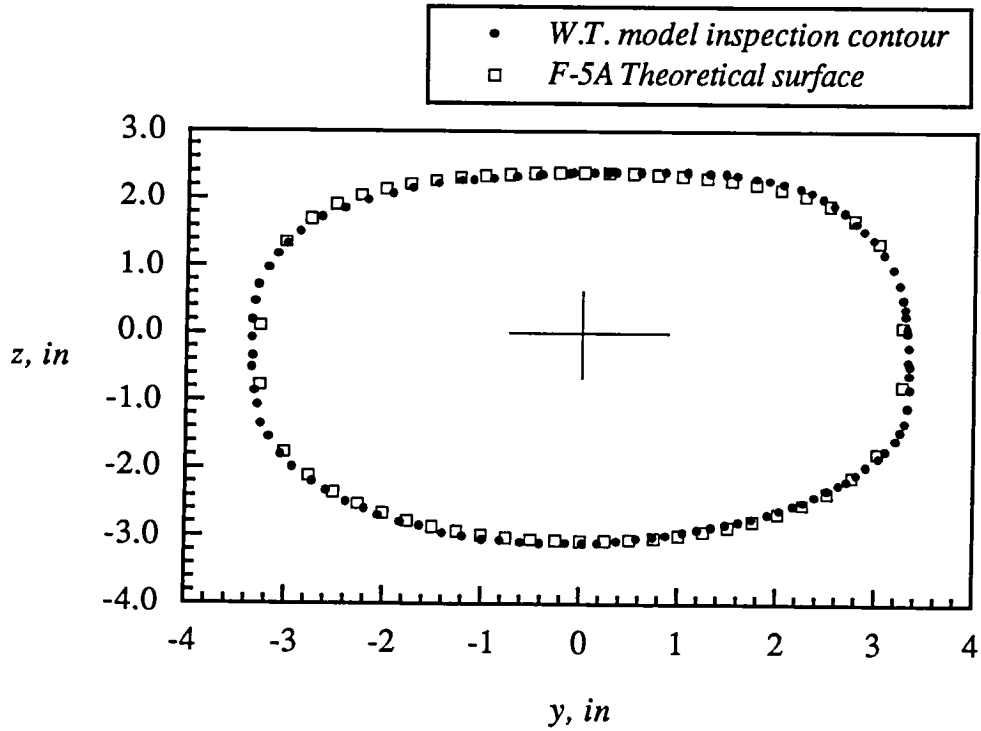


Figure 11(e). Comparison of F-5A geometry: Station 18.0625 *in* from nose

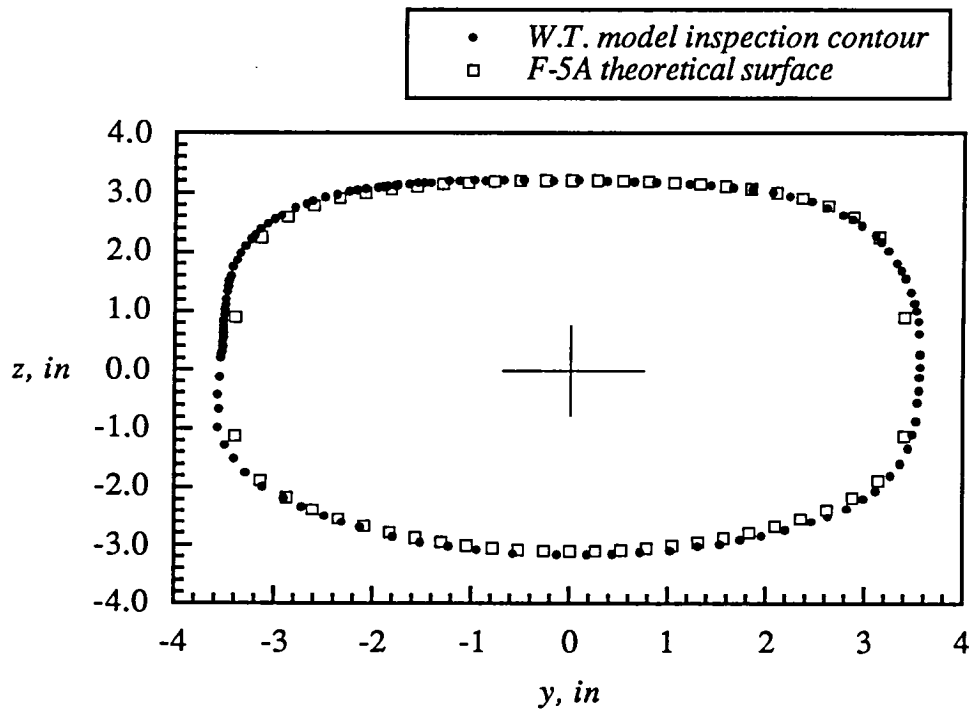


Figure 11(f). Comparison of F-5A geometry: Station 22.5 *in* from nose

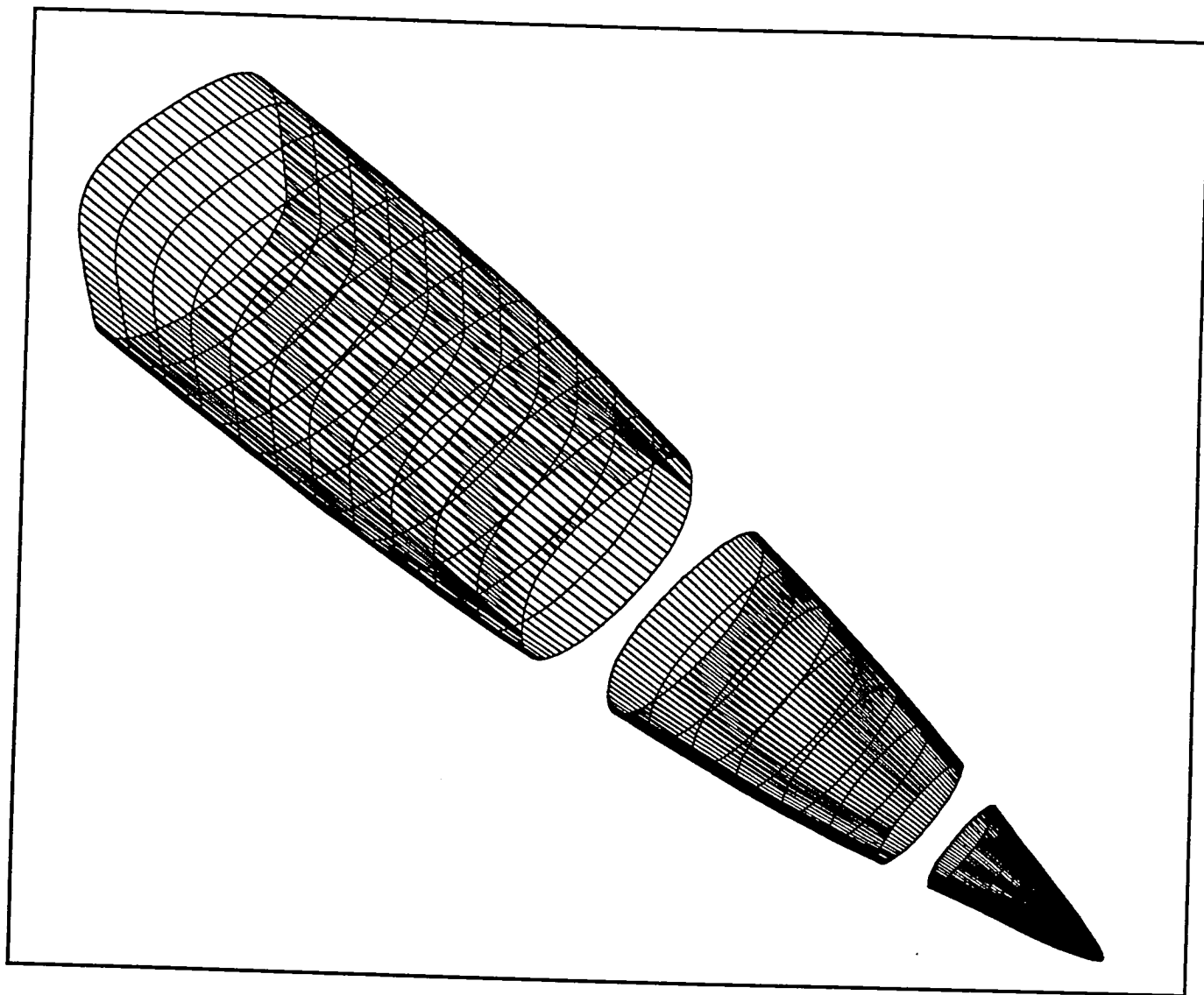
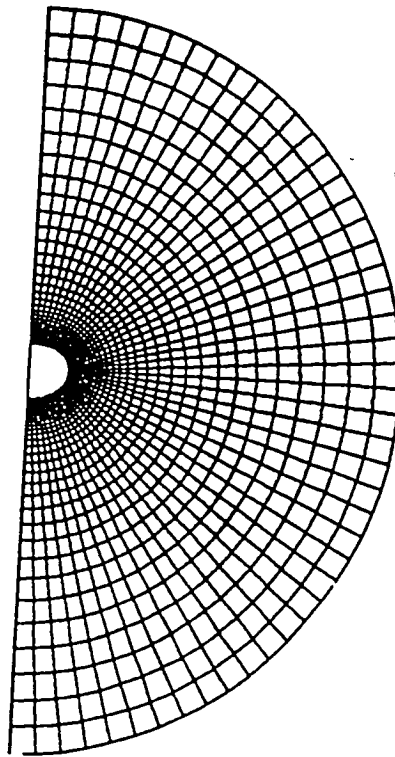
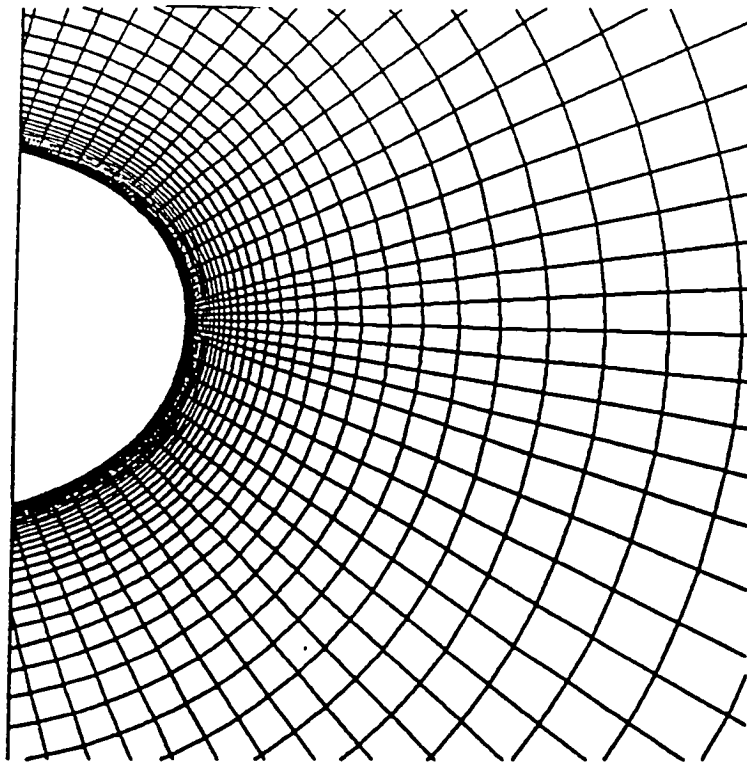


Figure 12. Wireframe model of F-5A surface definition

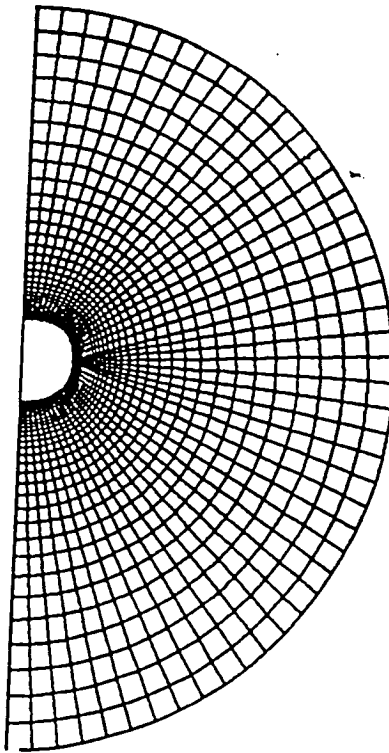


(a) cross sectional grid

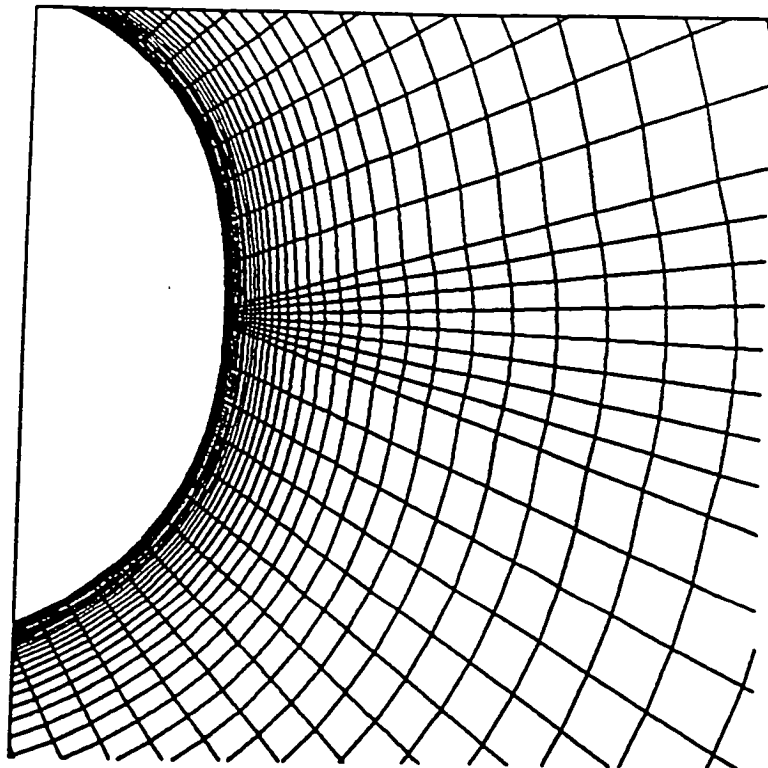


(b) closeup near surface

Figure 13. F5-A cross sectional grid and closeup near surface at $x = 9.061$ in.
(model scale)

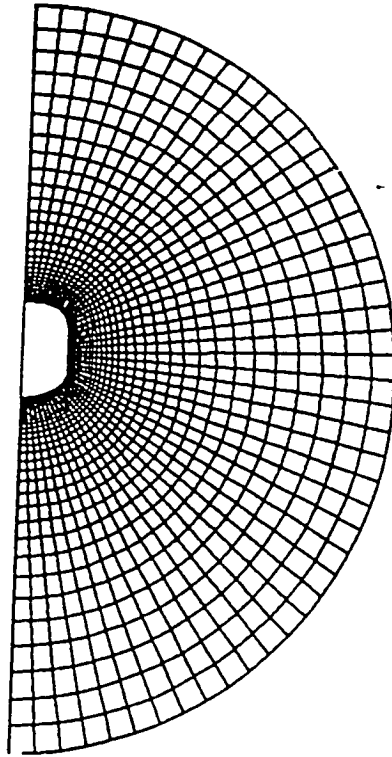


(a) cross sectional grid

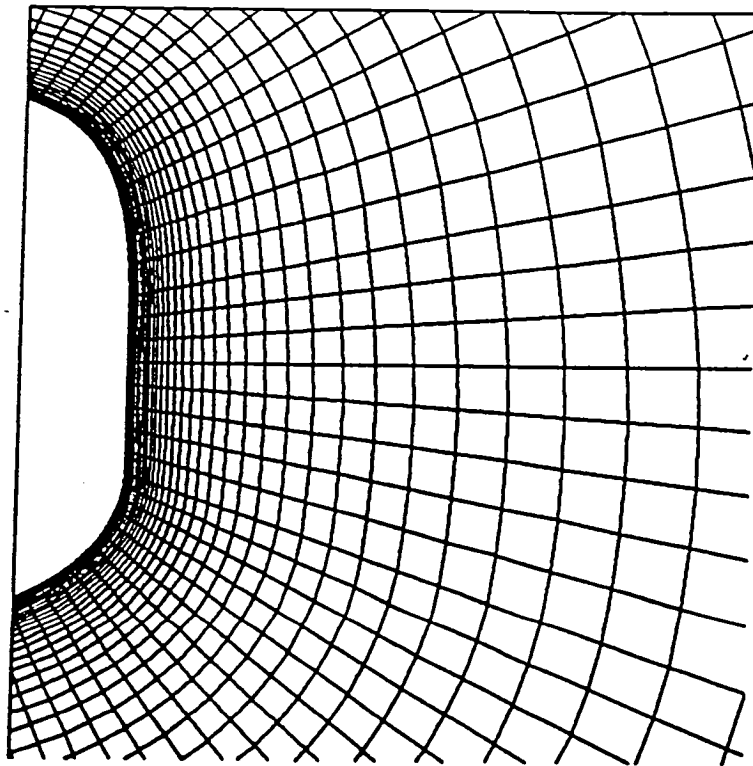


(b) closeup near surface

**Figure 14. F5-A cross sectional grid and closeup near surface at $x = 15.44$ in.
(model scale)**



(a) cross sectional grid



(b) closeup near surface

**Figure 15. F5-A cross sectional grid and closeup near surface at $x = 29.6$ in.
(model scale)**

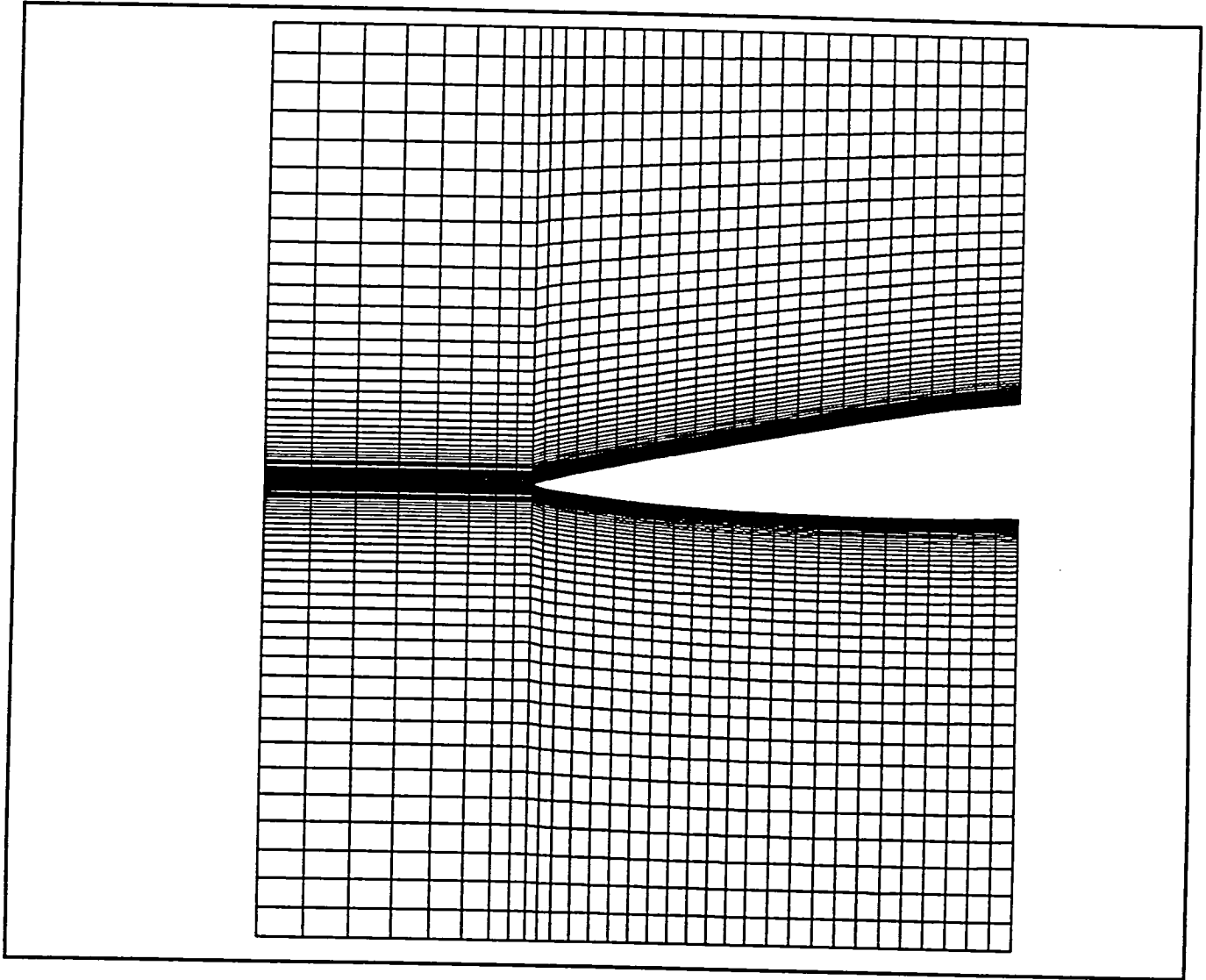


Figure 16. F-5A longitudinal pattern of grid (PLOT3D)

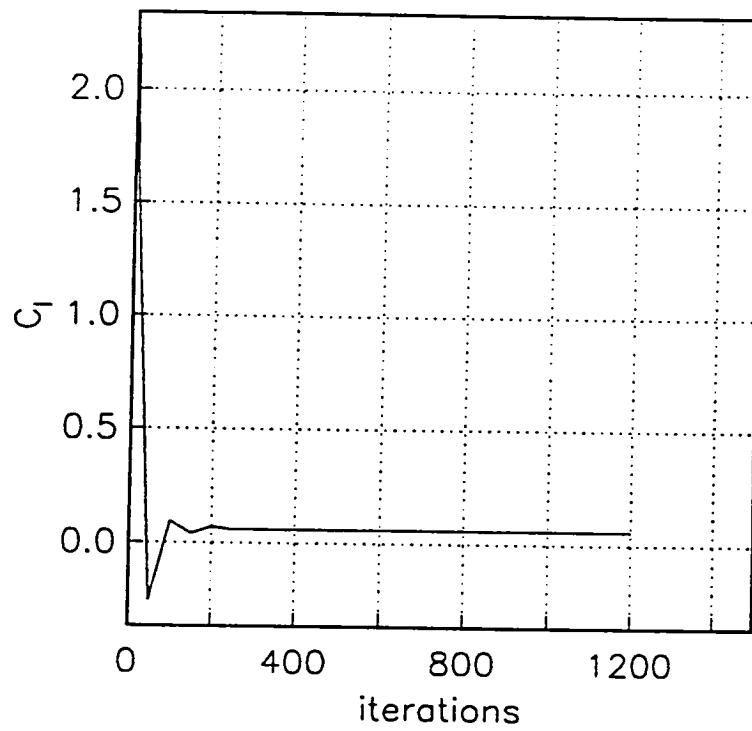
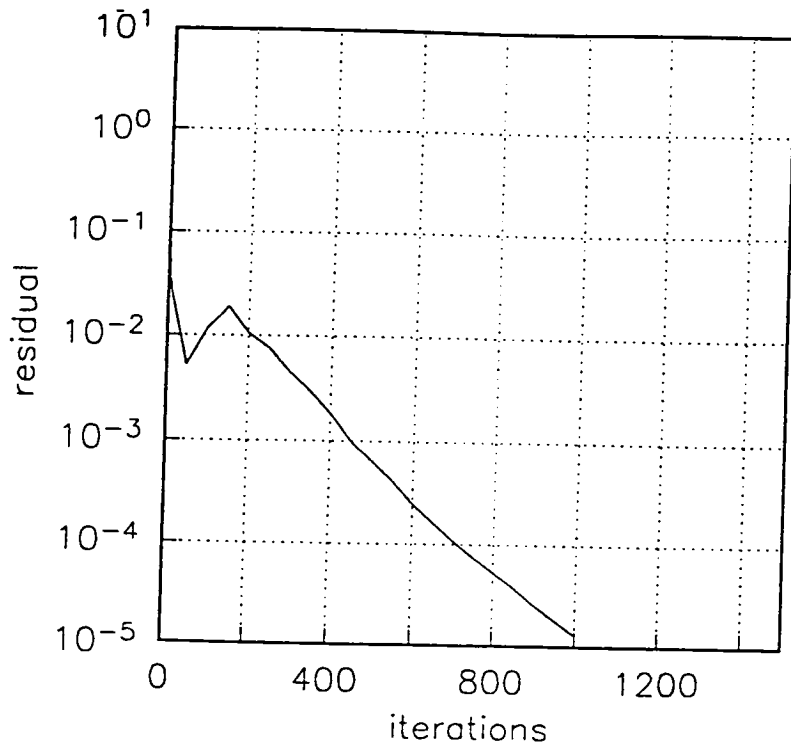


Figure 17. F5-A convergence history (inviscid) $\alpha = 40^\circ$ and $\beta = 5^\circ$

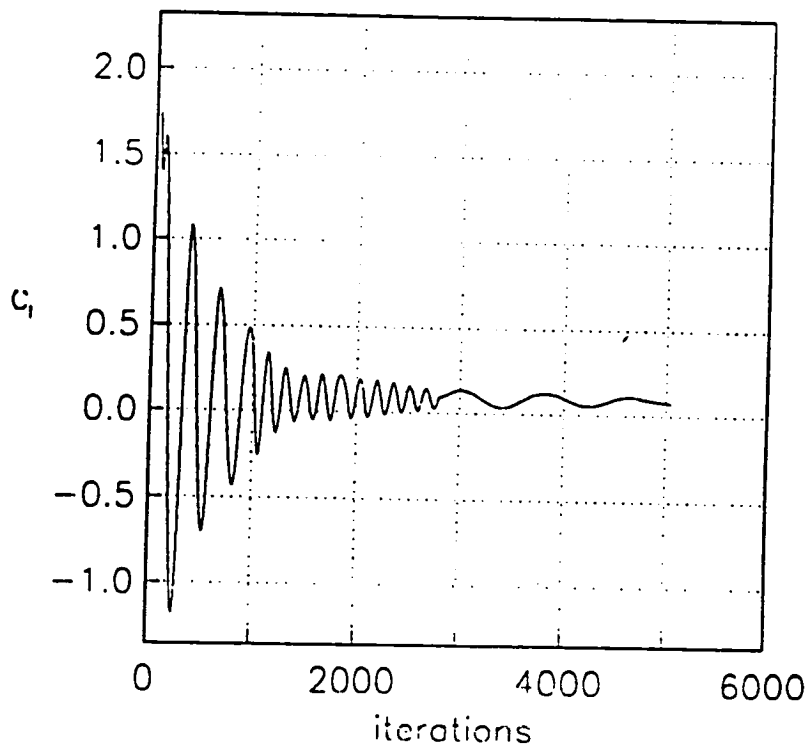
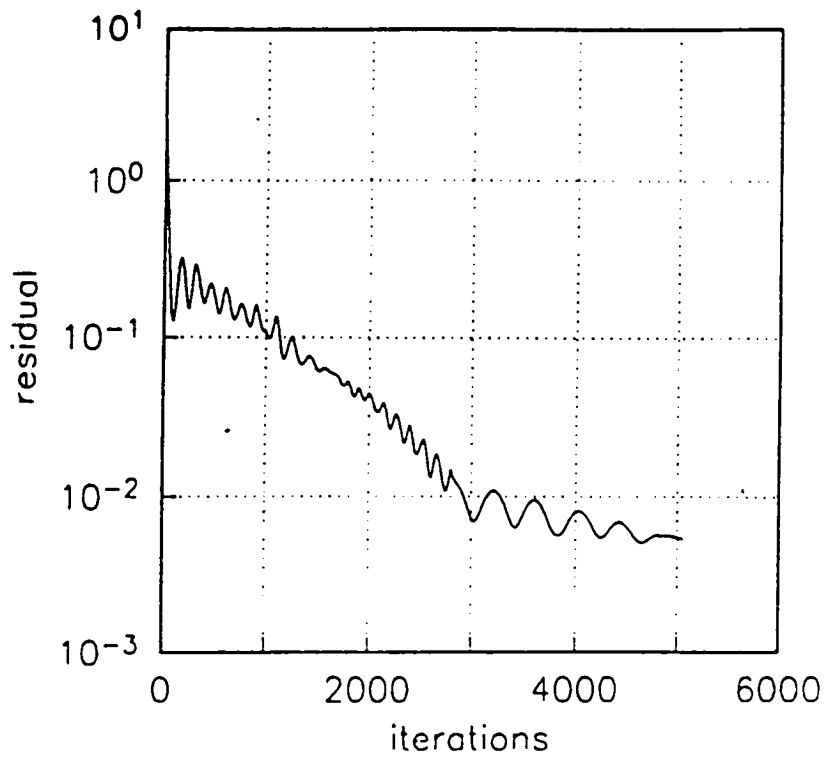


Figure 18(a). F5-A convergence history (turbulent) $\alpha = 40^\circ$ and $\beta = 5^\circ$

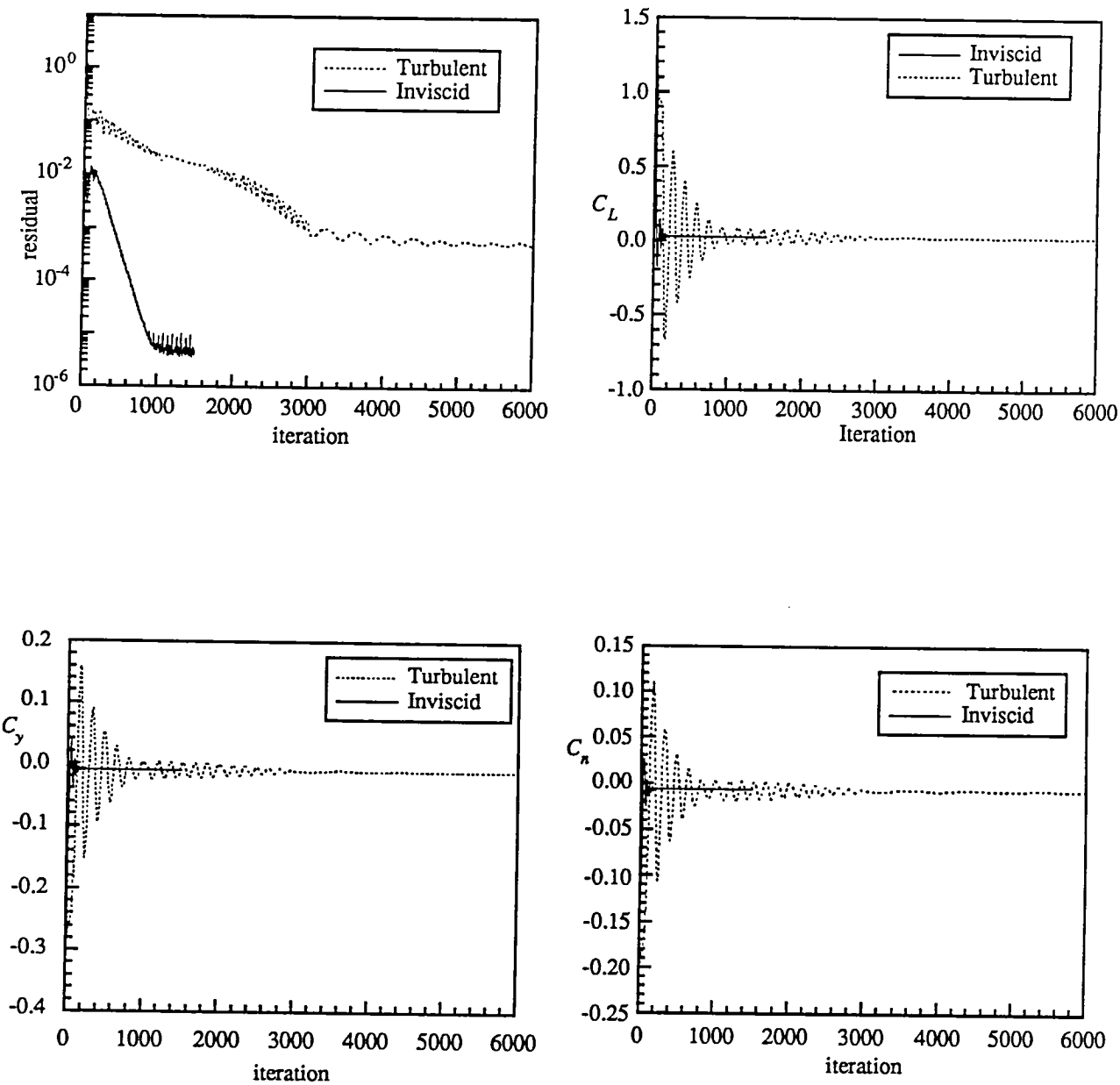


Figure 18(b). F-5A convergence history $\alpha = 20^\circ$ and $\beta = 5^\circ$

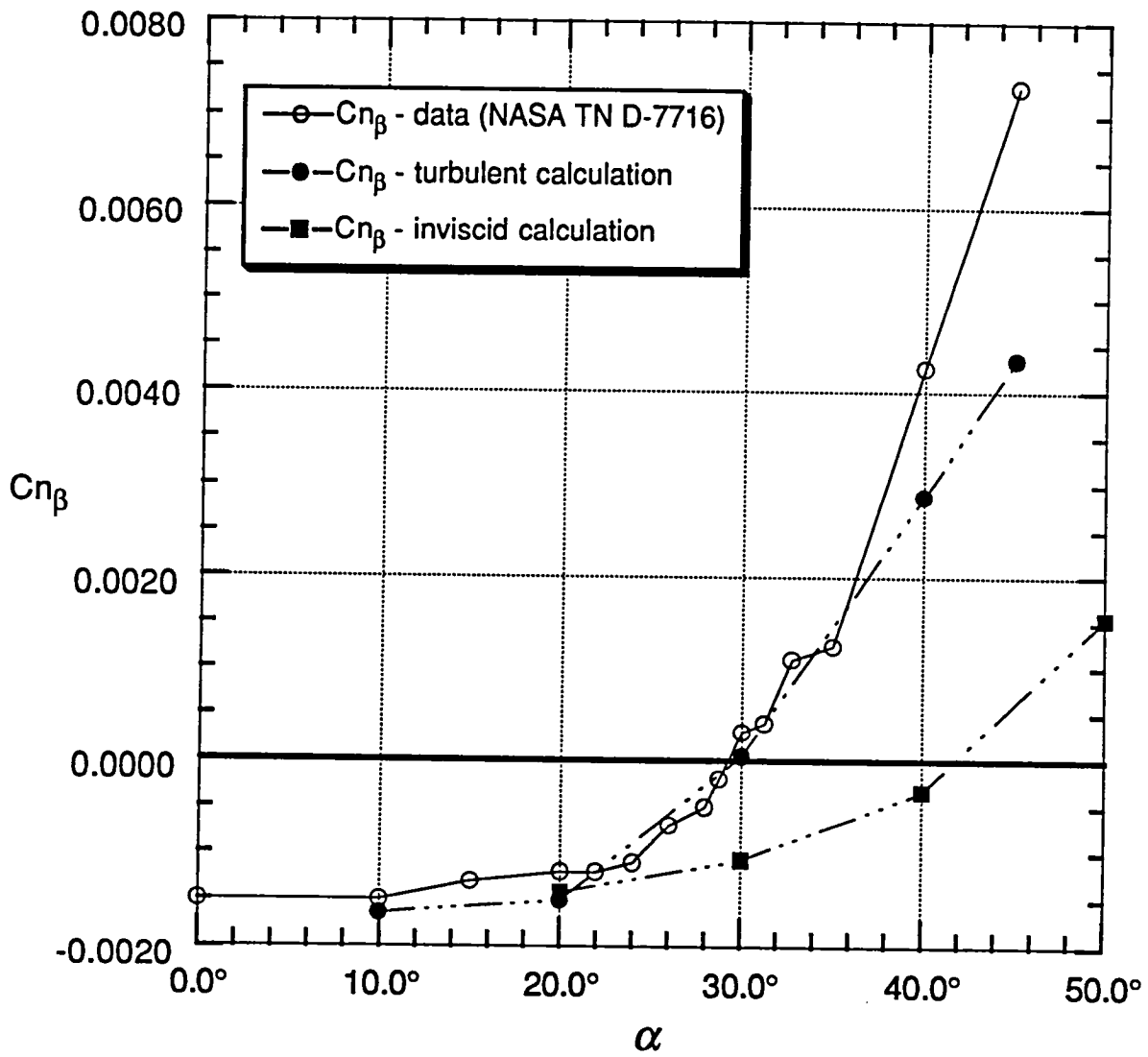


Figure 19. F5-A directional stability: comparison of calculation with experiment.

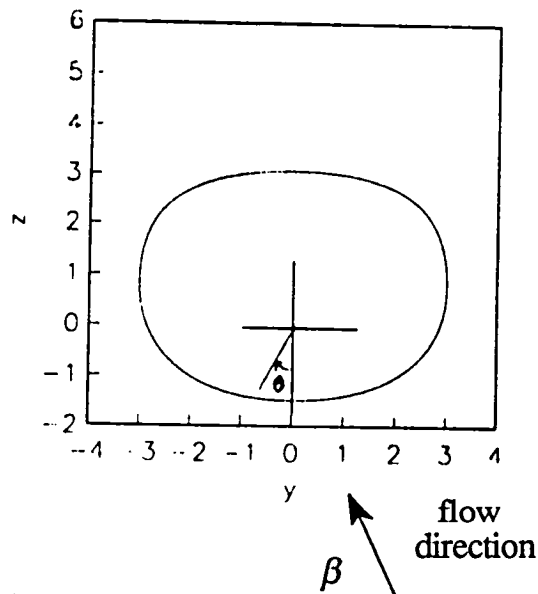
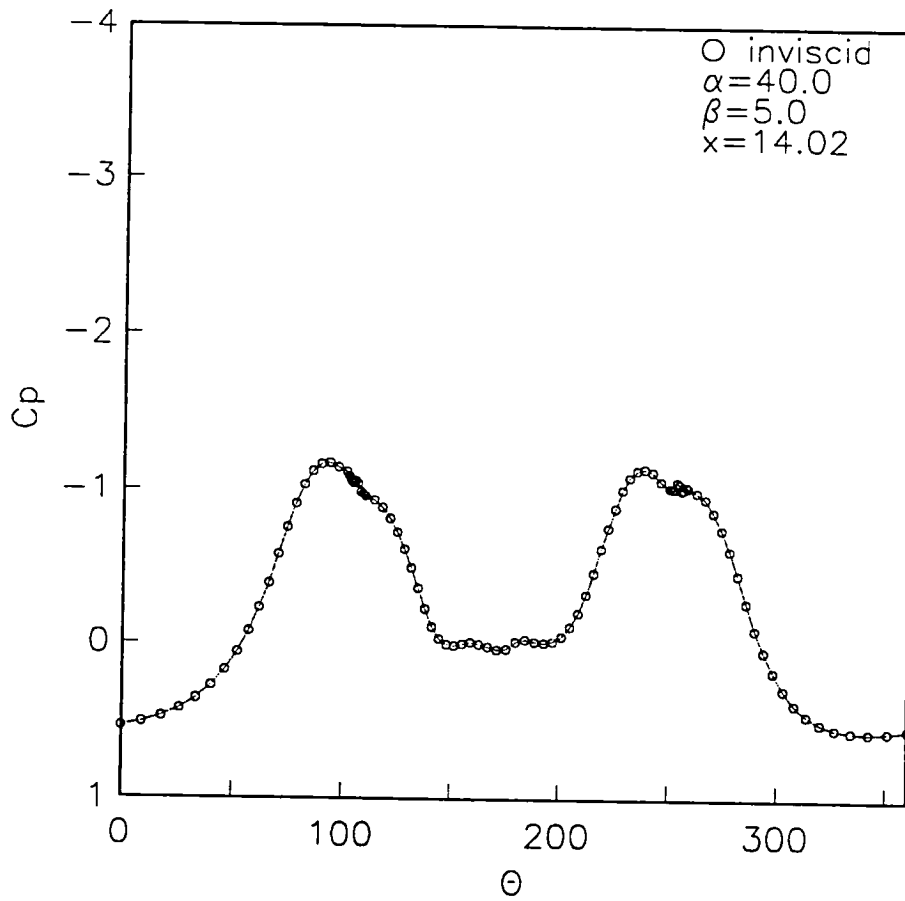


Figure 20(a). F5-A inviscid surface pressure distribution at $x = 14.02$ in.
 ($M=0.2$)

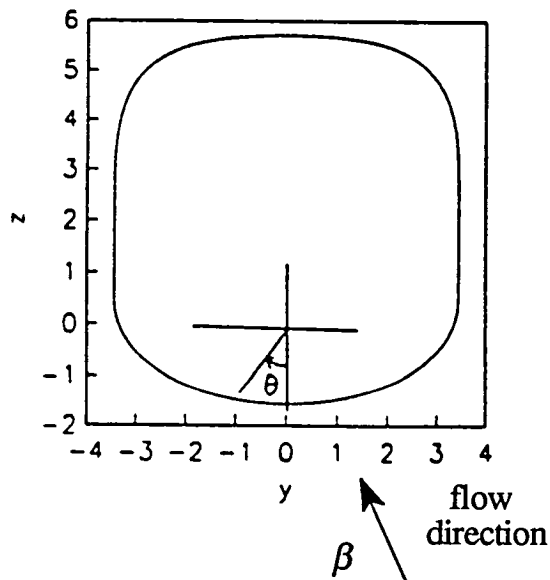
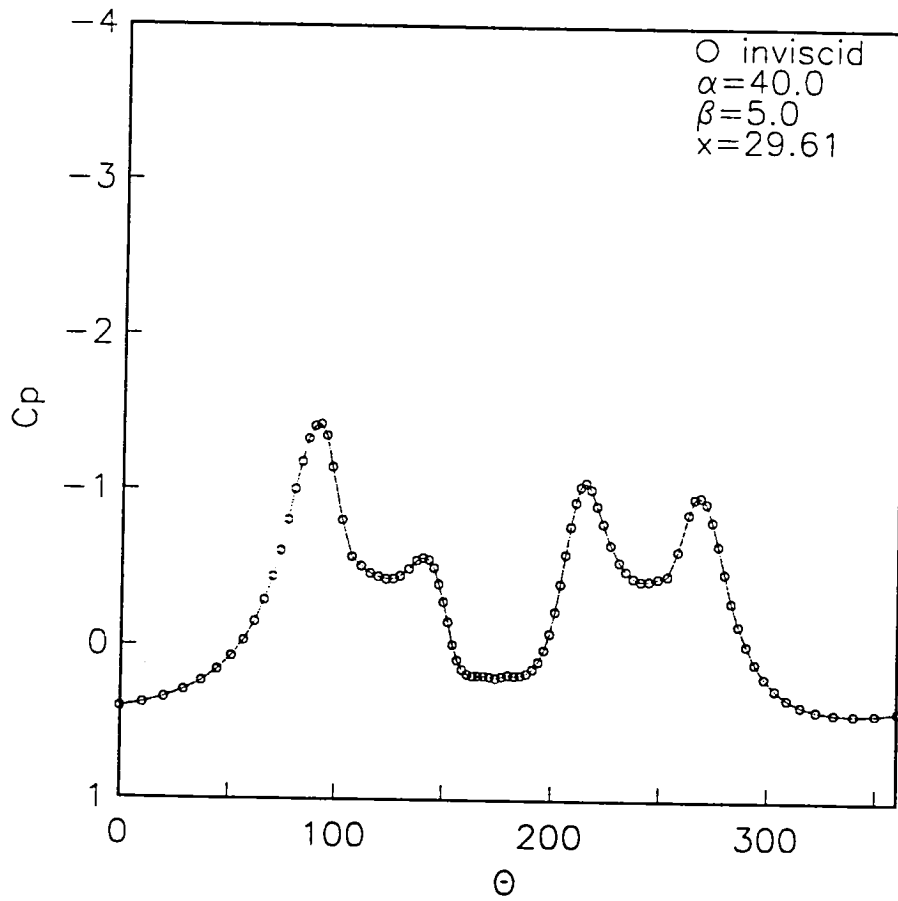


Figure 20(b). F5-A inviscid surface pressure distribution at $x = 29.61$ in.
 ($M=0.2$)

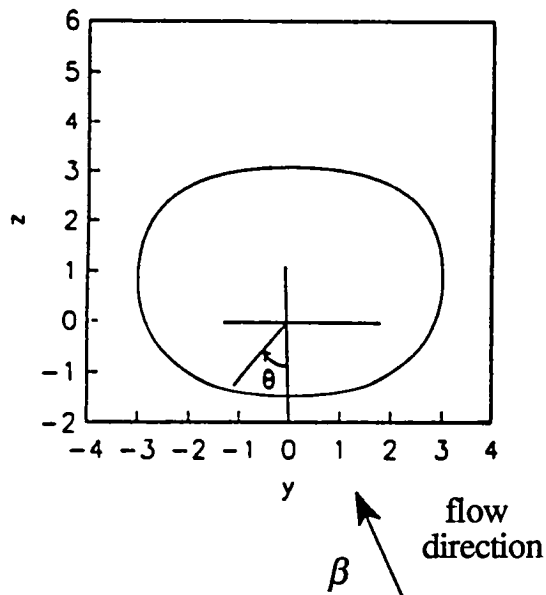
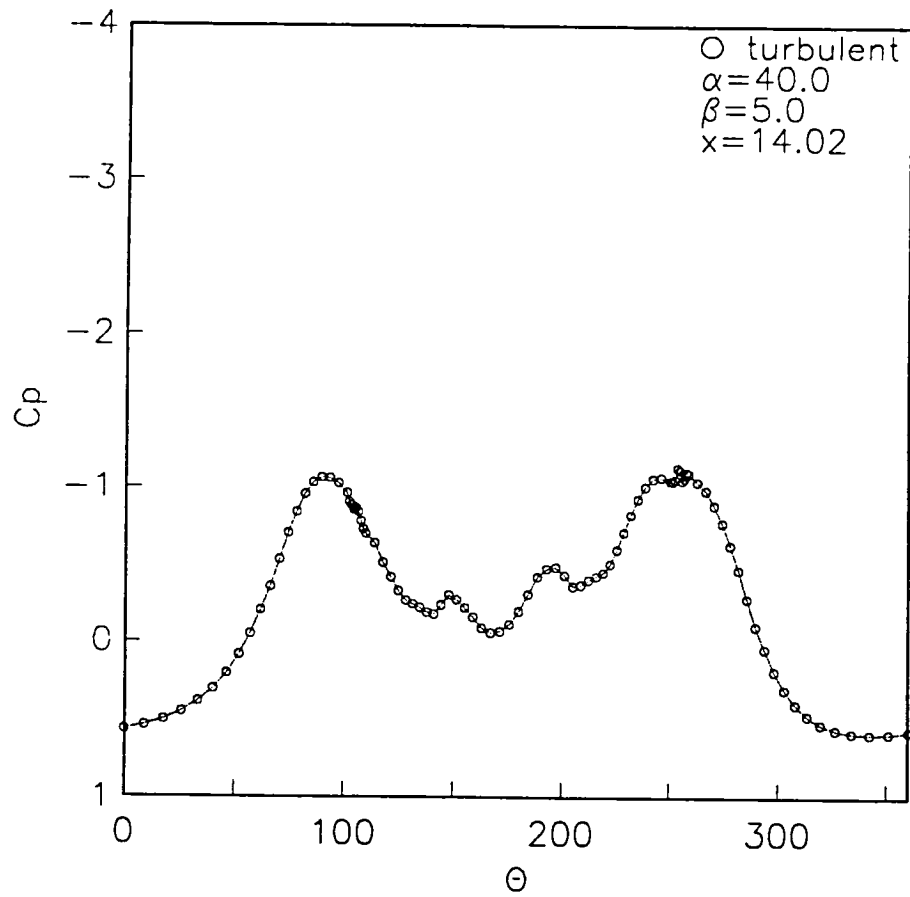


Figure 21(a). F5-A turbulent surface pressure distribution at $x = 14.02$ in.
 ($M=0.2, Re_c = 1.25 \cdot 10^6$)

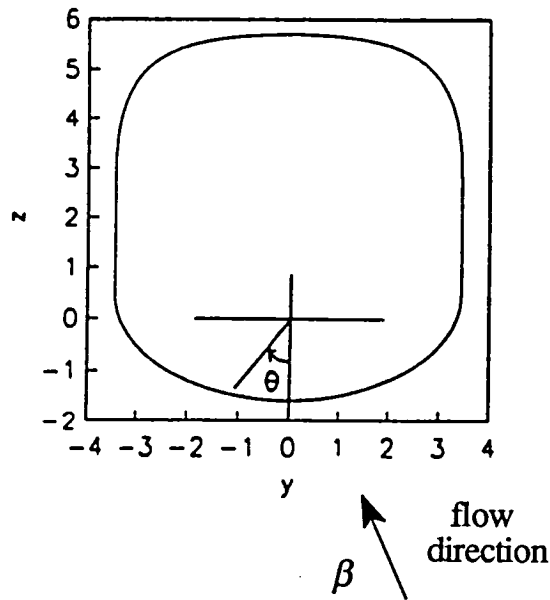
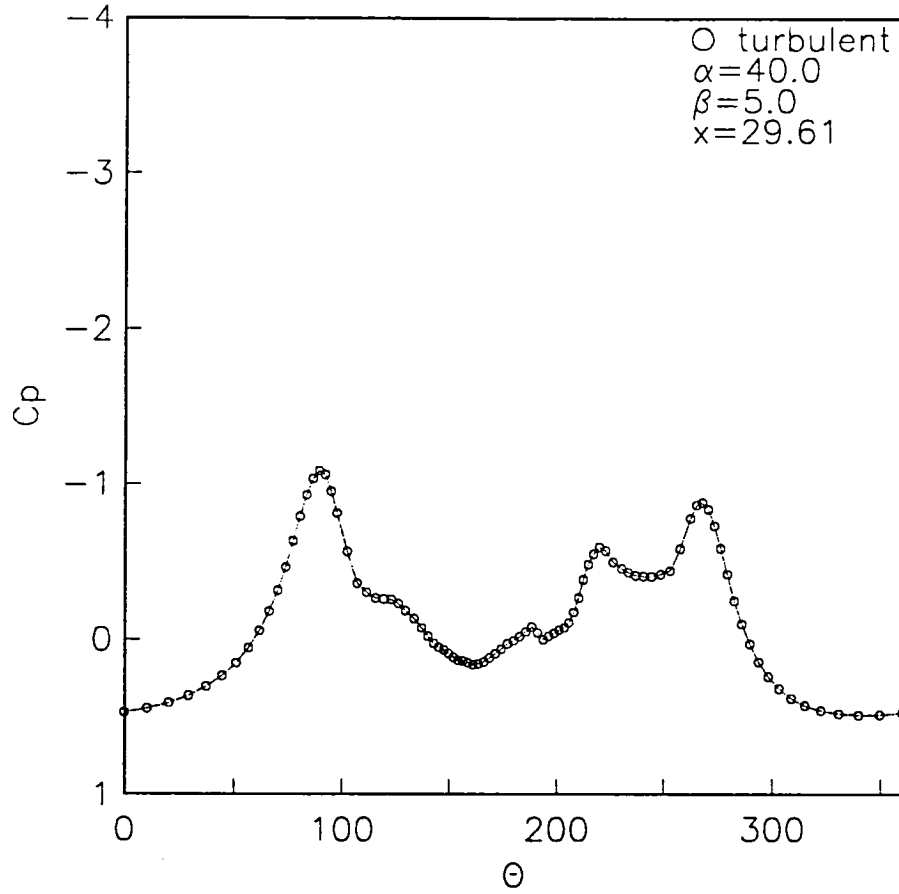
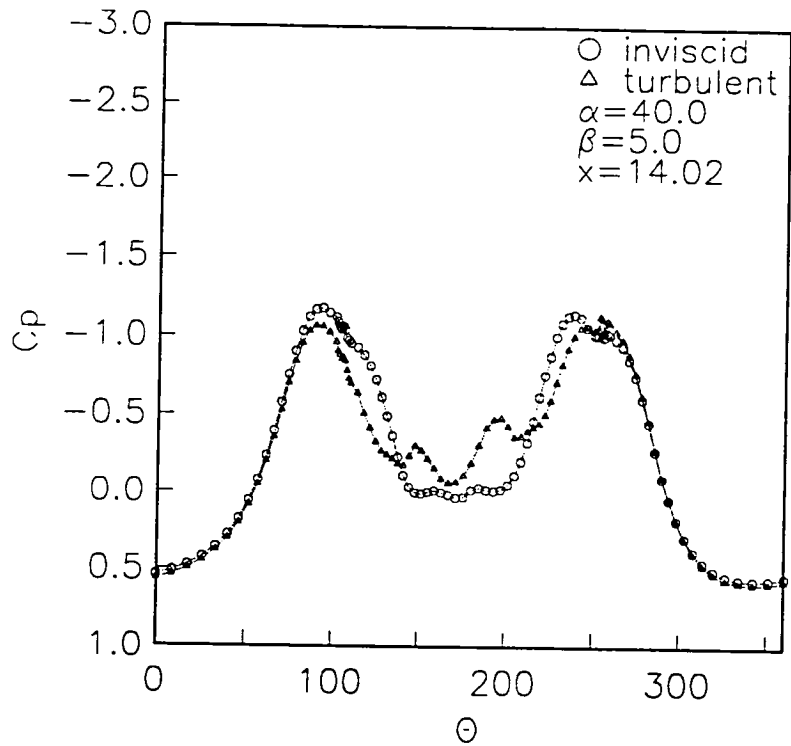
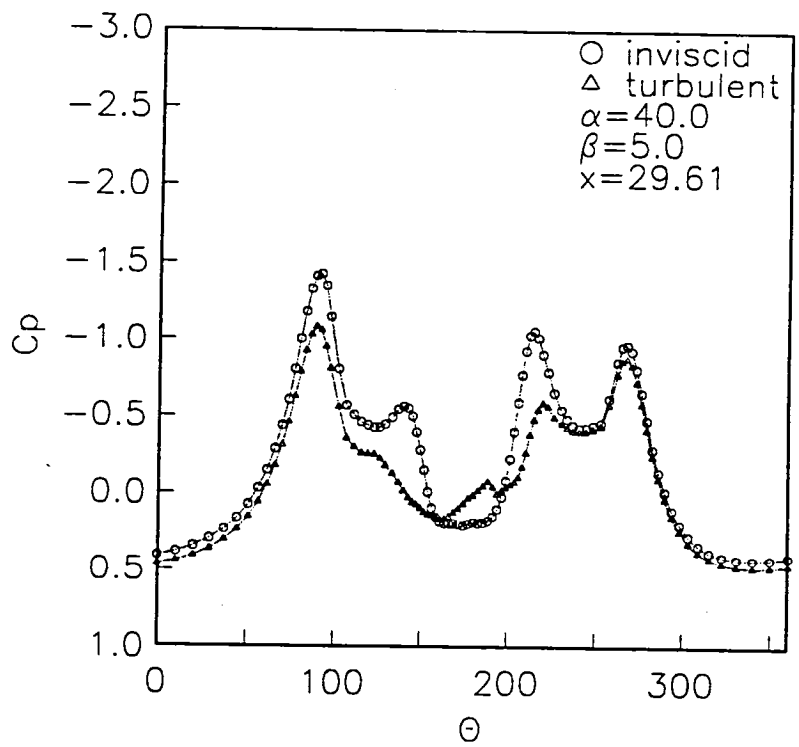


Figure 21(b). F5-A turbulent surface pressure distribution at $x = 29.61$ in.
 ($M=0.2, Re_c = 1.25 \cdot 10^6$)



(a) $x = 14.02$



(b) $x = 29.61$

Figure 22. F5-A inviscid vs turbulent surface pressure distribution at

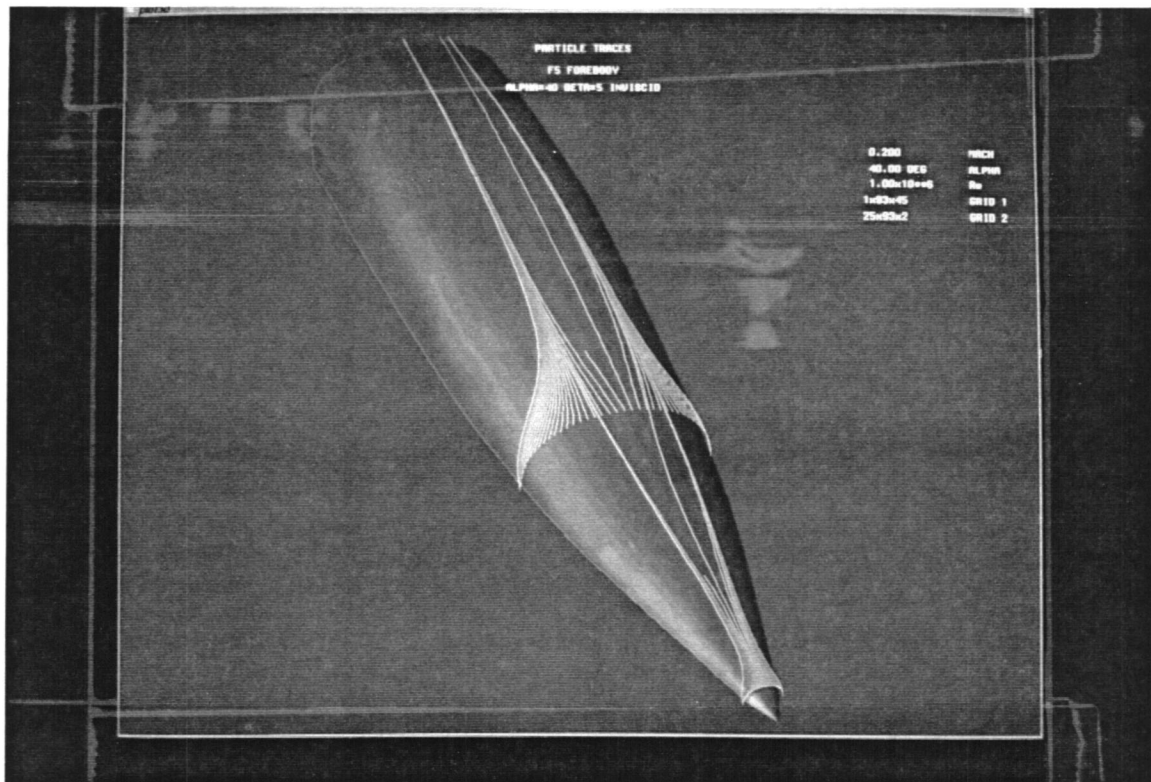


Figure 23(a). F5-A inviscid surface oil flow pattern $\alpha = 40^\circ$ and $\beta = 5^\circ$

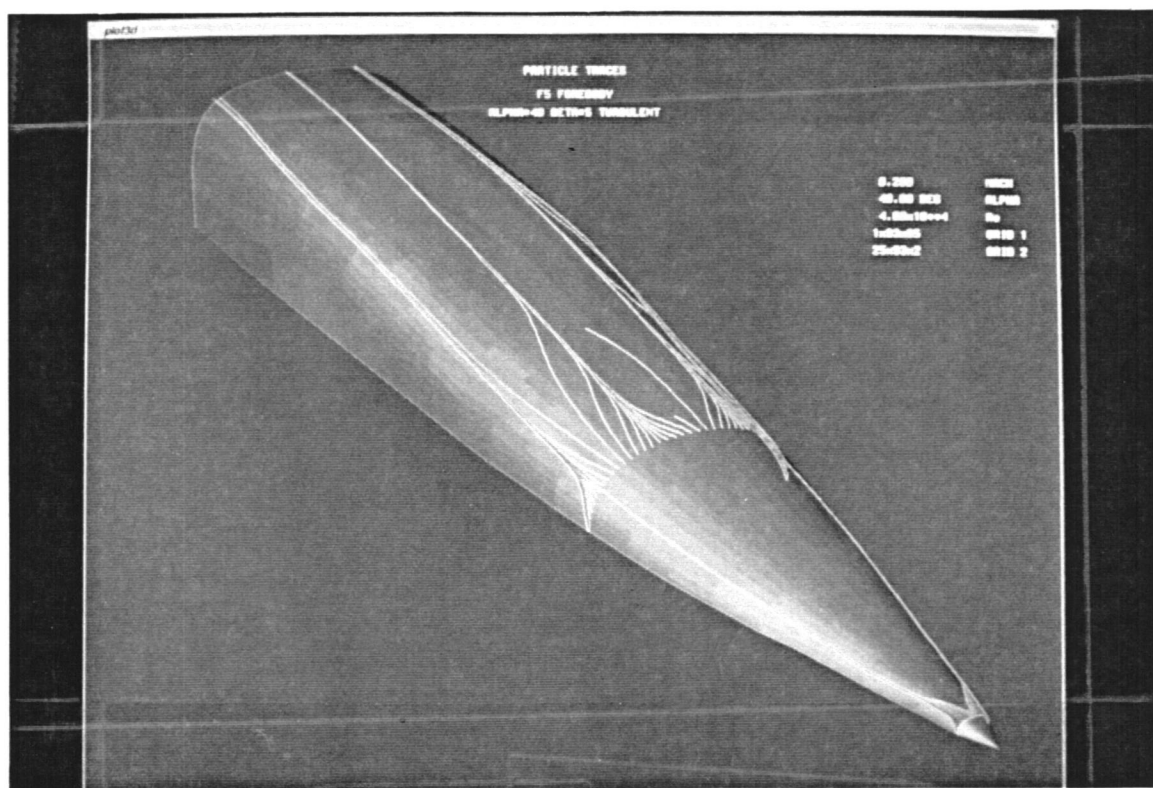


Figure 23(b). F5-A turbulent surface oil flow pattern $\alpha = 40^\circ$ and $\beta = 5^\circ$

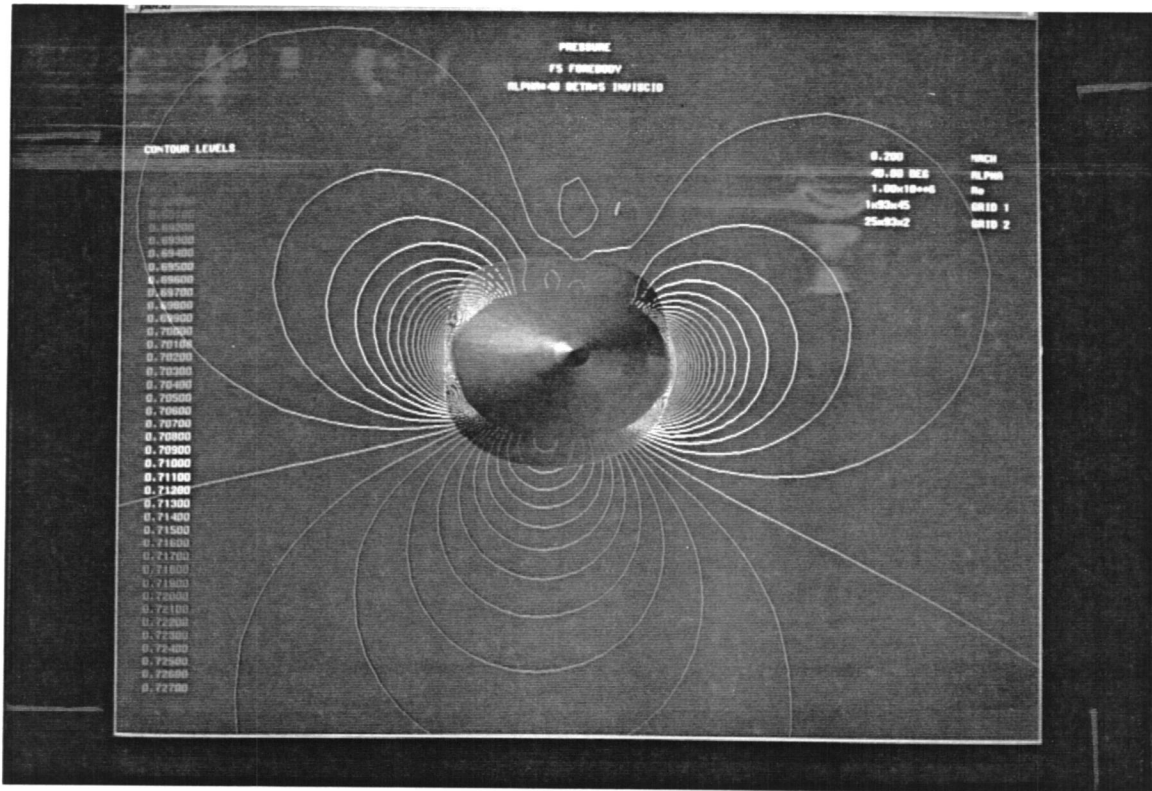


Figure 24. F5-A inviscid pressure contours at $x = 14.025$ in. ($\alpha = 40^\circ$ and $\beta = 5^\circ$)

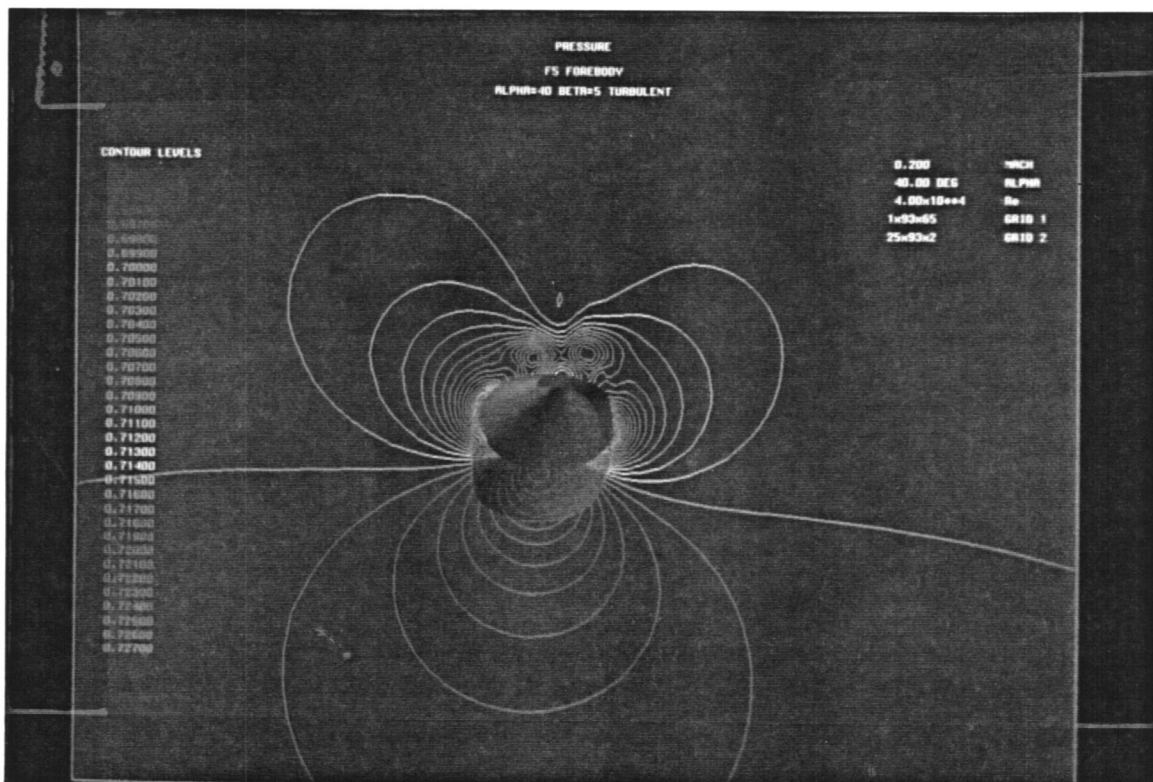


Figure 25. F5-A turbulent pressure contours at $x = 14.025$ in. ($\alpha = 40^\circ$ and $\beta = 5^\circ$)

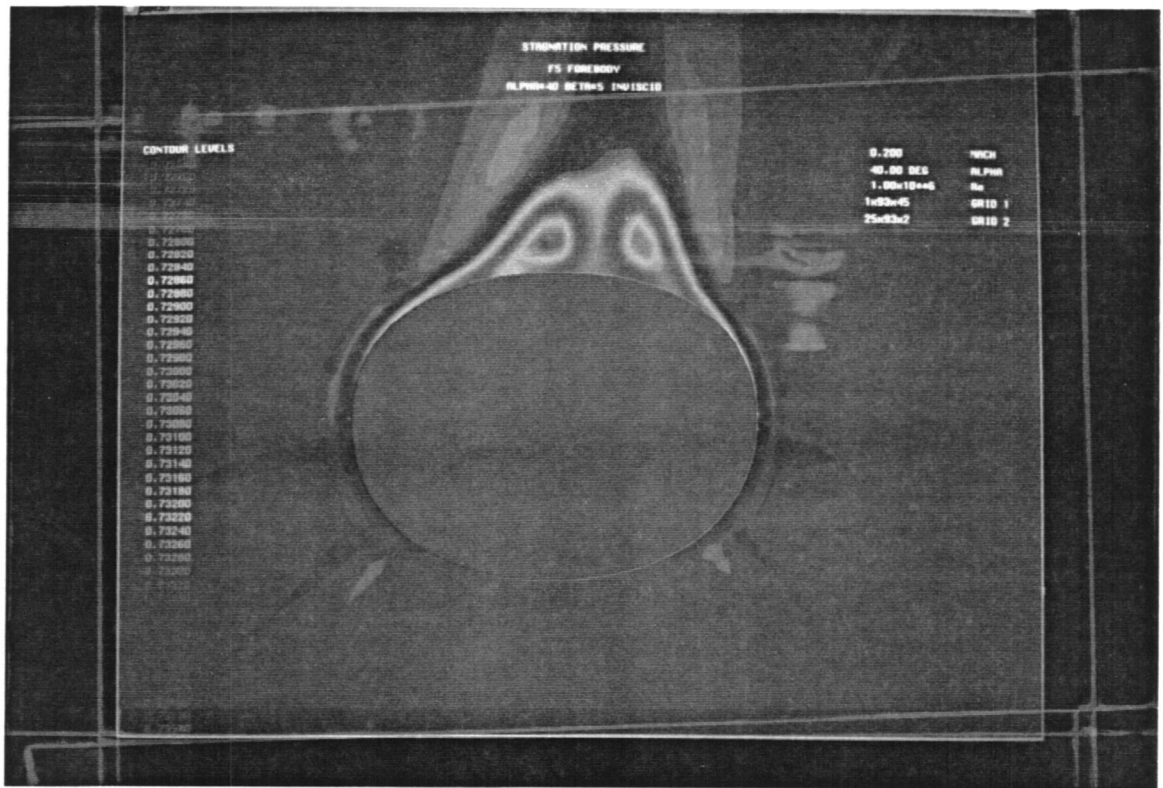


Figure 26. F5-A inviscid stagnation pressure at $x = 14.025$ in. ($\alpha = 40^\circ$ and $\beta = 5^\circ$)

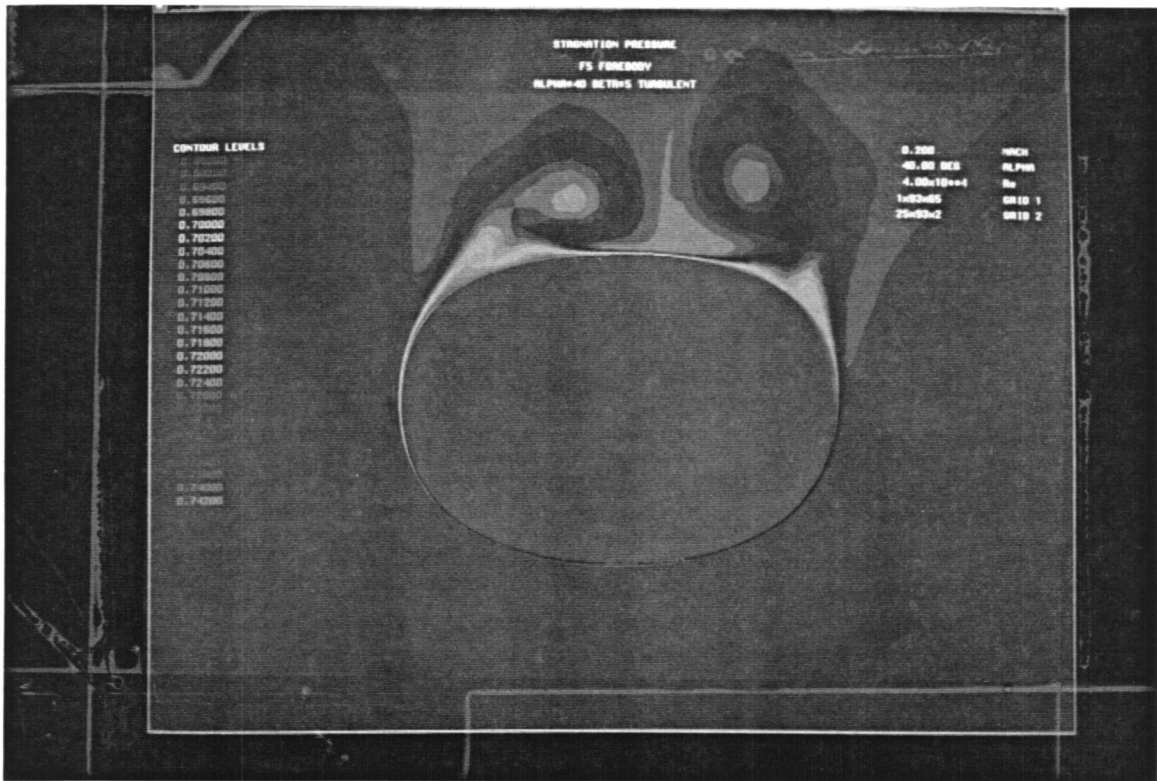


Figure 27. F5-A turbulent stagnation pressure at $x = 14.025$ in. ($\alpha = 40^\circ$ and $\beta = 5^\circ$)

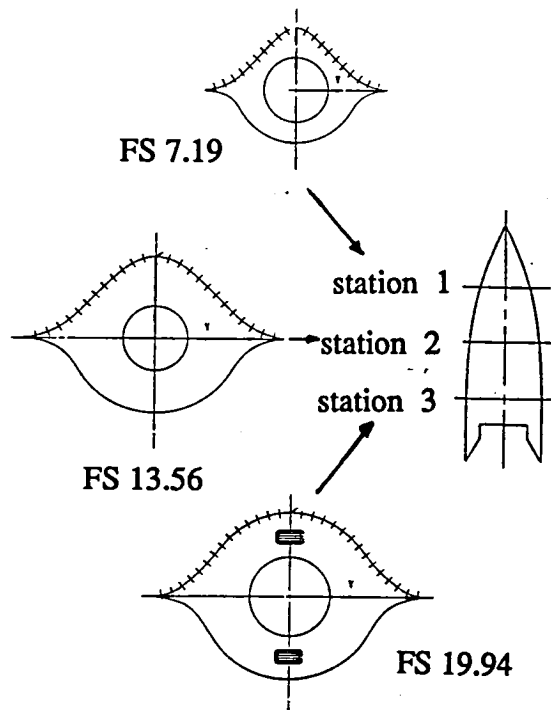
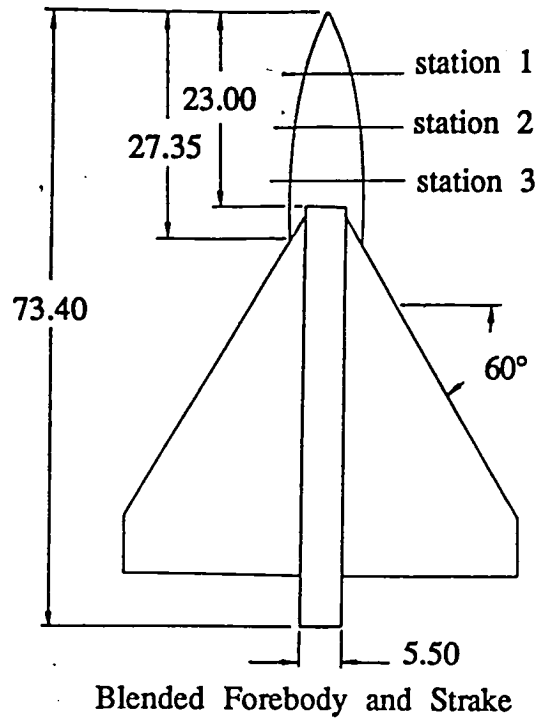


Figure 28. Details of the Erickson forebody wind tunnel model (ref. 7)

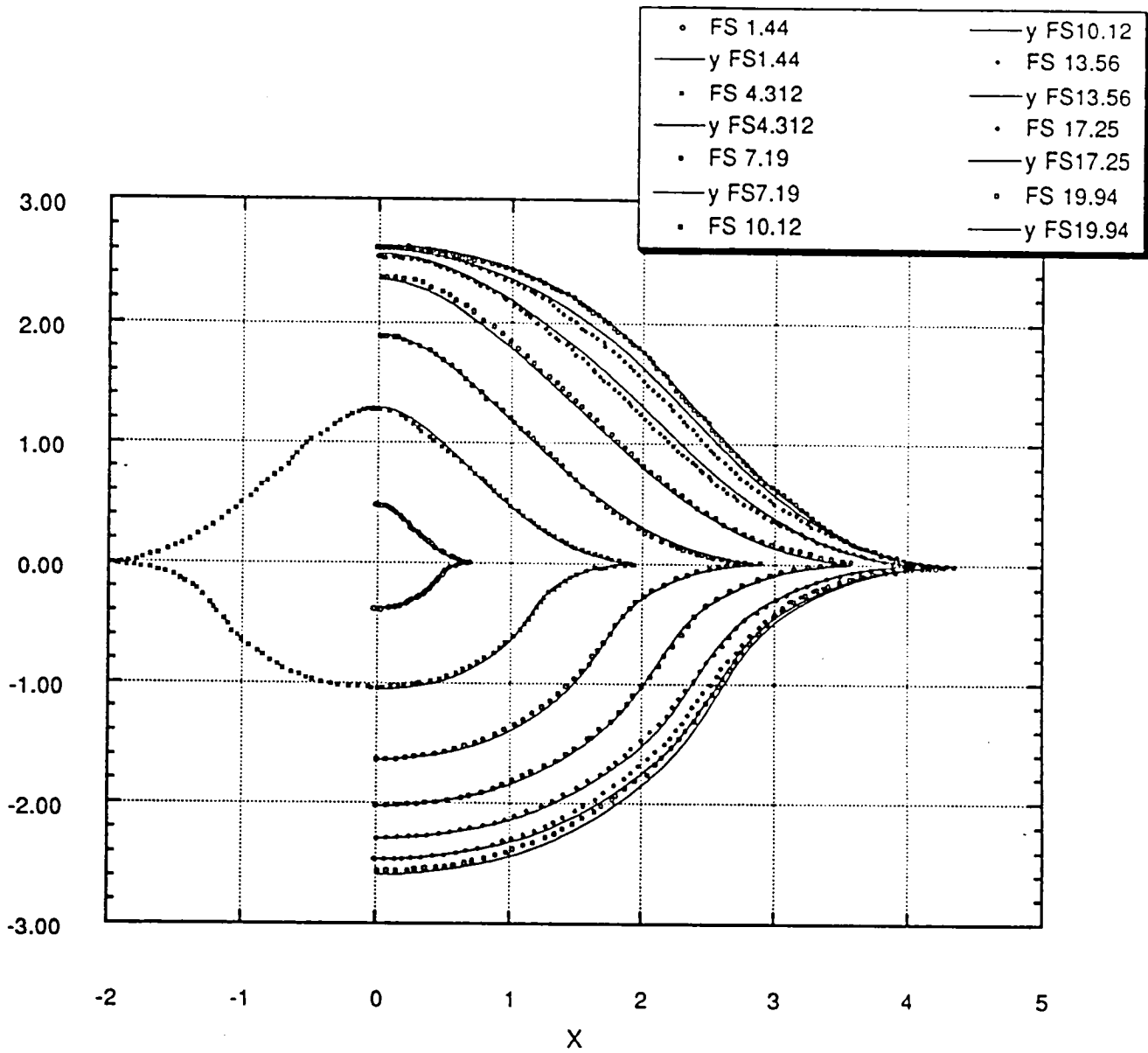
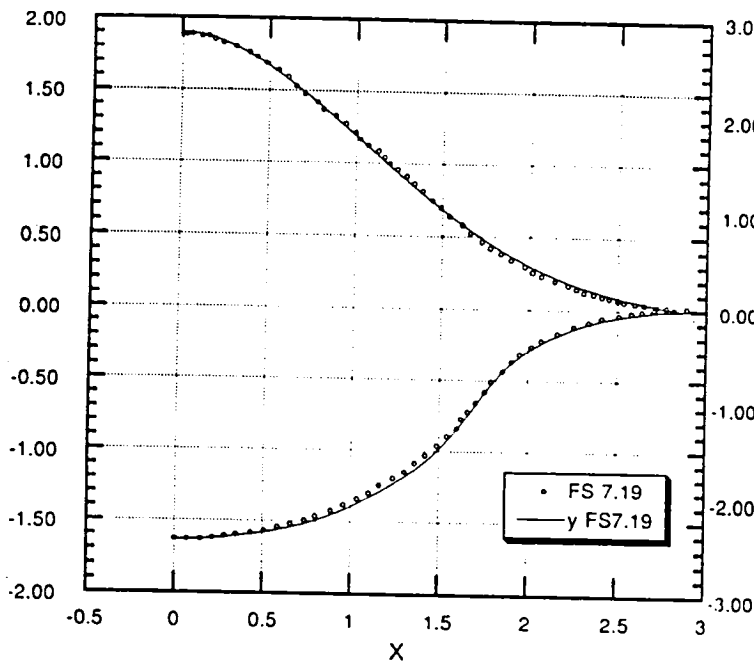
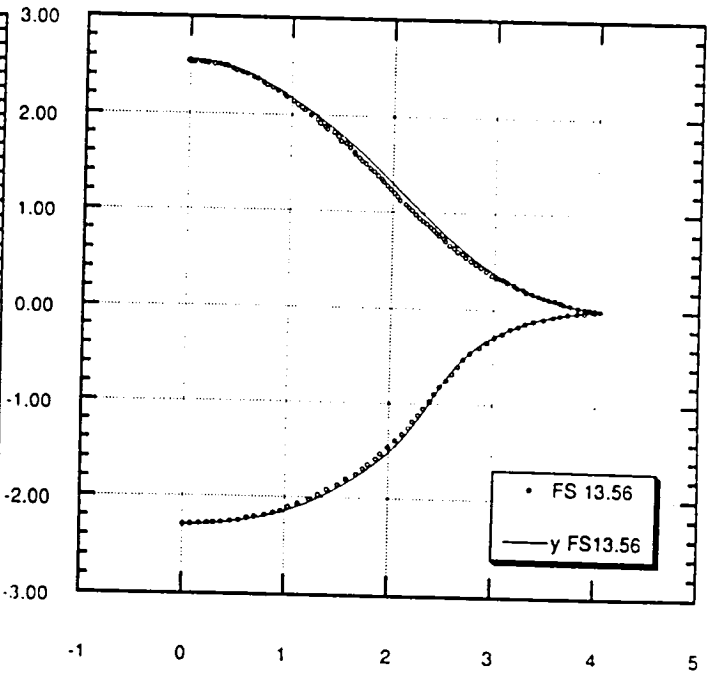


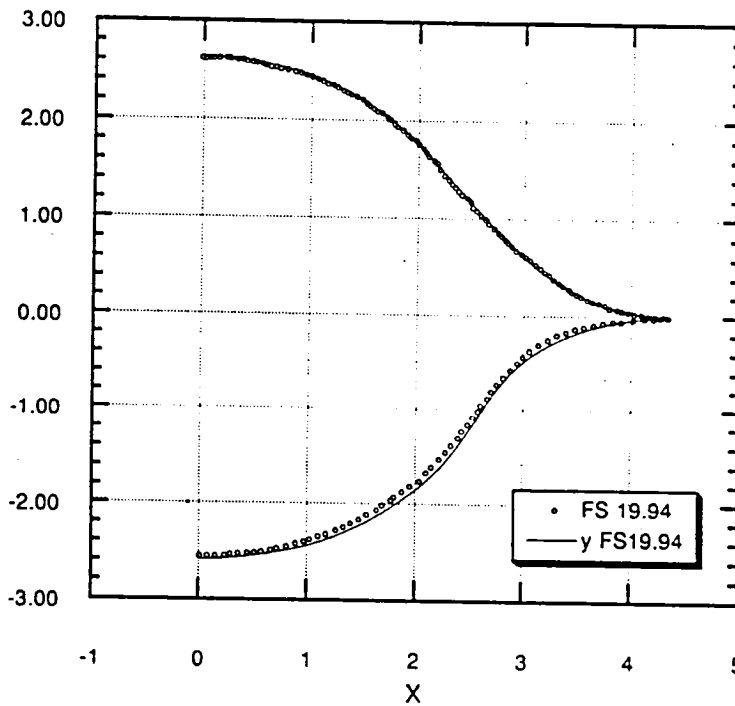
Figure 29. Comparison of digitized ordinates and smooth math model for the Erickson forebody for the full range of stations.



FS 7.19



FS 13.56



FS 19.94

Figure 30. Comparison of digitized ordinates and smooth math model for the Erickson forebody.

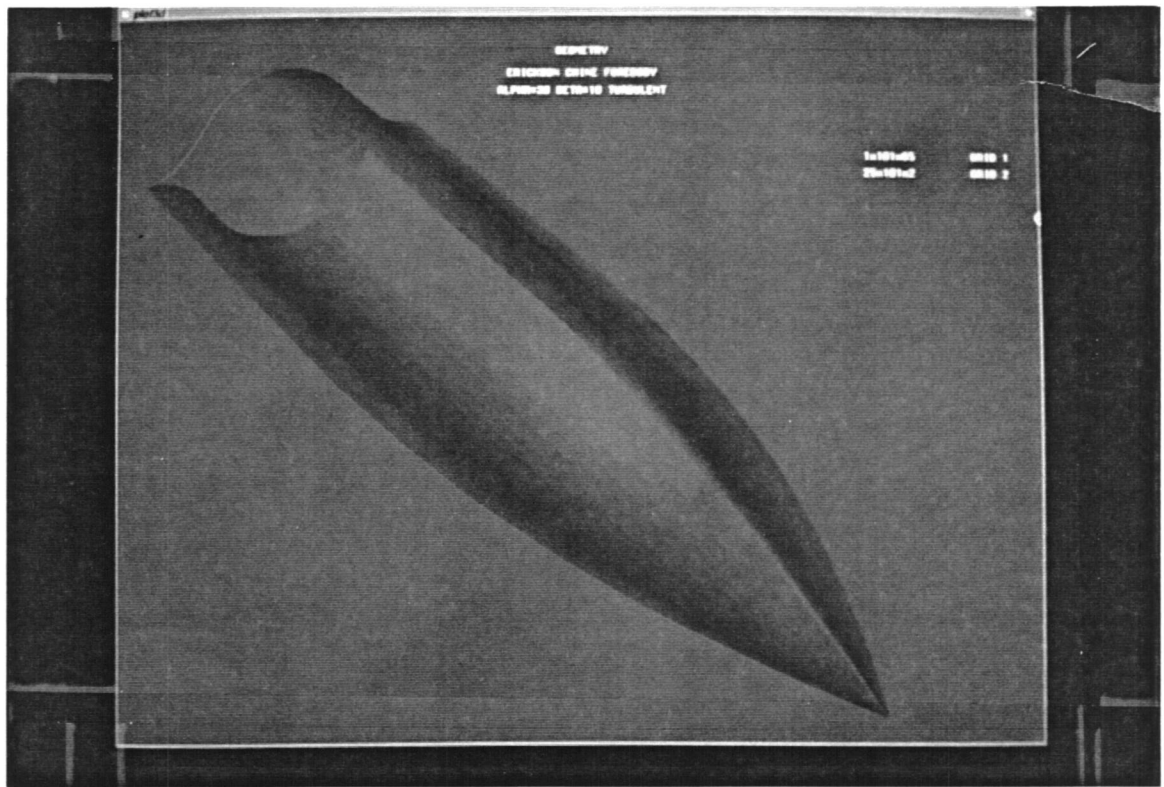
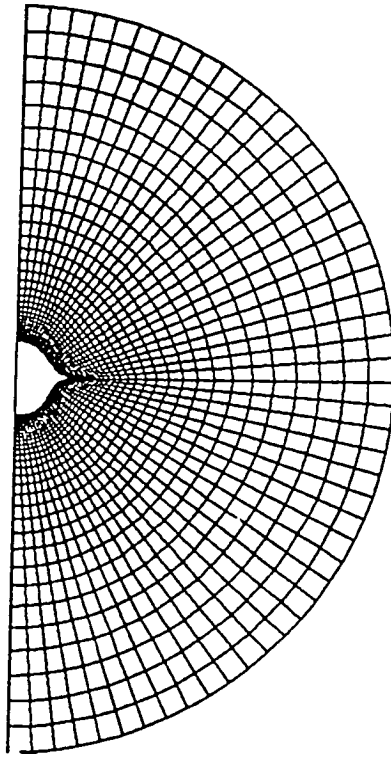
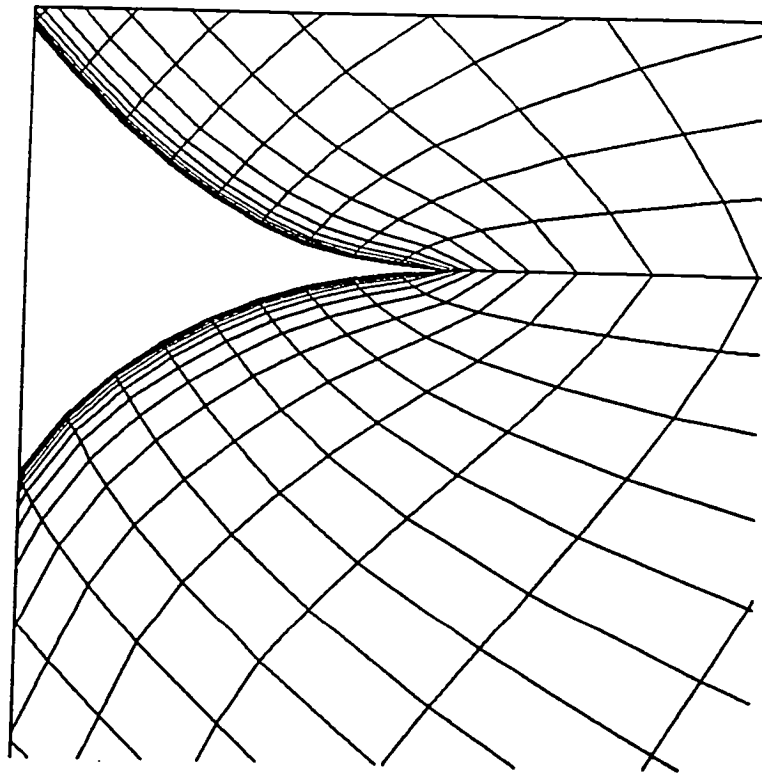


Figure 31. Erickson forebody computational model (PLOT3D)



(a) cross sectional grid



(b) closeup near surface

Figure 32. Erickson forebody cross sectional grid at $x = 30.00$ in.

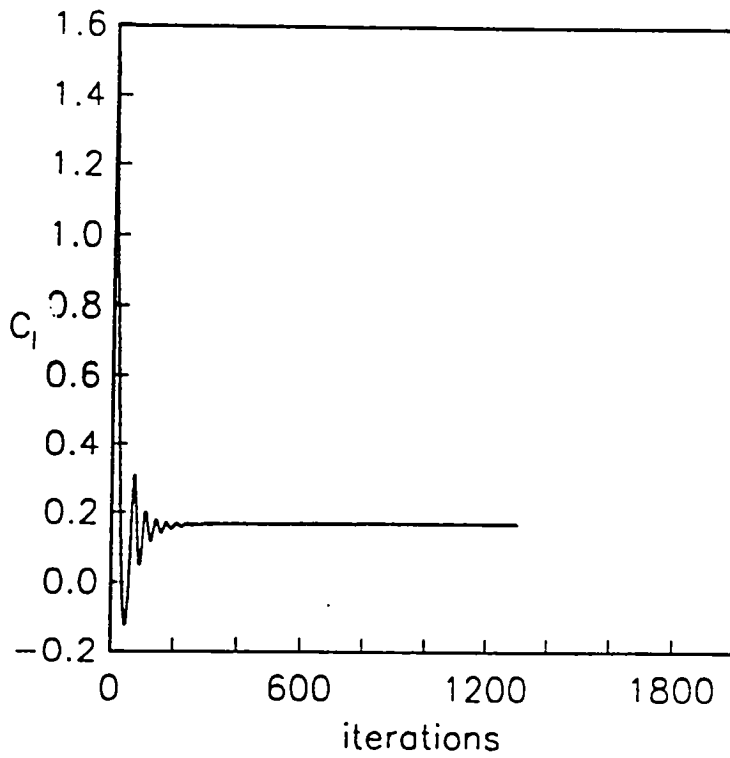
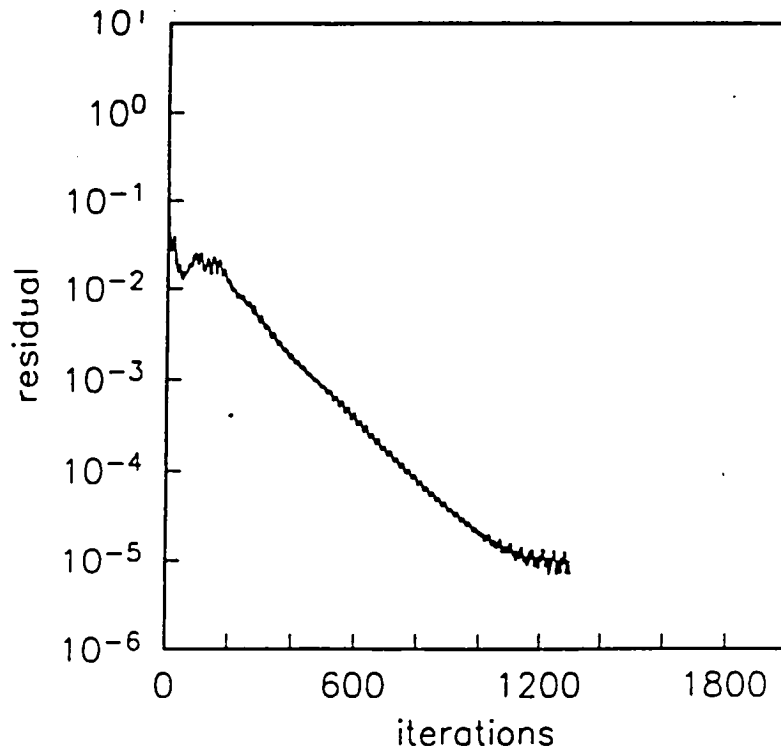


Figure 33. Erickson forebody convergence history (inviscid)
 $\alpha = 30^\circ$ and $\beta = 10^\circ$

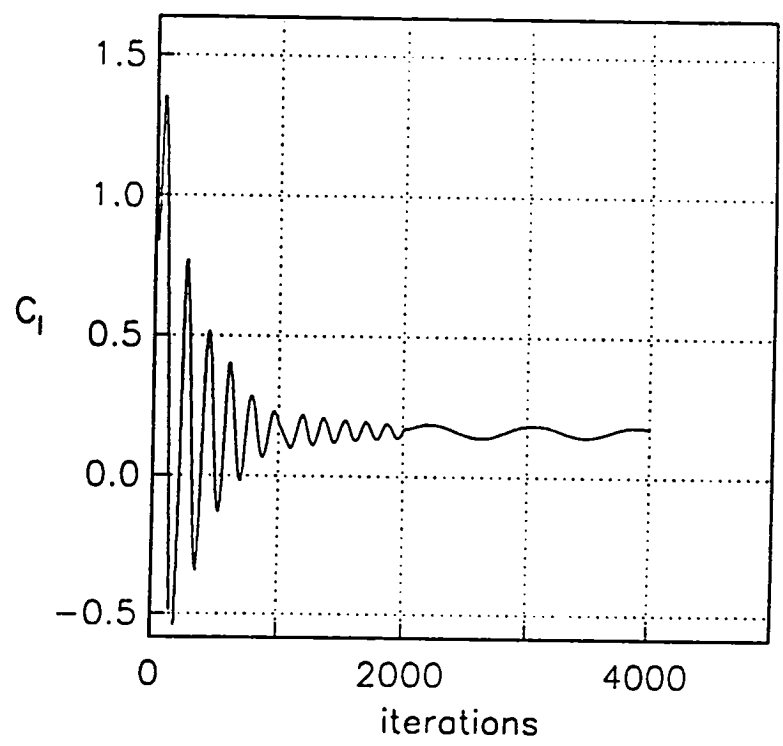
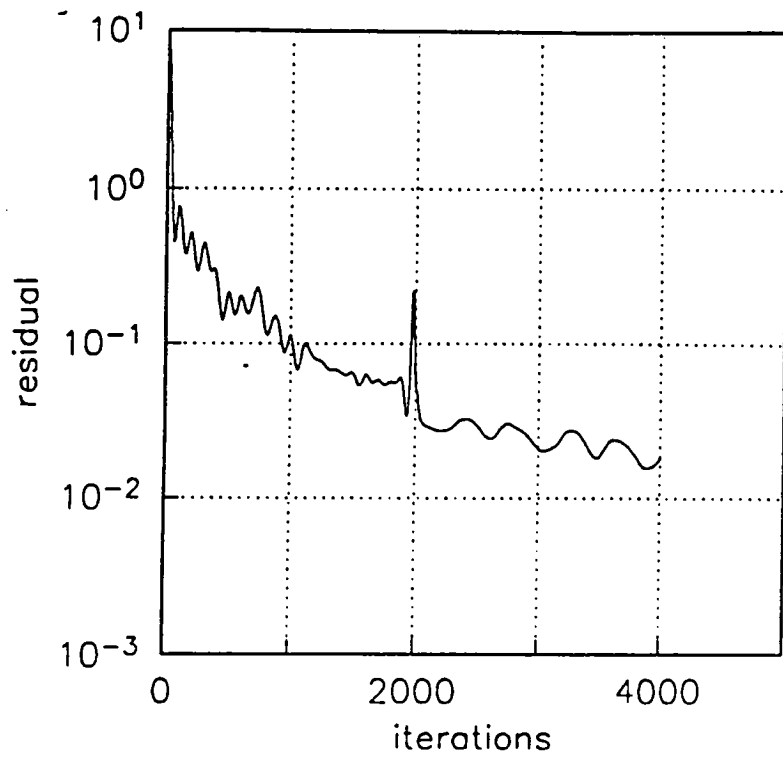


Figure 34. Erickson forebody convergence history (turbulent) $\alpha = 30^\circ$ and $\beta = 10^\circ$

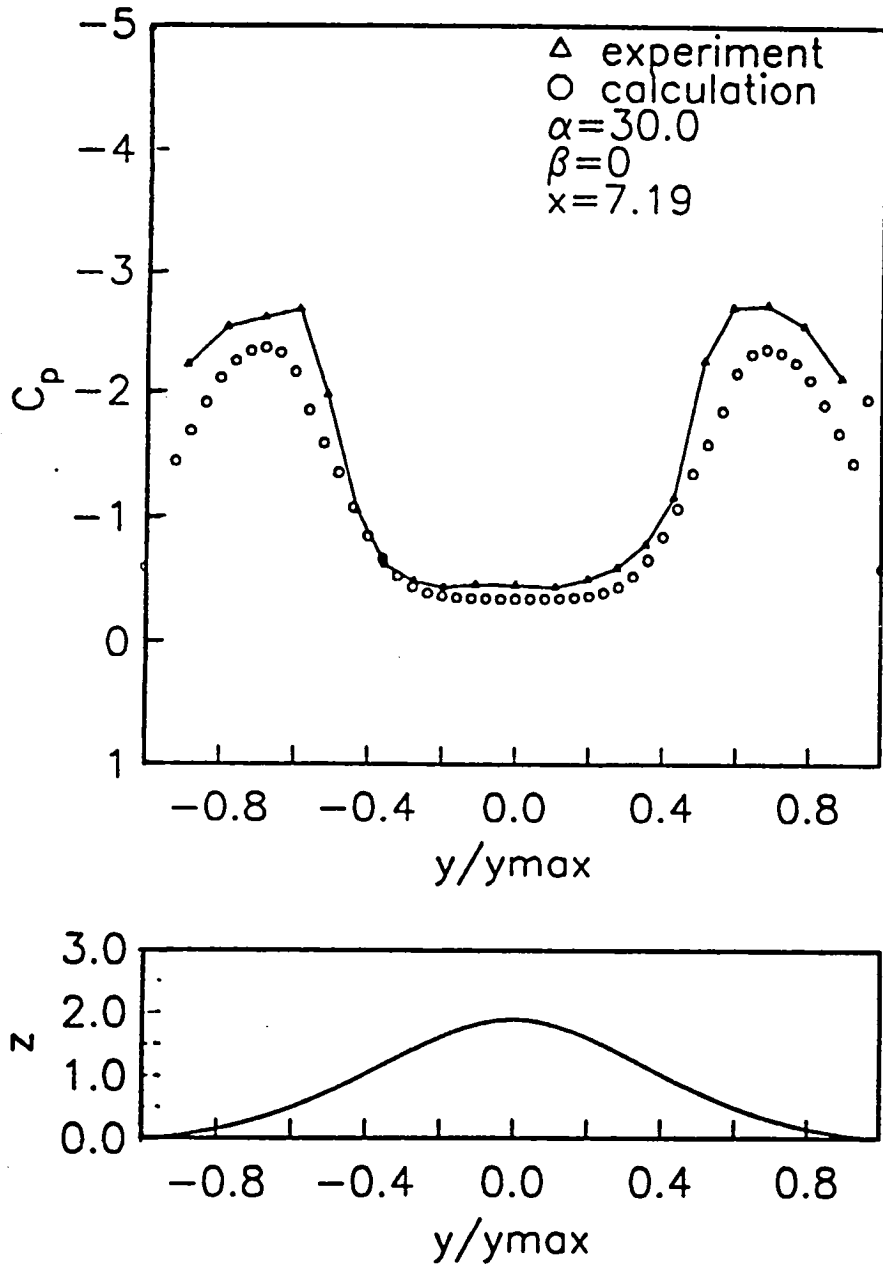


Figure 35(a). Erickson forebody inviscid surface pressure distribution at $x = 7.19$ in.
 ($M = 0.2$)

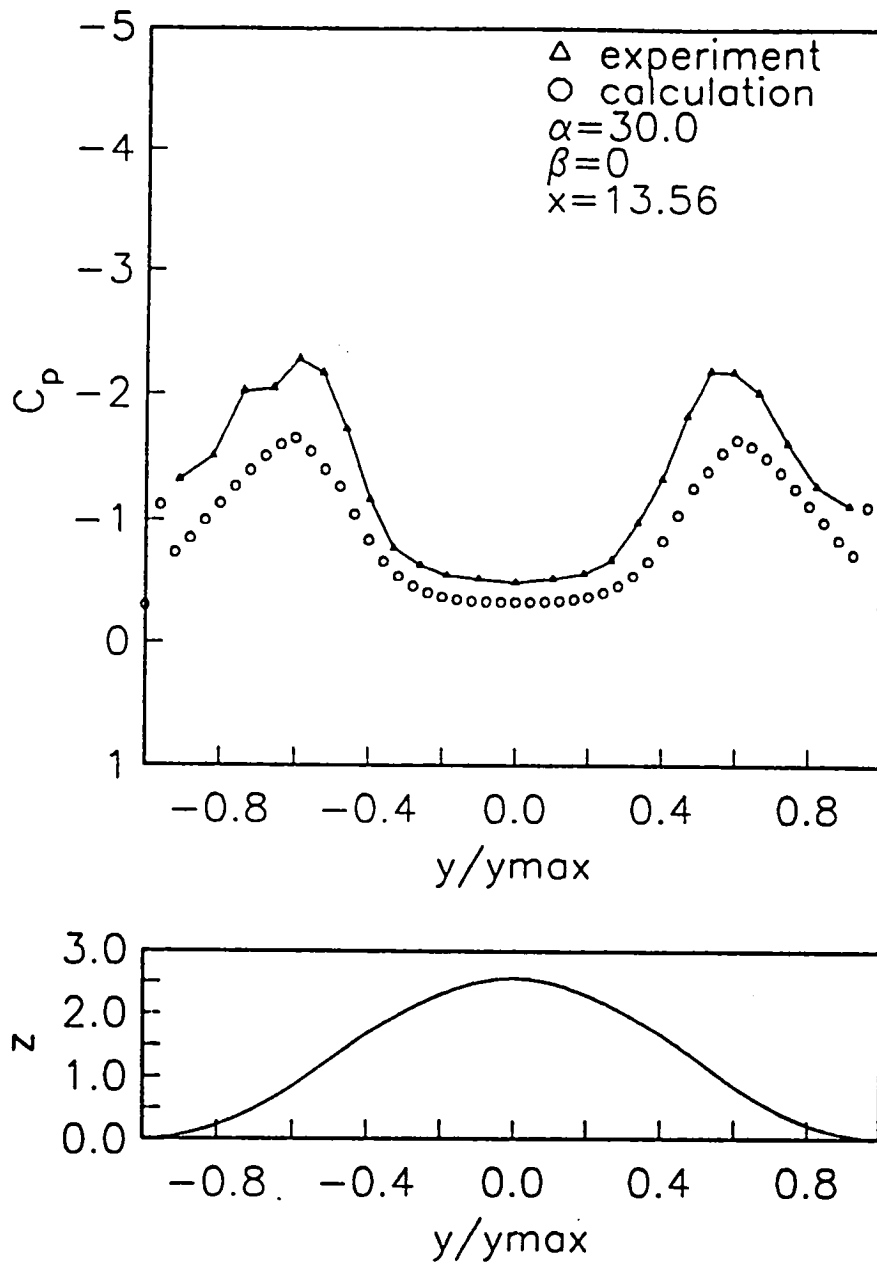


Figure 35(b). Erickson forebody inviscid surface pressure distribution at $x = 13.56$ in. ($M = 0.2$)

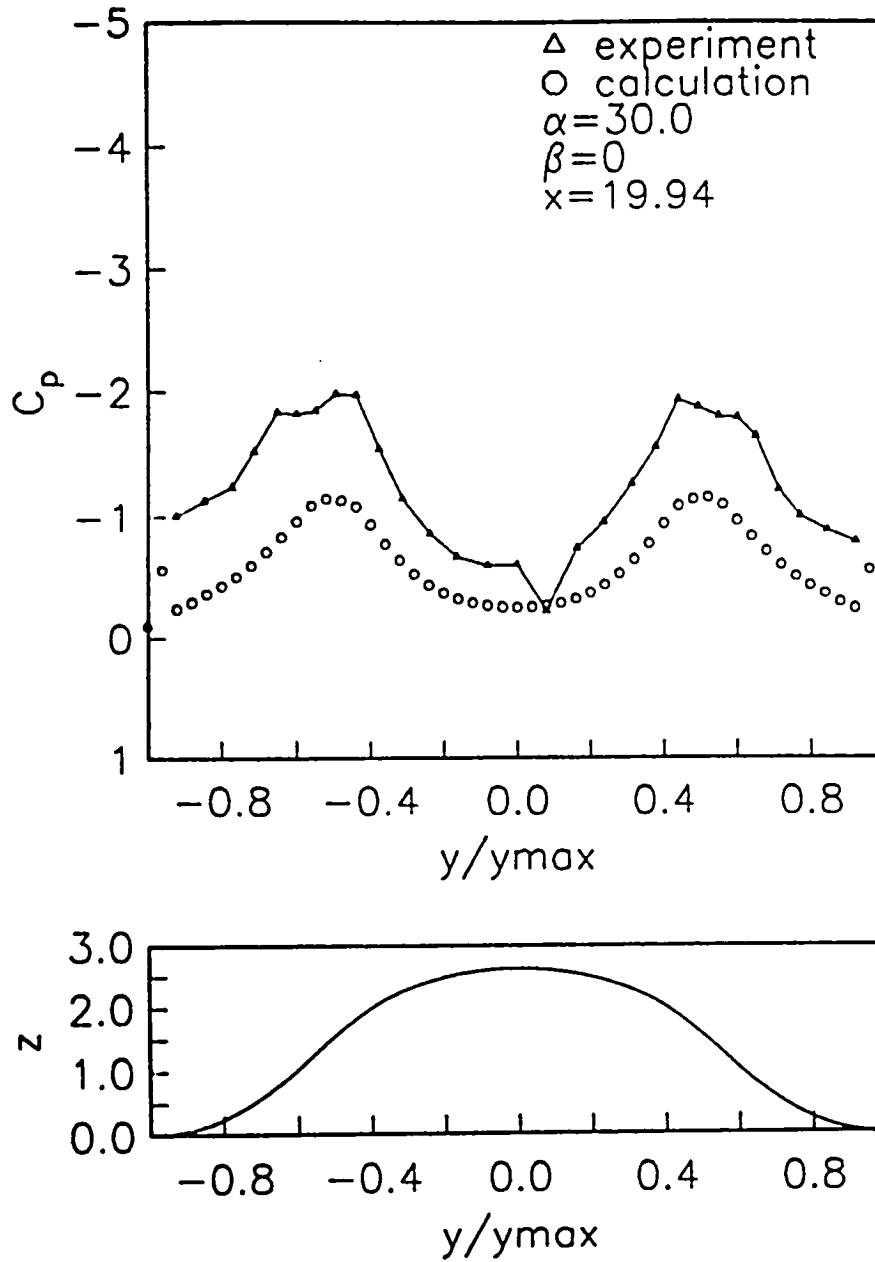


Figure 35(c). Erickson forebody inviscid surface pressure distribution at $x = 19.94$ in. ($M = 0.2$)

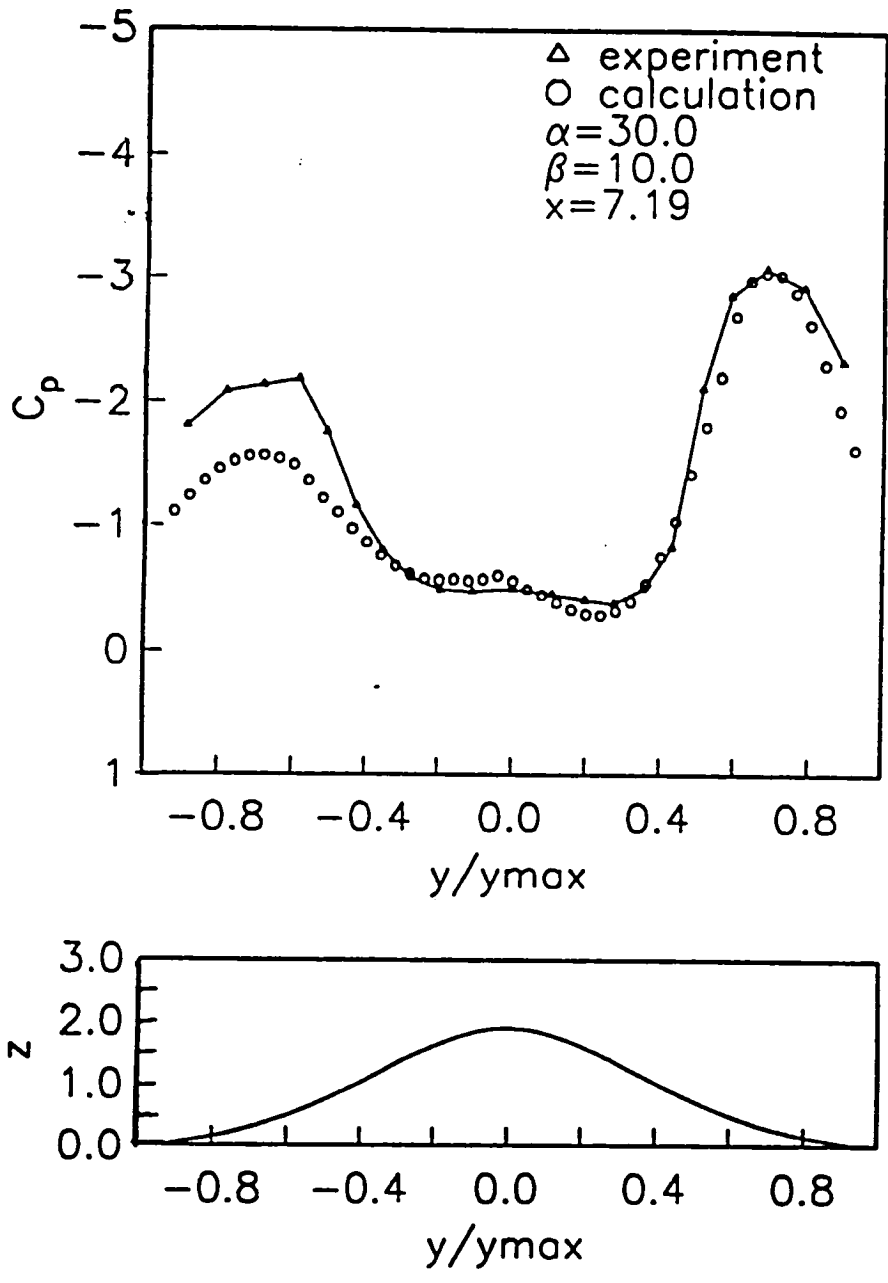


Figure 36(a). Erickson forebody inviscid surface pressure distribution at $x = 7.19$ in. ($M = 0.2$)

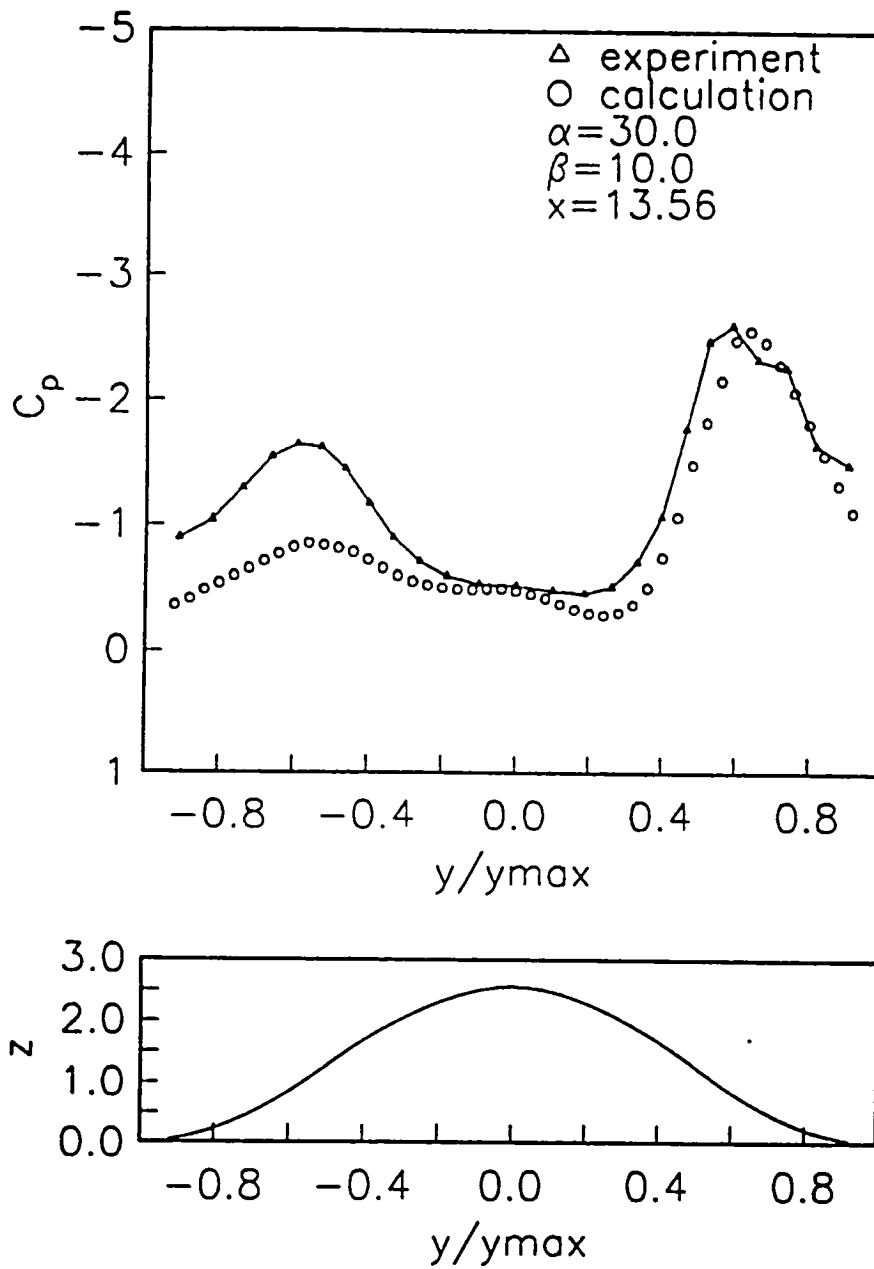


Figure 36(b). Erickson forebody inviscid surface pressure distribution at $x = 13.56$ in. ($M = 0.2$)

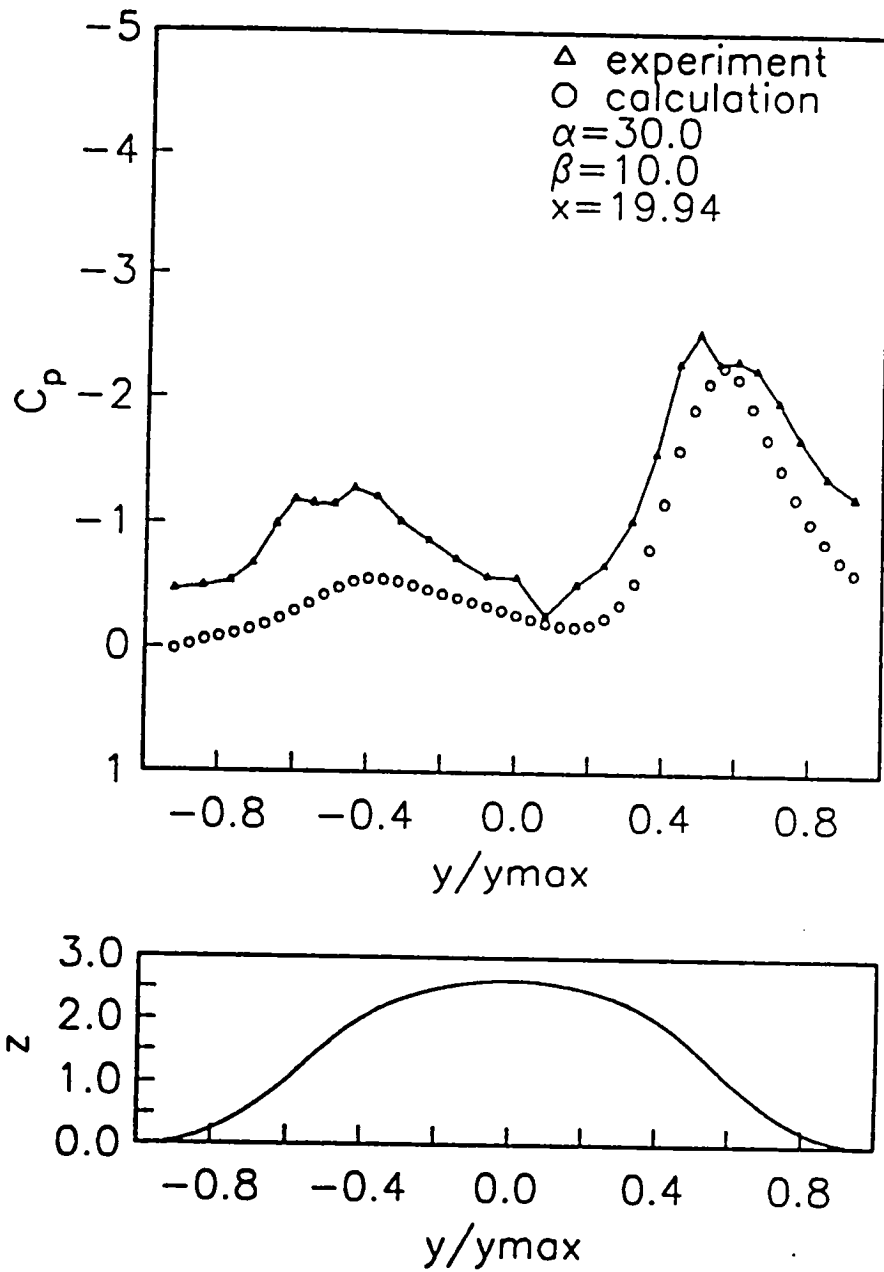


Figure 36(c). Erickson forebody inviscid surface pressure distribution at $x = 19.94$ in. ($M = 0.2$)

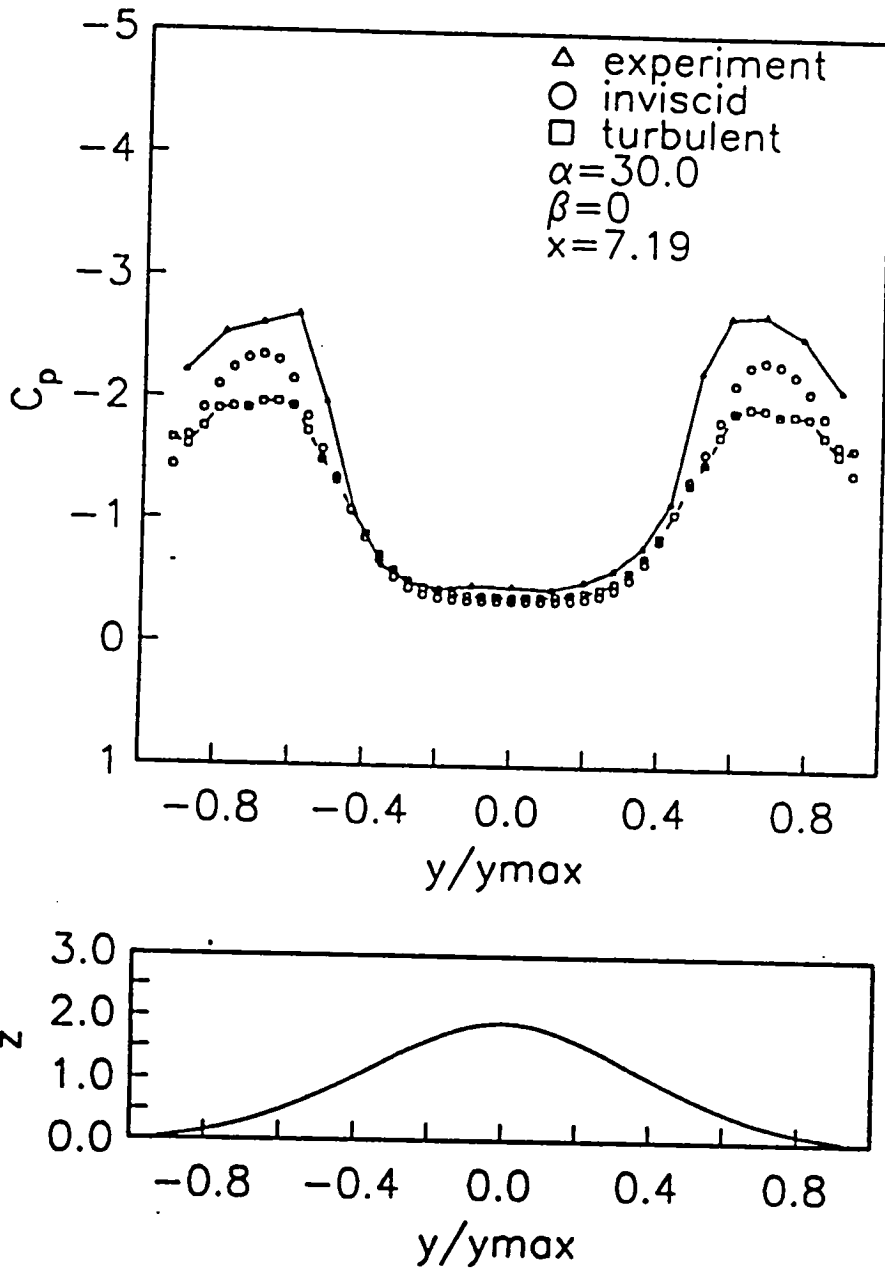


Figure 37(a). Erickson forebody inviscid vs turbulent surface pressures at $x = 7.19$ in.
 ($M = 0.2$, $Re_c = 1.02 \cdot 10^6$)

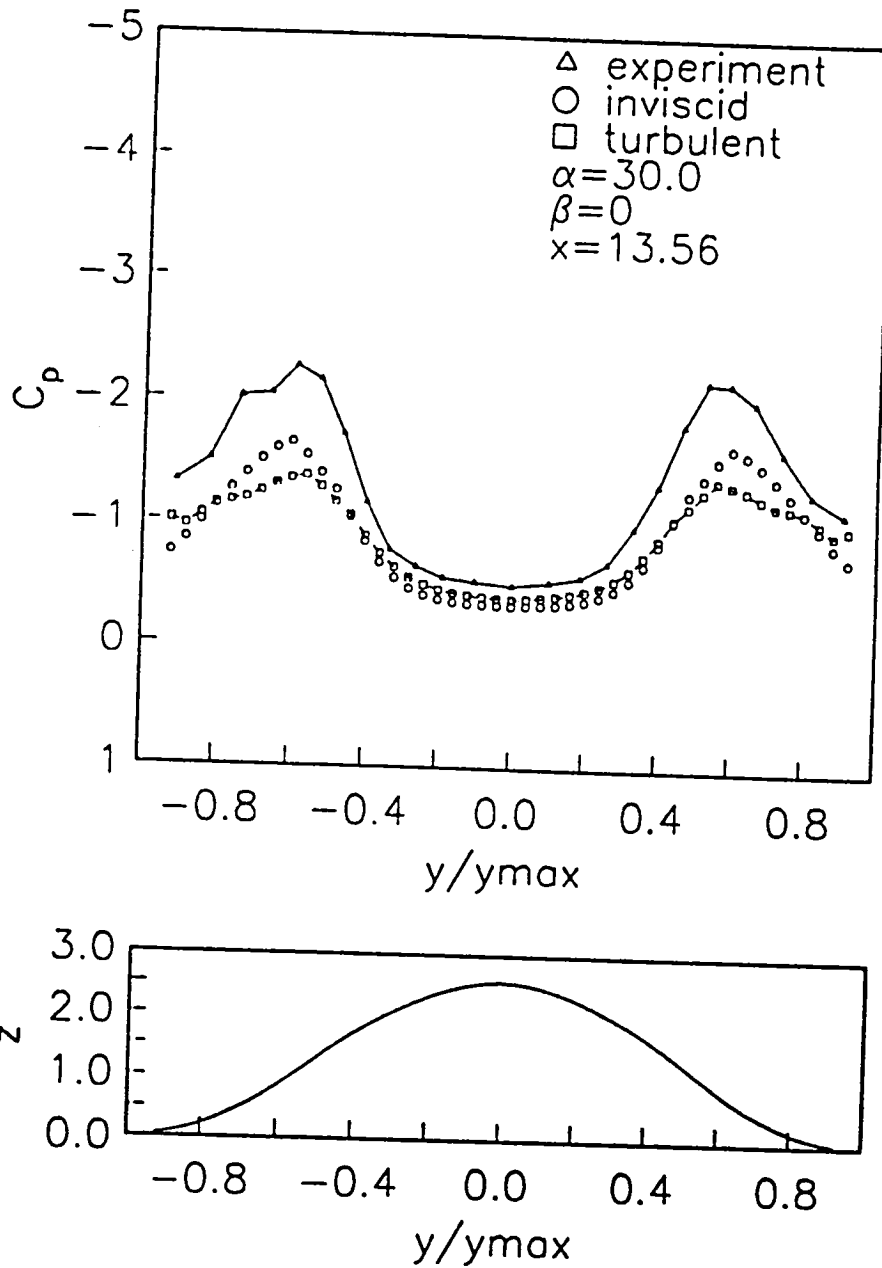


Figure 37(b). Erickson forebody inviscid vs turbulent surface pressures at $x = 13.56$ in. ($M = 0.2$, $Re_c = 1.02 \cdot 10^6$)

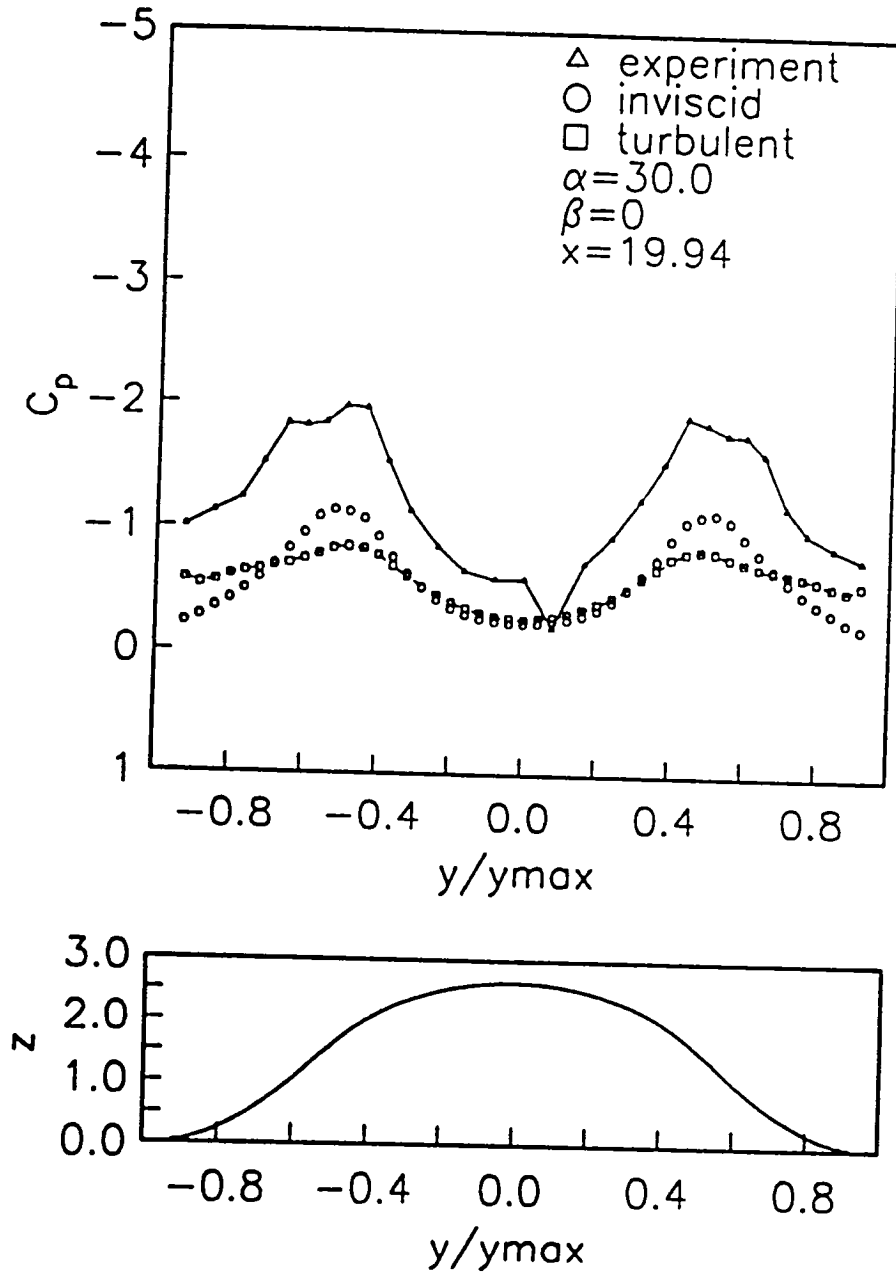


Figure 37(c). Erickson forebody inviscid vs turbulent surface pressures at $x = 19.94$ in.
 ($M = 0.2, Re_c = 1.02 \cdot 10^6$)

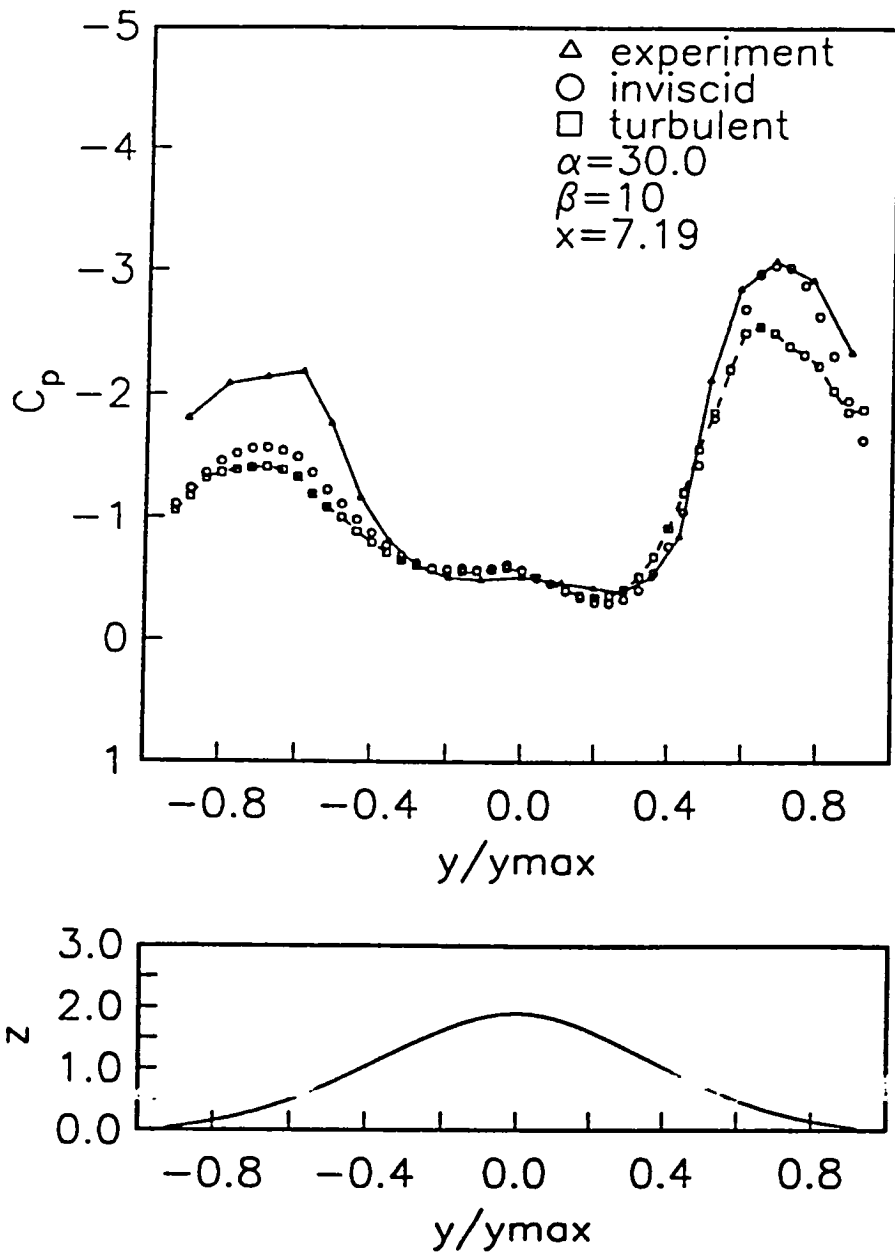


Figure 38(a). Erickson forebody inviscid vs turbulent surface pressures at $x = 7.19$ in.
 ($M = 0.2$, $Re_c = 1.02 \cdot 10^6$)

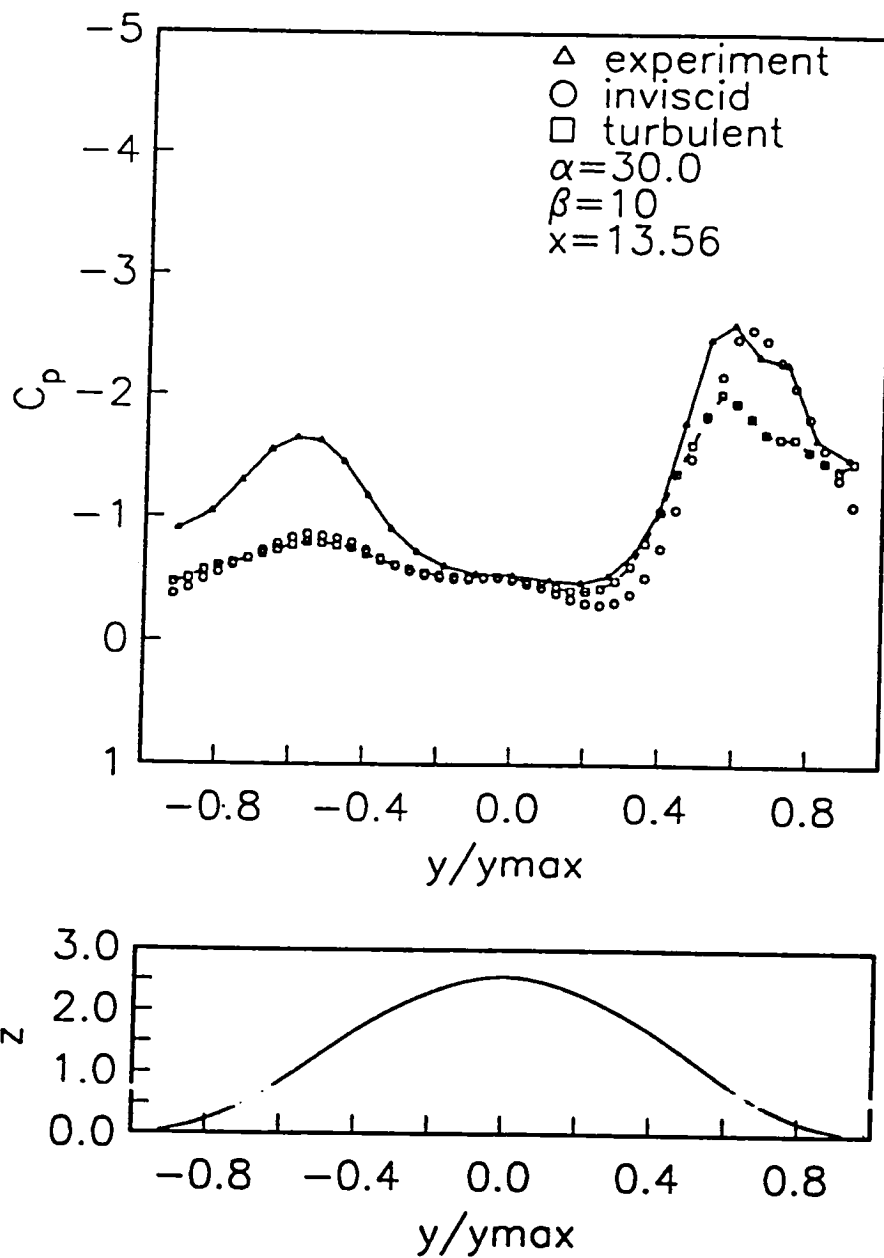


Figure 38(b). Erickson forebody inviscid vs turbulent surface pressures at $x = 13.56$ in.
 ($M = 0.2, Re_c = 1.02 \cdot 10^6$)

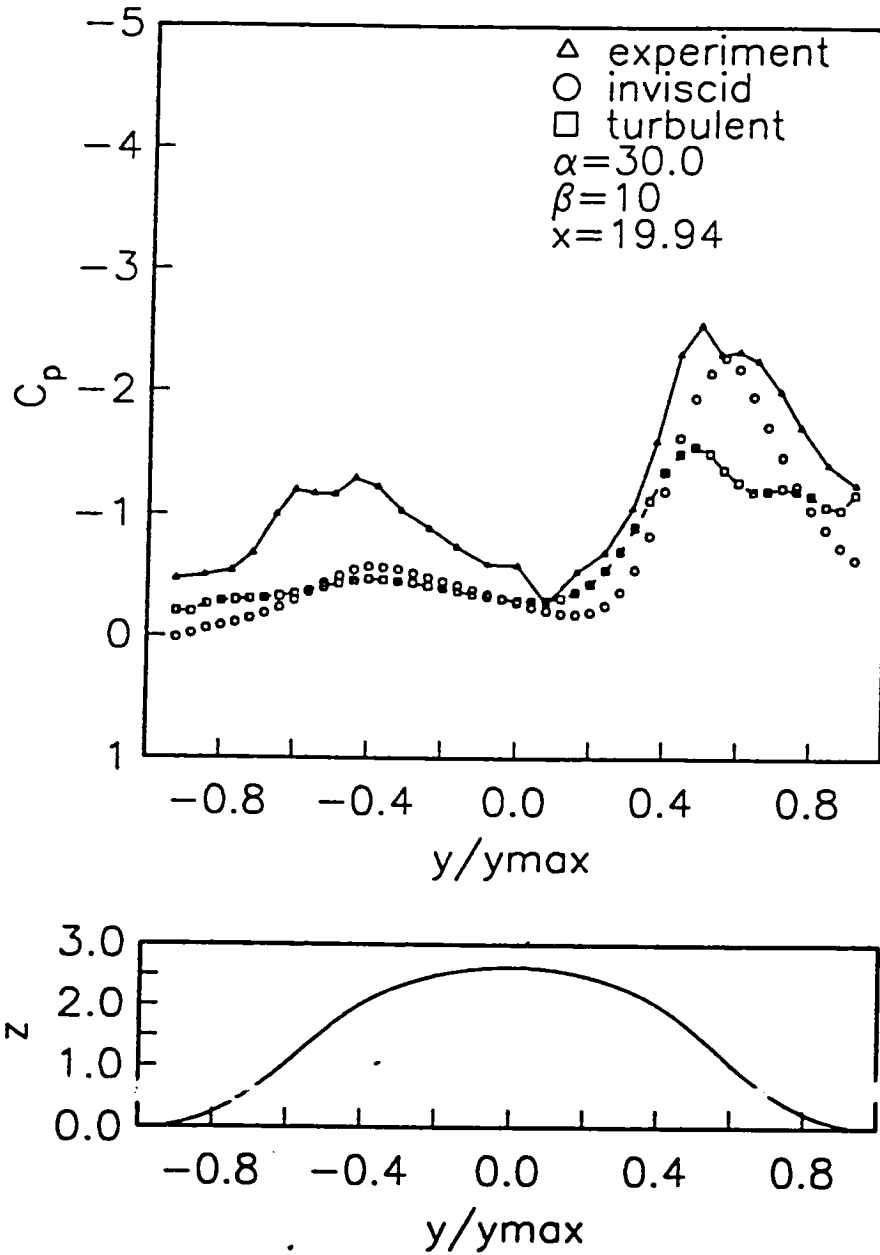
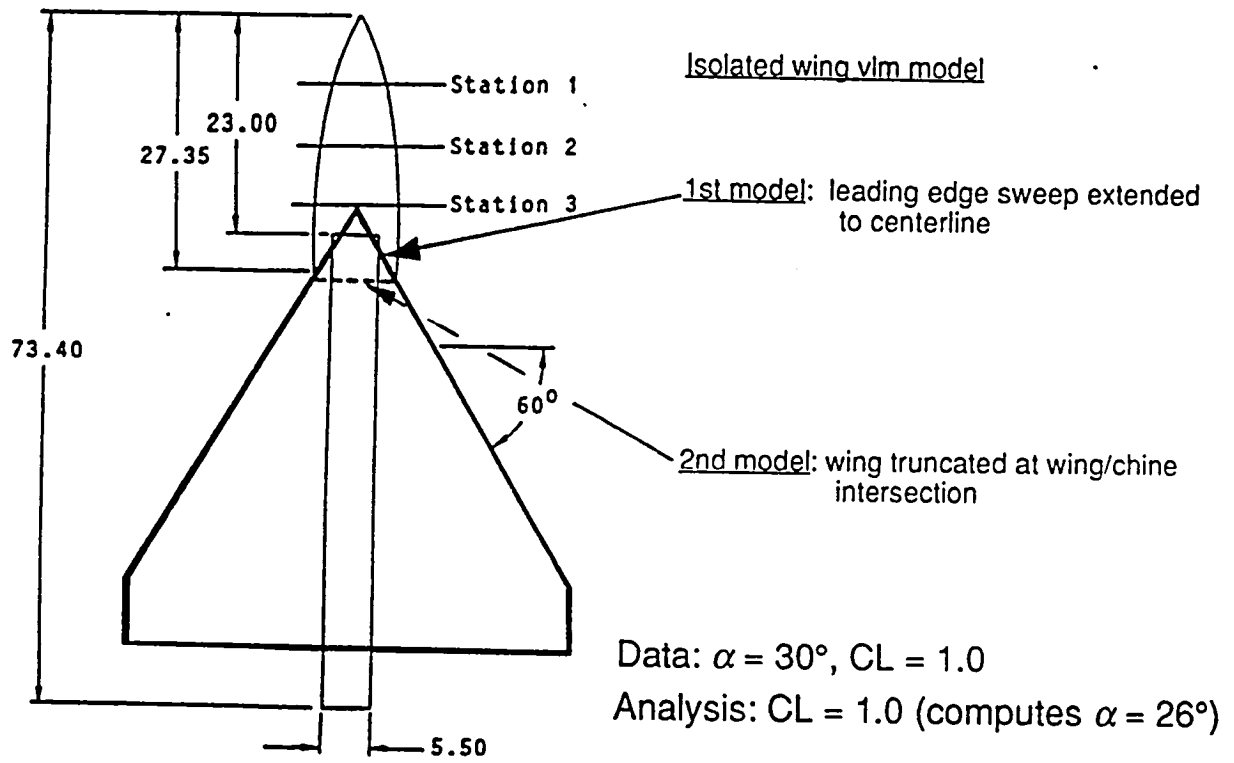


Figure 38(c). Erickson forebody inviscid vs turbulent surface pressures at $x = 19.94$ in.
 ($M = 0.2$, $Re_c = 1.02 \cdot 10^6$)

Erickson Chine Forebody



(from Erickson and Brandon, AIAA 85-1798)

Figure 39. Erickson forebody with isolated wing VLM model

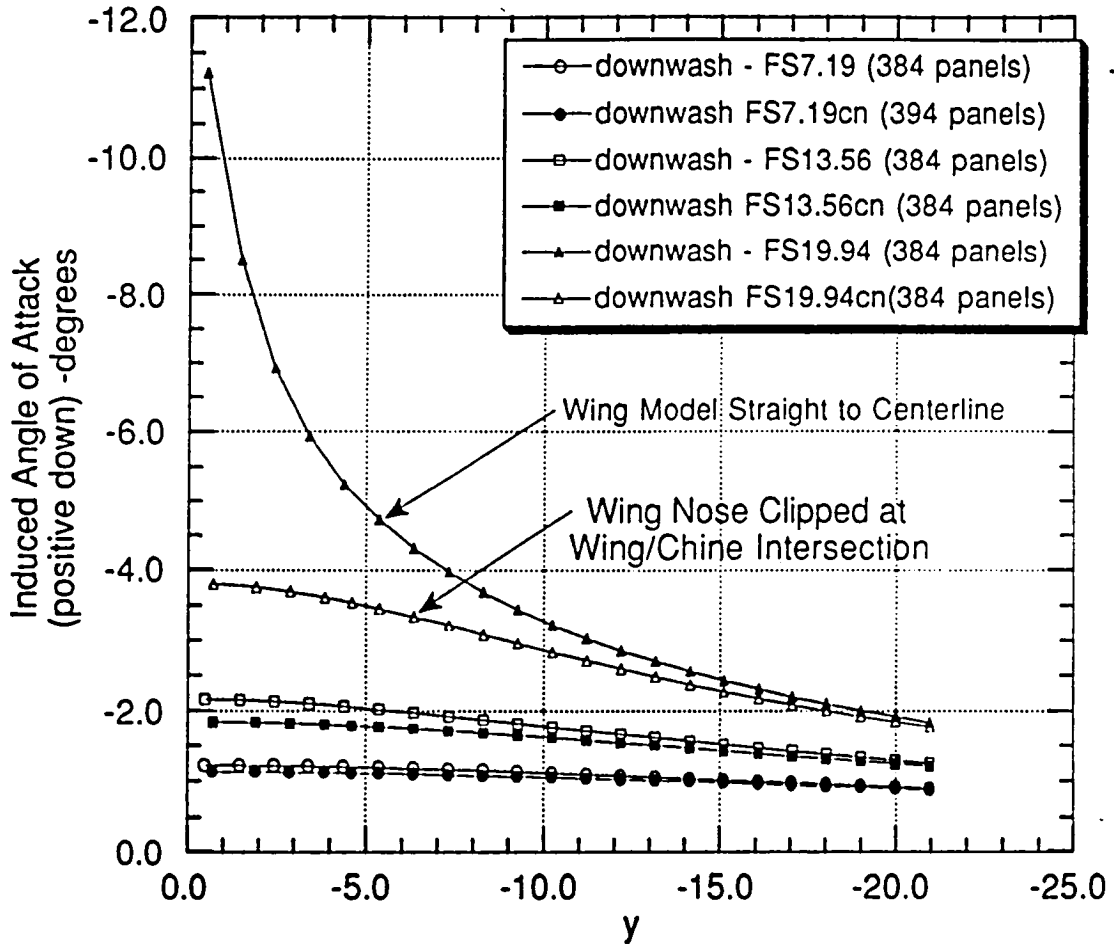


Figure 40. Wing induced flowfield at Erickson forebody pressure stations.

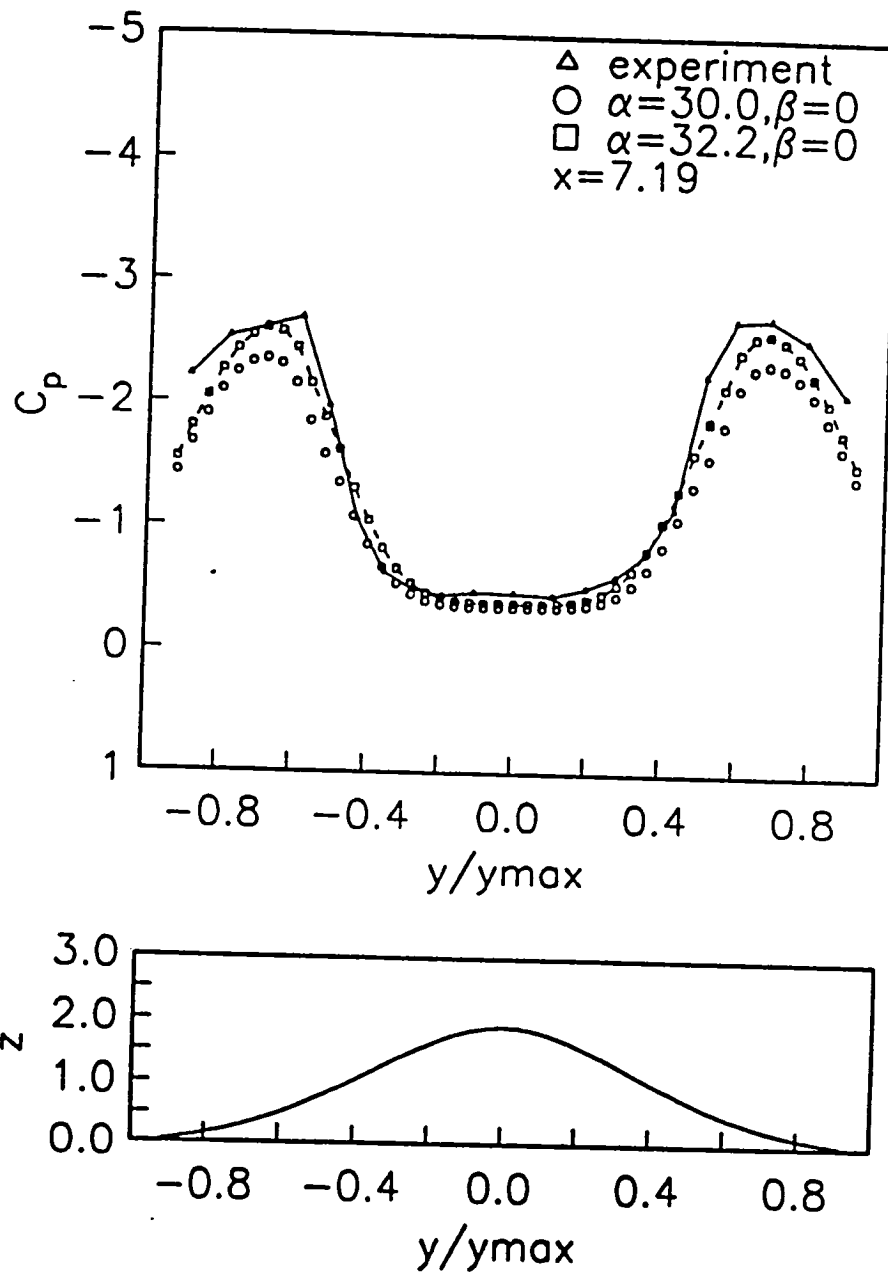


Figure 41(a). Erickson forebody inviscid surface pressures at $x = 7.19$ in.
 ($\alpha = 32.2^\circ$ and $\beta = 0^\circ$)

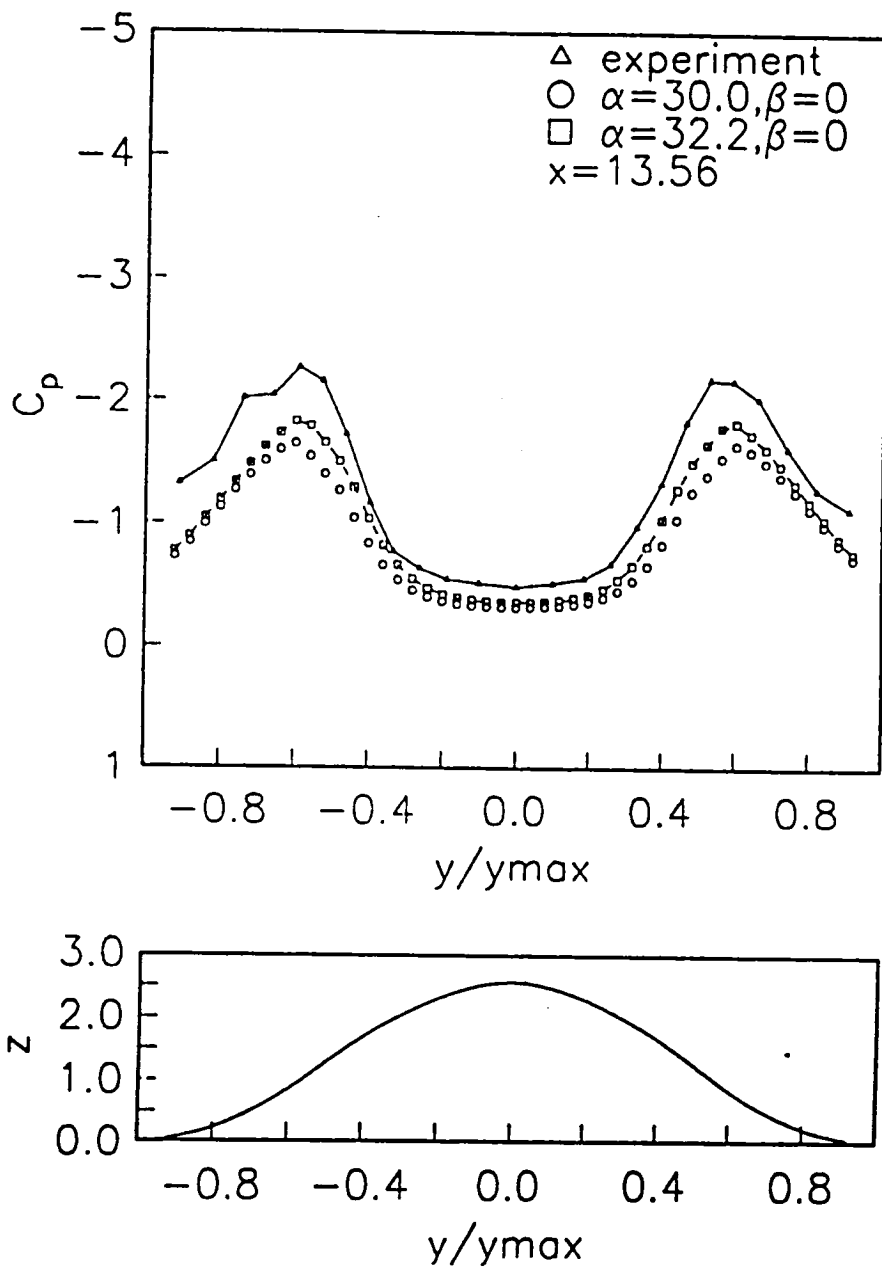


Figure 41(b). Erickson forebody inviscid surface pressures at $x = 13.56$ in.
 ($\alpha = 32.2^\circ$ and $\beta = 0^\circ$)

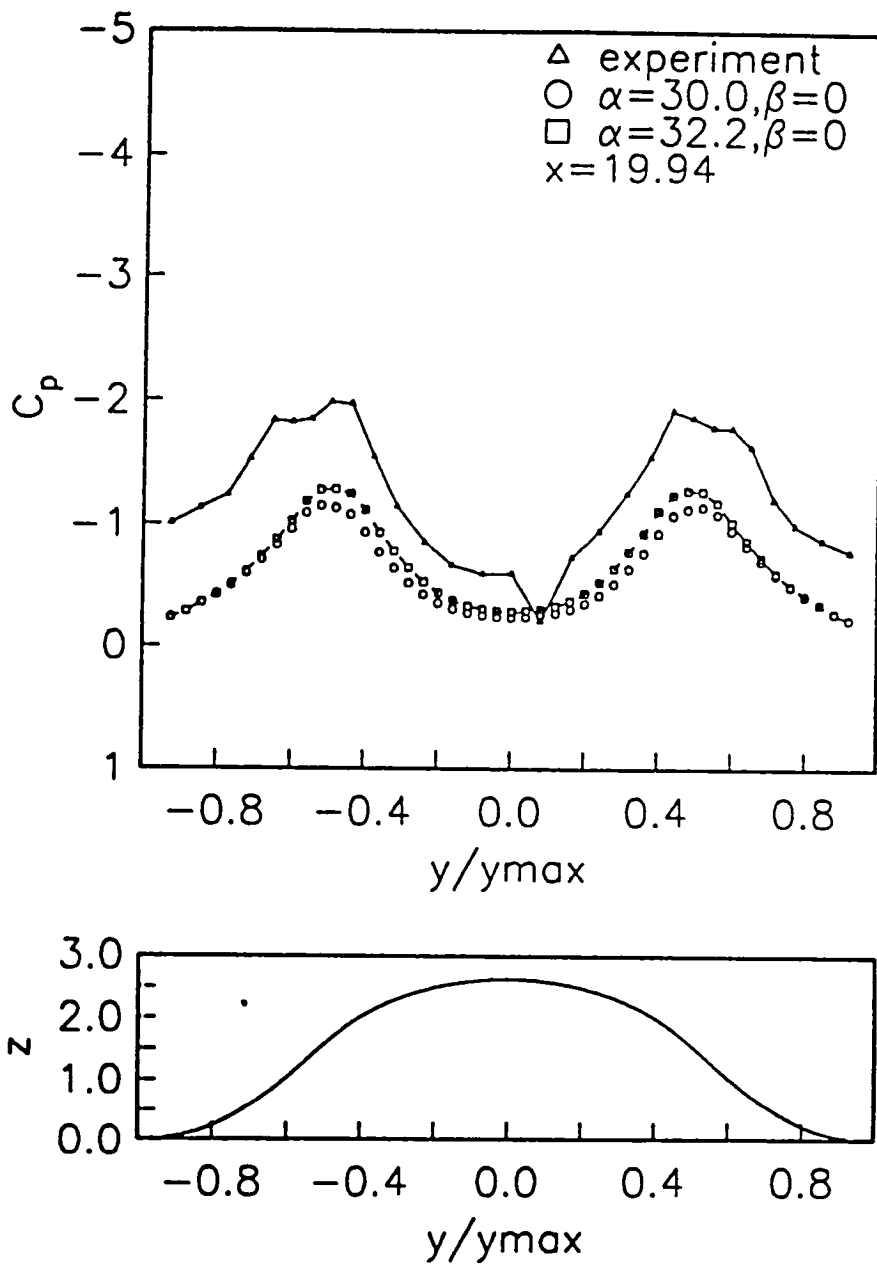


Figure 41(c). Erickson forebody inviscid surface pressures at $x = 19.94$ in.
 ($\alpha = 32.2^\circ$ and $\beta = 0^\circ$)

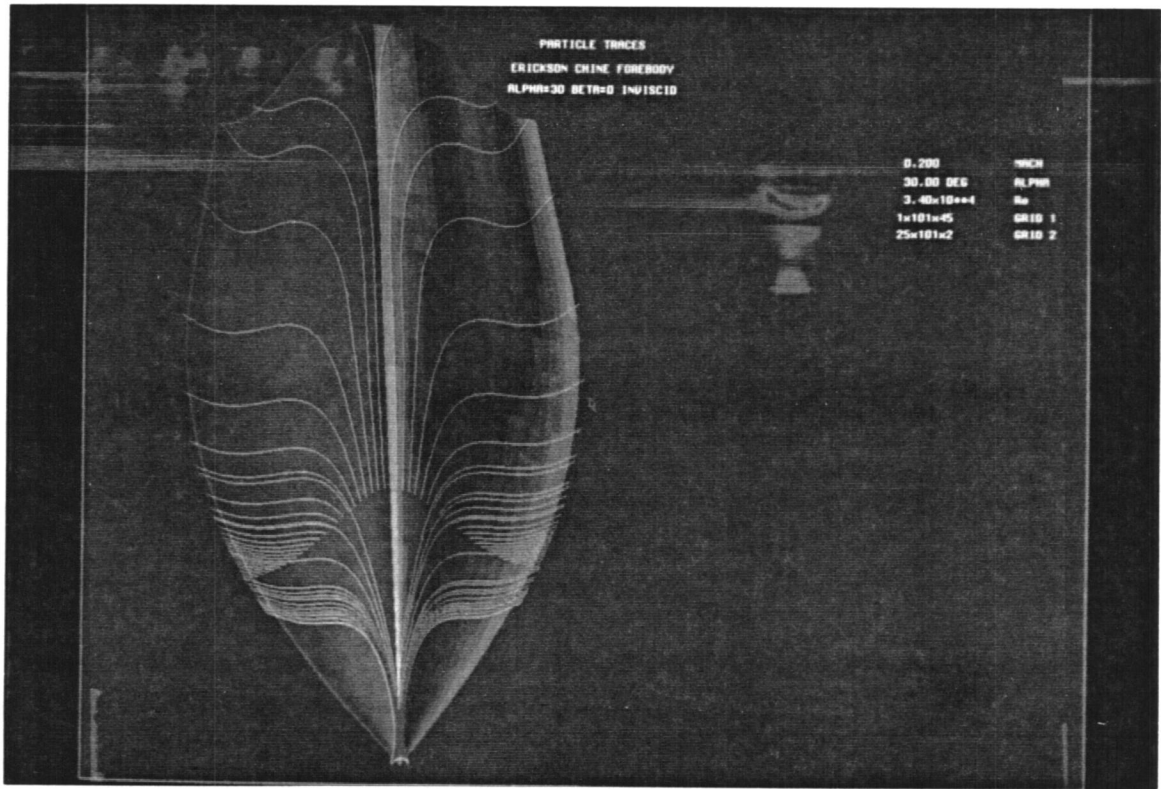


Figure 42. Erickson forebody inviscid surface oil flow pattern ($\alpha = 30^\circ$ and $\beta = 0^\circ$)

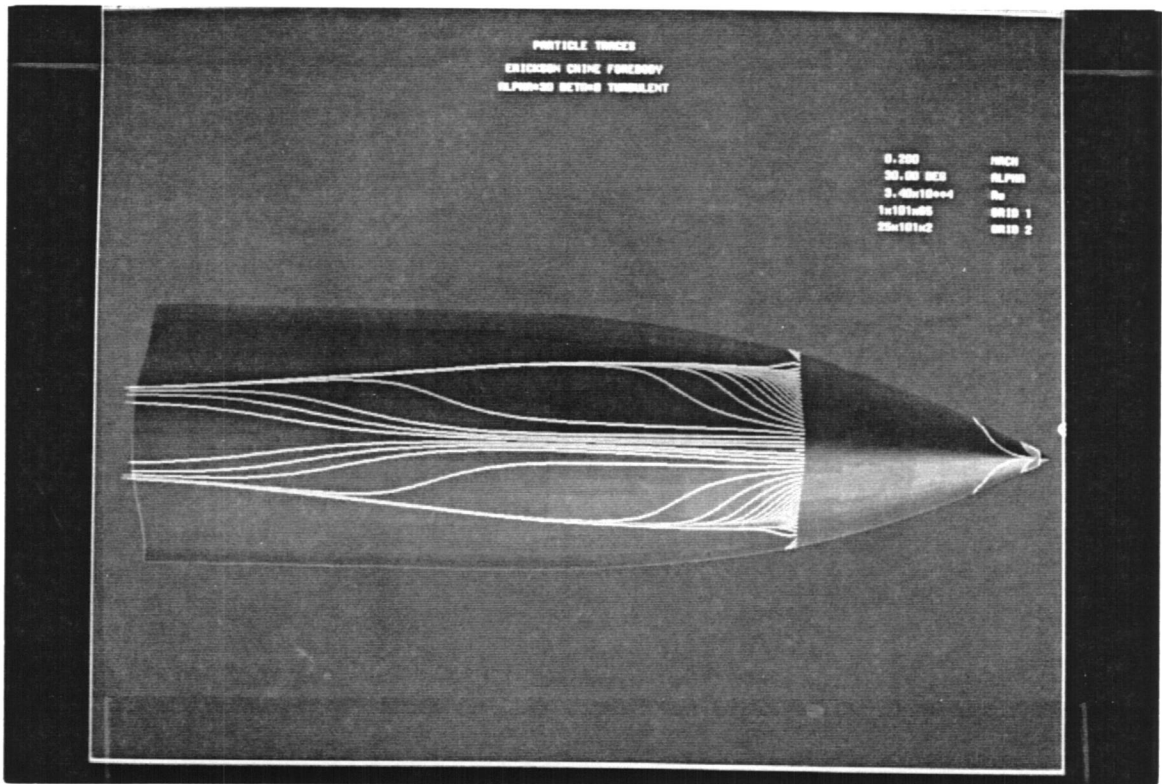


Figure 43. Erickson forebody turbulent surface oil flow pattern ($\alpha = 30^\circ$ and $\beta = 0^\circ$)

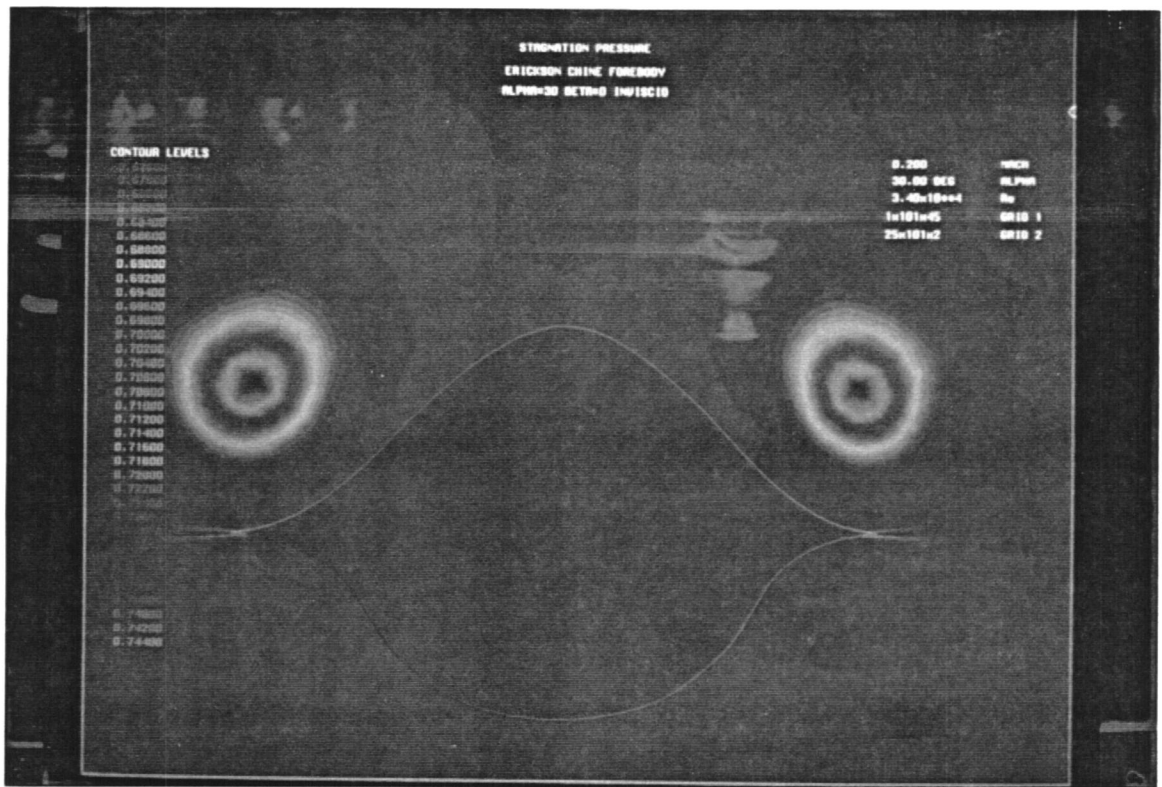


Figure 46. Erickson forebody inviscid stagnation pressure at $x = 13.56$ in.
($\alpha = 30^\circ$ and $\beta = 0^\circ$)

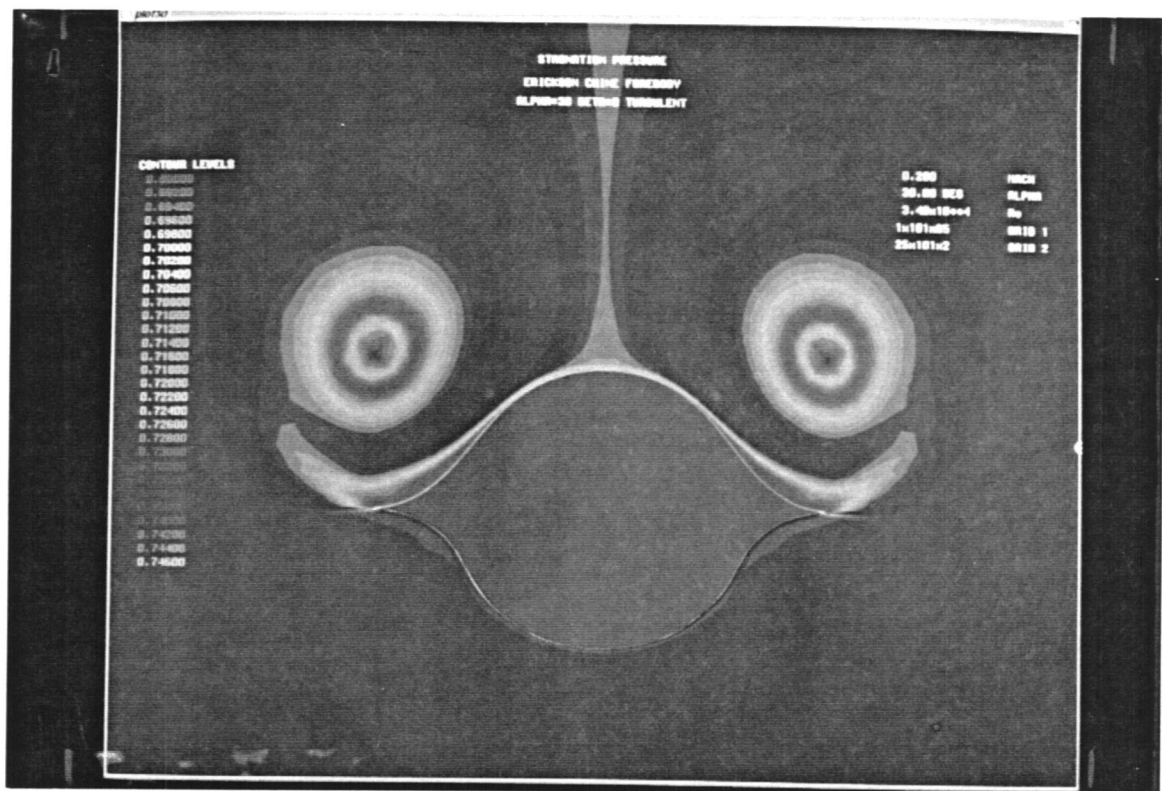


Figure 47. Erickson forebody turbulent stagnation pressure at $x=13.56$ in.
($\alpha = 30^\circ$ and $\beta = 0^\circ$)

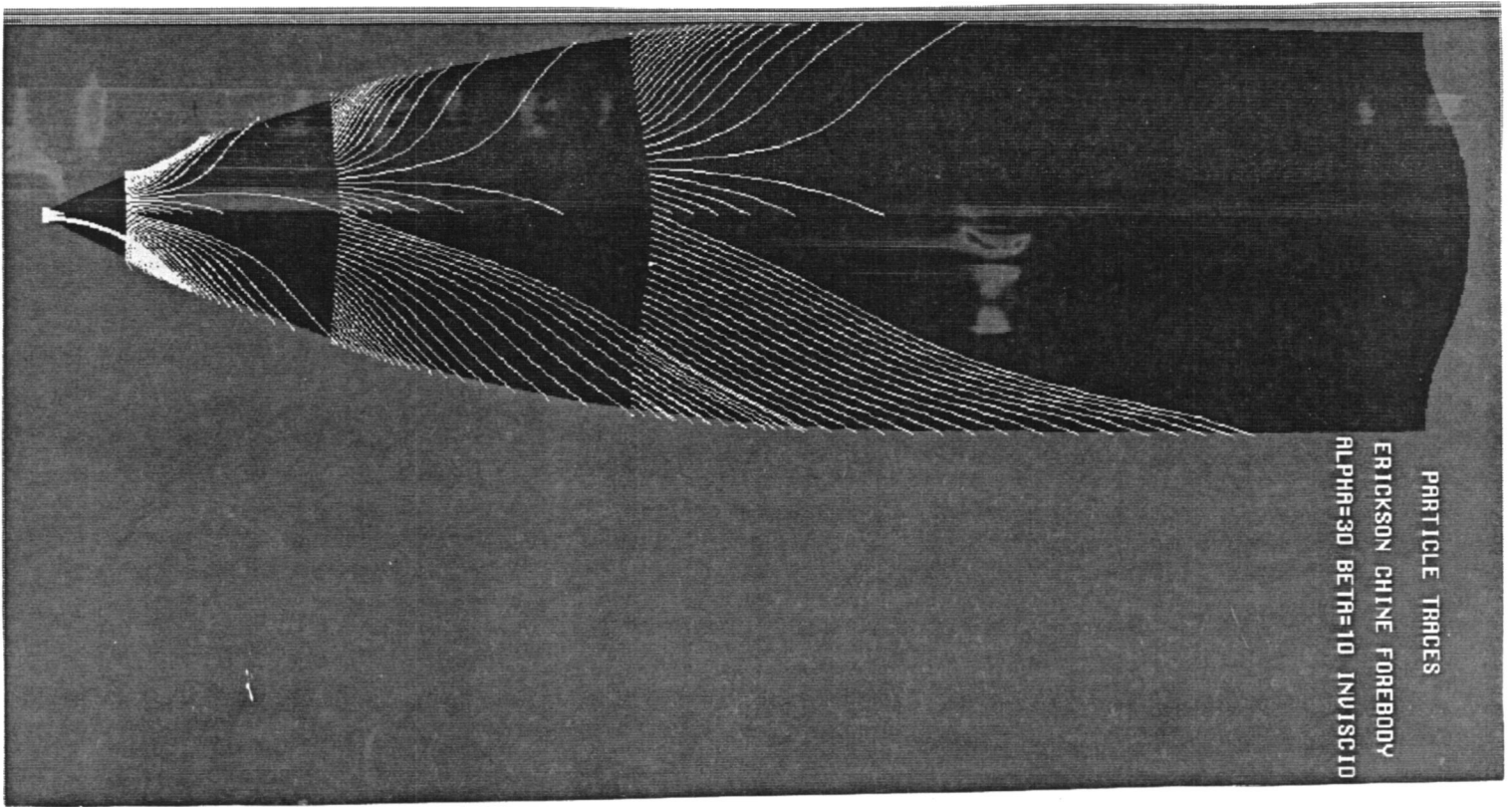


Figure 48. Erickson forebody inviscid surface flow pattern ($\alpha = 30^\circ$ and $\beta = 10^\circ$)

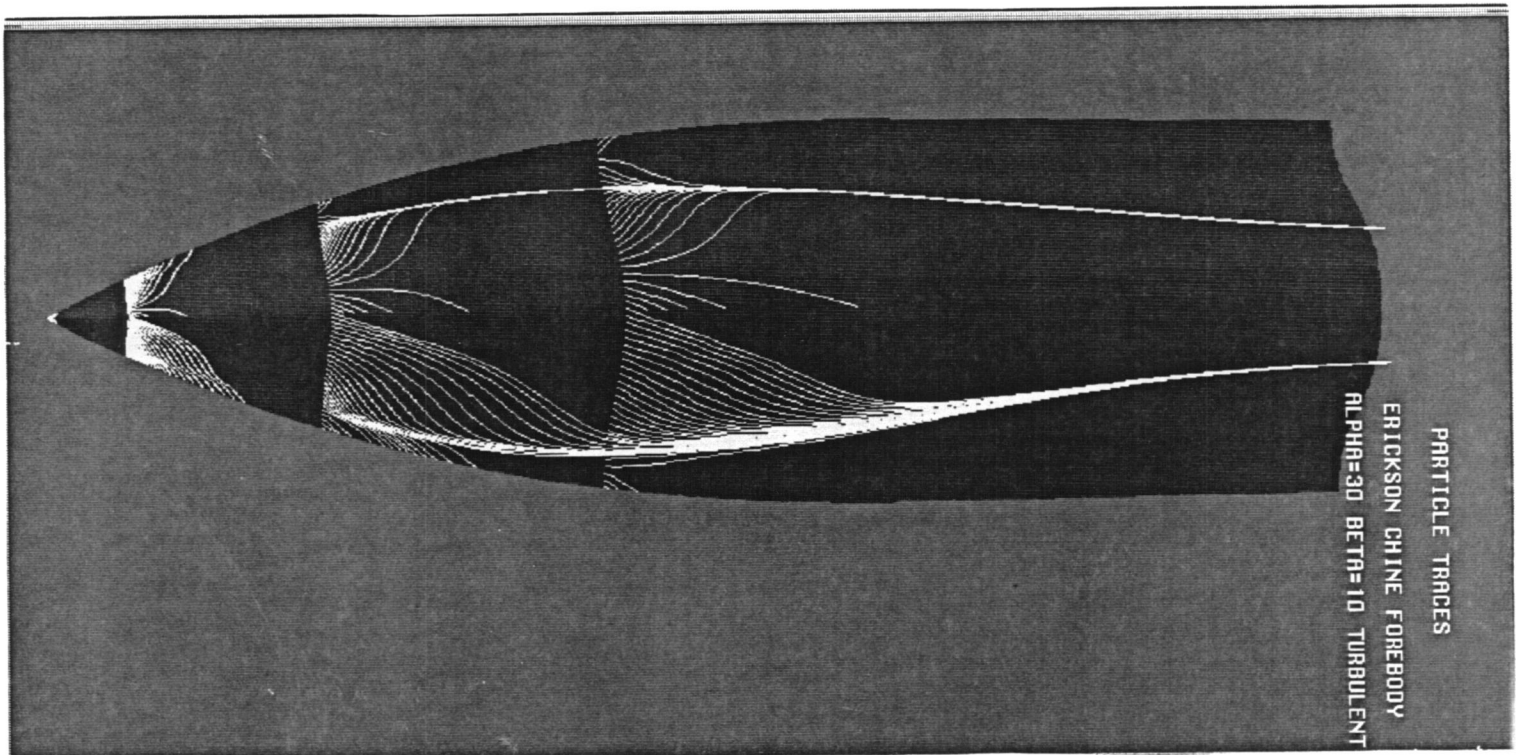


Figure 49. Erickson forebody turbulent surface flow pattern ($\alpha = 30^\circ$ and $\beta = 10^\circ$)

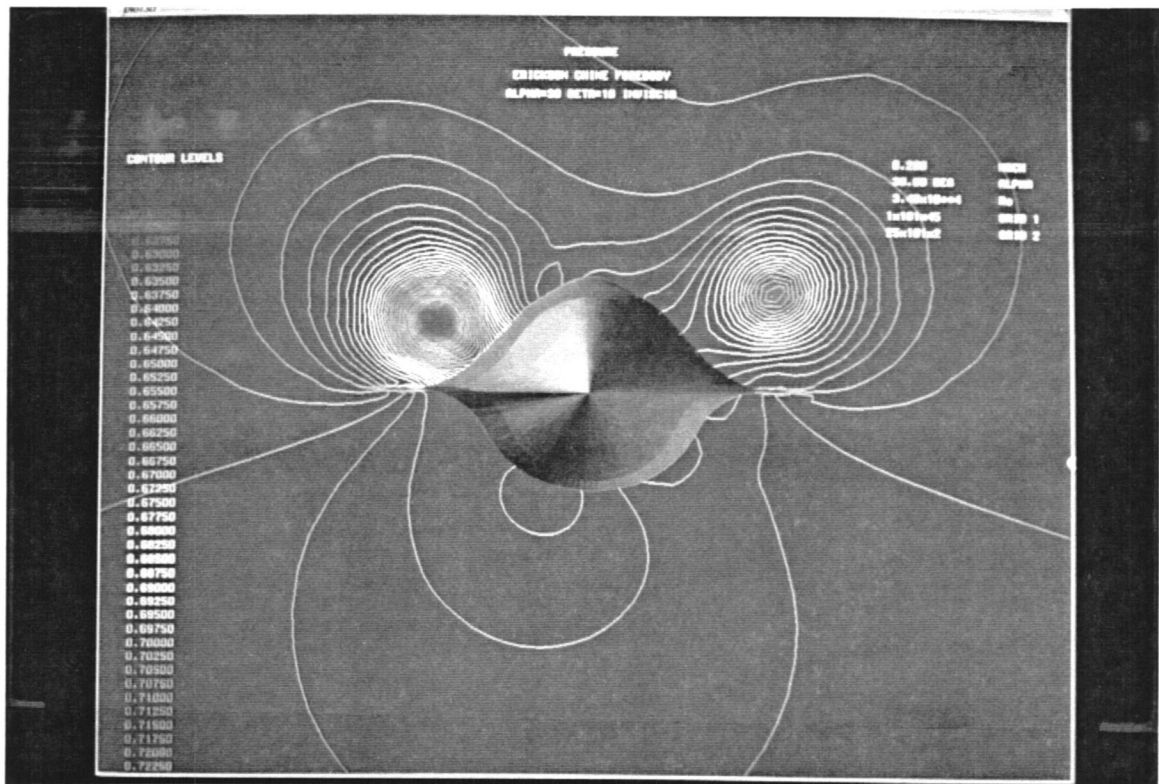


Figure 50. Erickson forebody inviscid pressure contours at $x = 13.56$ in.
($\alpha = 30^\circ$ and $\beta = 10^\circ$)

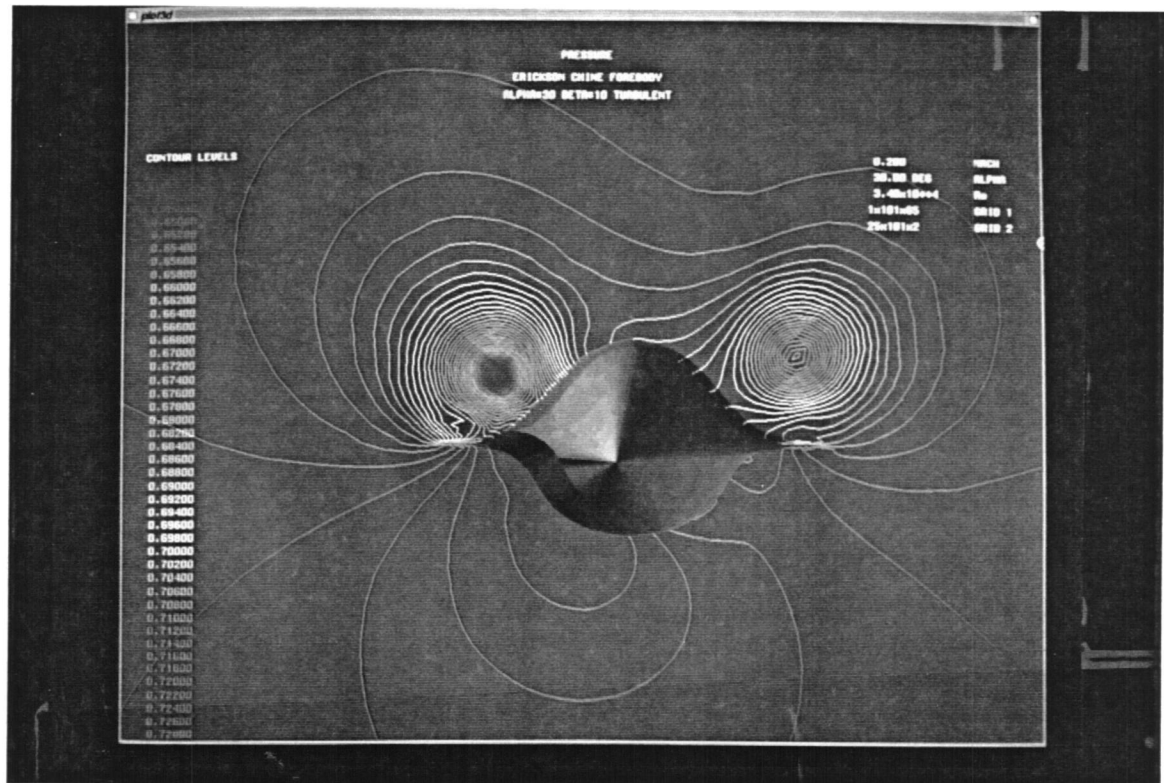


Figure 51. Erickson forebody turbulent pressure contours at $x = 13.56$ in.
($\alpha = 30^\circ$ and $\beta = 10^\circ$)

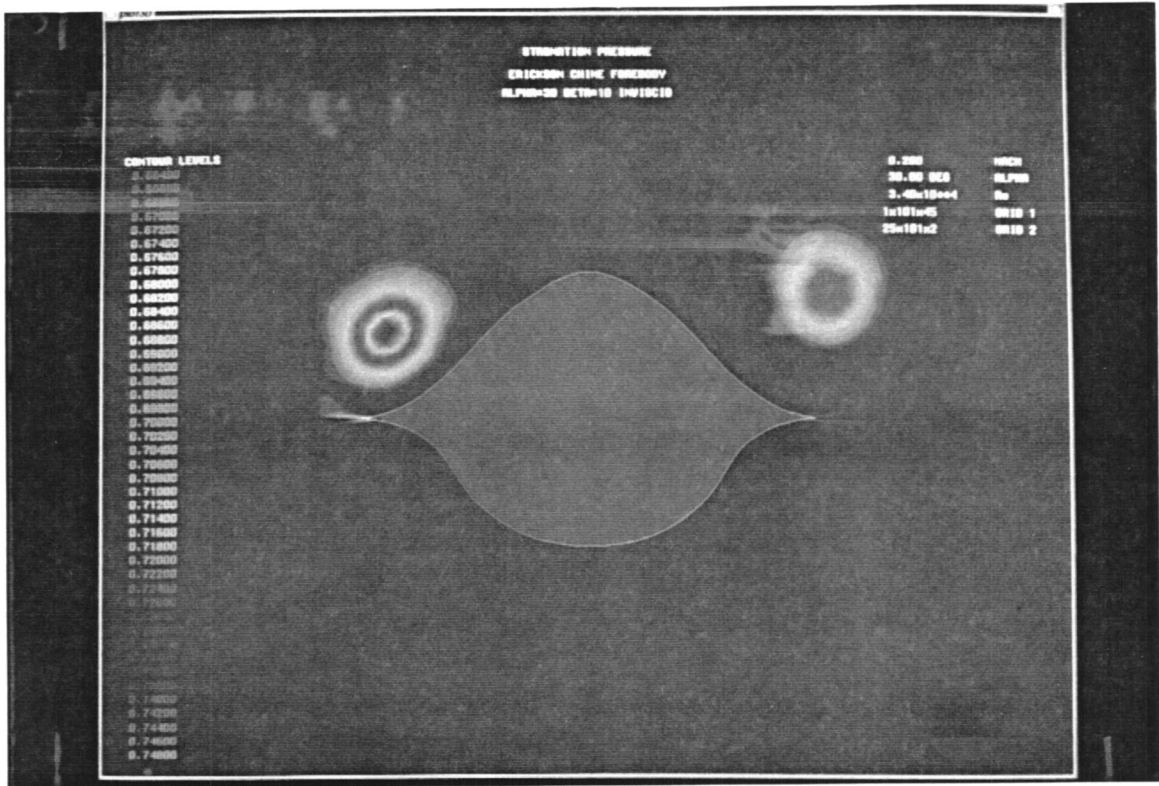


Figure 52. Erickson forebody inviscid stagnation pressure at $x = 13.56$ in.
($\alpha = 30^\circ$ and $\beta = 10^\circ$)

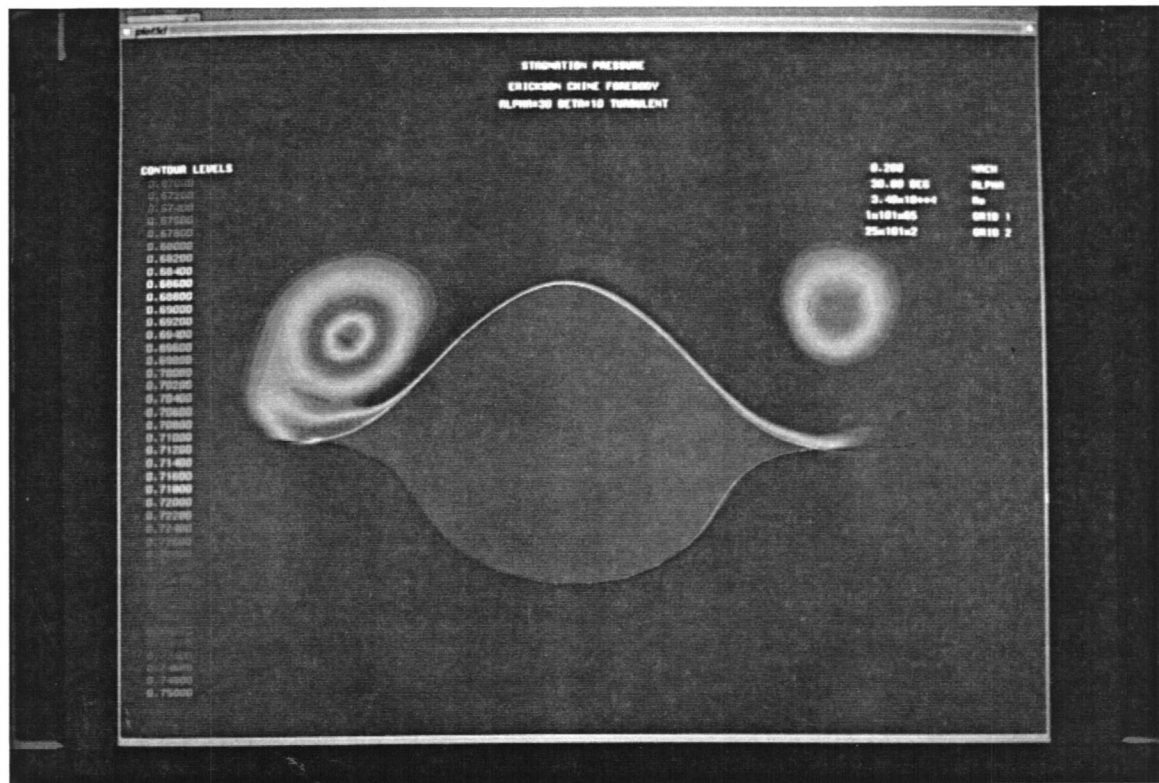


Figure 53. Erickson forebody turbulent stagnation pressure at $x=13.56$ in.
($\alpha = 30^\circ$ and $\beta = 10^\circ$)

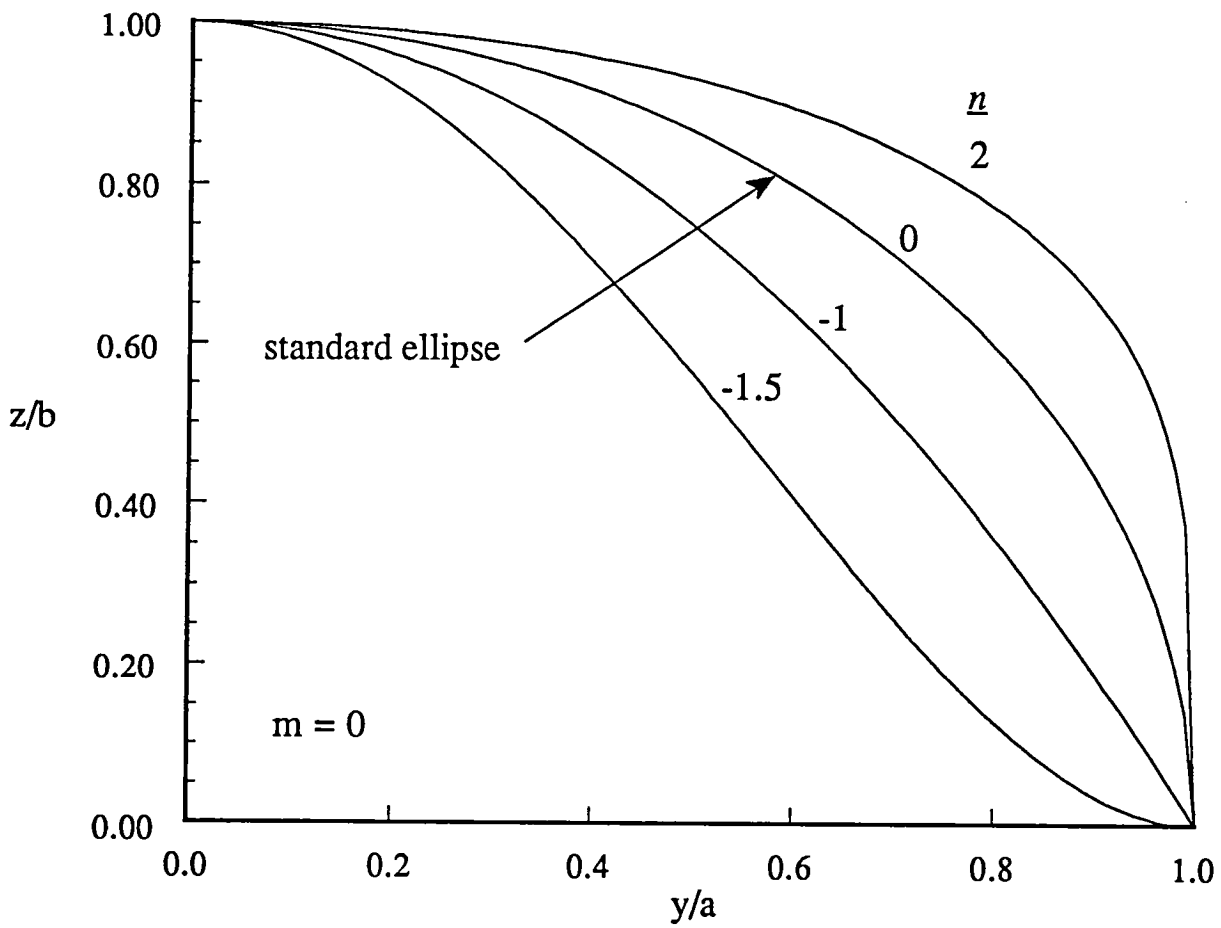


Figure 54. Parametric forebody shapes as driven by the value of n .

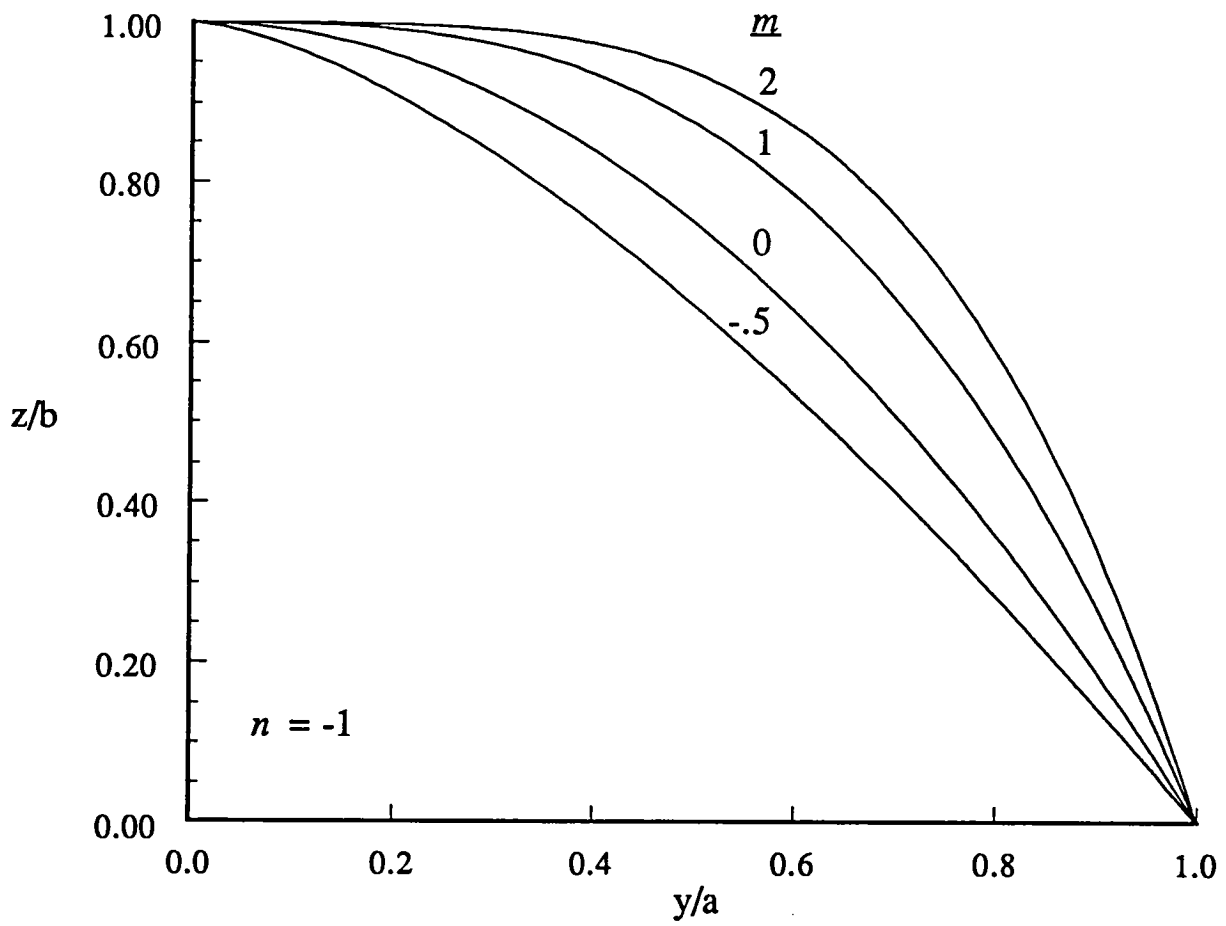


Figure 55. Parametric forebody shapes when the straight sidewall is selected.

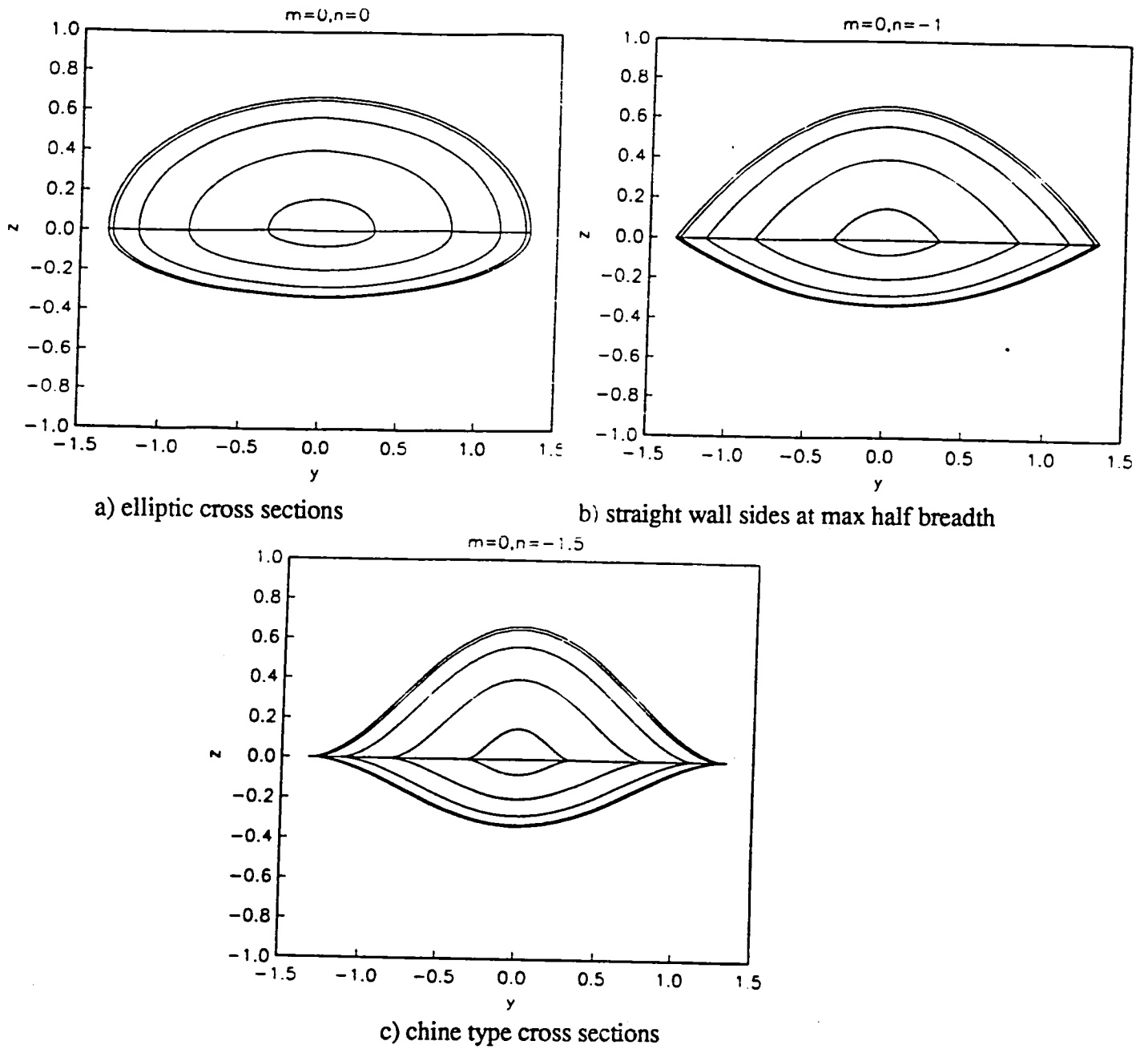


Figure 56. Examples of the parametric forebody for the entire cross section

